Università degli Studi di Parma

Dottorato di ricerca in scienze e Tecnologie dei Materiali Innovativi

Ciclo XXVIII (2013-2015)

Photoconductivity and Electro-Optical Properties of Wide Band Gap Metal Oxides

Coordinatore:

Prof. Enrico Dalcanale

Tutor:

Prof. Maura Pavesi

Dottorando:

Giovanni Piacentini

2016

INDEX

Photoconductivity and Electro-Optical Properties of Wide Band Gap Metal Oxides

1 Properties and Applications of Wide Band Gap Metal Oxides

1.1 Metal oxides as semiconductor materials

Metal-oxides semiconductors are materials that are typically characterized by a binary formula such as M_nO_m, where M is a metallic element like aluminium, zinc, titanium, gallium, tin, etc., which combines with oxygen (O) to form strong bonds with high ionic character.

There is an ample variety of materials that fit this definition, which can have widely different properties; however, some characteristics are present in the majority of metal oxides compounds, the most important of which are the following:

- While being semiconductors, metal oxides typically possess a wide band gap, above 3 eV, so that for some applications they can be considered insulators, especially in comparison with "classic" semiconductors like silicon (E_g=1.12eV) and germanium (E_g = 0.67eV).
- Due to reasons that we will explore briefly, metal-oxides possess good electron conductivity, and are relatively easily doped n-type, but at the same time are poor hole conductors, and p-doping is difficult to obtain in most cases.
- Materials with large energy gaps usually have other useful properties as a consequence, such as: high breakdown electric field, which is the maximum field that the material can sustain before being irreversibly damaged, and high maximum operating temperature; these two properties together allow the material to carry higher power densities compared to standard semiconductors.
- The band gap is over 3 eV, so that the absorption edge falls in the ultraviolet range of the electromagnetic spectrum (wavelength shorter than about 400 nm); on the other end, if the carrier density (due to doping) is not exceedingly high, the plasma edge due to collective oscillation of conduction electrons falls in the near-IR range: as a consequence these material result transparent to visible light

(380-720 nm) while being capable of conducting electricity like a classic semiconductor.

- Most metal-oxides, due to their nature, have high affinity to oxygen, water, and other gases adsorption at the surface; as will be explained later, these gases adsorbed on the crystal surface can change the conduction properties of the material, such that the current in the device depends on the concentration of species in the atmosphere surrounding it.

- Finally, materials such as SnO_2, Ga_2O_3 and in particular ZnO, can be grown easily in a wide variety of nanostructures [1] [2] [3], such as nano-wires, rods, particles, tetrapods among others, using different methods such as growth from the vapour and from solution.

	α-Al_2O_3	**β-Ga_2O_3**	**In_2O_3**	**SnO**	**ZnO**
Structure	Corundum	Monoclinic	Bixbyite	Rutile	Wurtzite
Space Group	$R\bar{3}C$	$C2/m$	$Ia\bar{3}$	$P4_2/mnm$	$P6_3mc$
a (nm)	0.522	1.22	1.0117	0.474	0.325
b (nm)	-	0.304	-	-	-
c (nm)	-	0.58	-	0.319	0.52
Angle (°)	$\alpha = 55.3$	$\beta = 103.8$	-	-	-
E_g (eV)	**8.3**	**4.8**	**3.6**	**3.6**	**3.3**

Table 1 Some metal-oxide semiconductor materials with relative properties.

As part of a general trend, in the last decades materials with ever larger energy gaps are being studied, starting from Ge, to Si and passing from SiC (E_g=2.3-3.2 eV), GaN (E_g=3.4 eV), among others, to arrive at the metal-oxide semiconductors in more recent years. This trend is due to different reasons, primarily for the growing search of low cost and more efficient alternatives to semiconductor technology and materials in different technological areas, the most important of which are the following:

- UV opto-electronic applications [3] [4] [5], such as for the development of light emitting diodes (LEDs), lasers and photo-detectors working in the ultra-violet range; these applications take advantage of the large and direct band gap of these semiconductors, which corresponds to efficient emission and absorption light at wavelengths shorter than about 380 nm.

- The property of being transparent to visible radiation, coupled with the possibility of being made conductive through (usually n–type) doping, is central for finding application as transparent conducting oxides (TCOs) [6] [7]. TCOs are used in the front contact of some photovoltaic cells, but also for transparent electronic devices in general, that can be used in LCD displays, smart screen and windows, etc.

- The high breakdown field of these materials, coupled with high operating temperatures and good physical robustness, are good characteristics for power electronic devices, which are electronic components that can withstand high power densities without deteriorating. Some of these devices are: power switches, AC/DC converters and field effect transistors, among others [8]. In the last two decades, the increasing global demand of energy has sparked renewed interest in such devices, due to the high efficiency and increased power handling and transfer potential.
- Surface affinity to the adsorption different chemical species, chiefly O_2, but also H_2, H_2S, CH_3CH_2OH, etc., coupled with the change in conductivity that surface adsorbed species bring about, make some binary oxides (ZnO, SnO_2, In_2O_3) very good candidates for the development of chemical sensors [9] [10]. Moreover, the possibility of growing a variety of nanostructures with high surface to volume ratio has the potential of increasing the sensitivity of devices based on such structures.

1.2 Conductivity of metal-oxides

The electronic properties of metal-oxides are described by their energy band structures, as in standard semiconductor materials. However, the interaction between the metal and oxygen orbitals in metal-oxides leads to more complicated electronic structures, and also to a significant disparity between electron and hole conduction.

In a covalent semiconductor such as silicon, the conduction band minimum (CBM) and the valence band maximum (VBM) are attributed to the anti-bonding (sp^3 σ^*) and bonding (sp^3 σ) hybridized orbitals of Si; therefore, the band gap is given as the energy difference between the σ^* and σ levels [11] [12].

In contrast to this, metal oxide semiconductors are characterized by chemical bonds with a high degree of ionicity, and this creates an electronic structure that differs markedly from that of covalent semiconductors. For the most commonly discussed semiconducting metal oxides, such as In_2O_3, SnO_2, and ZnO, the metal (M) ns orbitals contribute to the formation of CBM, while oxygen (O) 2p orbitals are responsible for the formation of the VBM; this gives rise to broadly disperse CBM and, on the other hand, a highly localized VBM.

A highly delocalized conduction band minimum produce a small electron effective mass; as a consequence, the electron mobility in metal-oxides is relatively high. Holes, on the other hand, have high effective masses and low mobility, due to the localized valence band maximum that hinders hole transport. As a result, most metal-oxides have electron mobility that is larger than that of holes by two or more orders of magnitude, and this is the main reason for the predominantly n-type conductivity observed in the vast majority of metal-oxide semiconductors reported to date.

Fig. 1 show the specific bonding scheme in these metal oxides that leads to the aforementioned properties: the delocalized nature of the bonding between ns orbitals make for good electron transport even in the amorphous state. This is opposed to what happens in classic covalent materials like Si, in which conduction is highly anisotropic due to the directional nature of the σ bonding between sp^3 orbitals of neighbouring Si atoms.

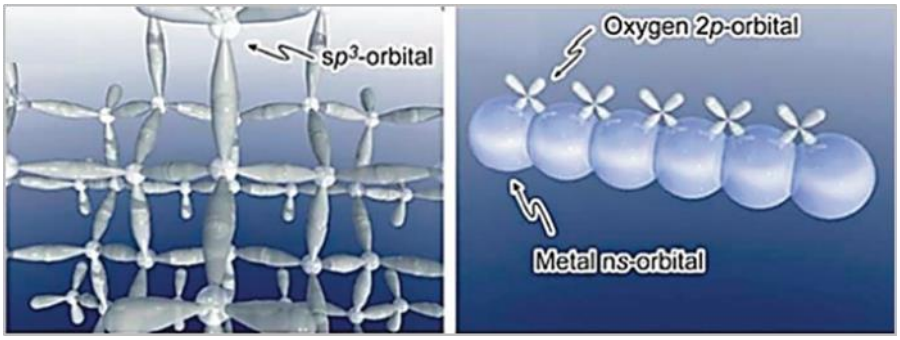

Fig. 1 Bonding structure between atoms in Si (left) and in a typical metal-oxide semiconductor (right).

Although the electronic band structures in many metal-oxides should allow for good charge transport, due to the large band gap there is negligible thermal generation of carriers in intrinsic materials at normal temperatures, leading to very low intrinsic carrier densities. This result in very good semi-insulating properties, which are necessary for most opto-electronic and sensing applications, because a low concentration of free carriers drastically reduces the dark current of the device and, in general, improves the signal to noise ratio. However, for applications in which good conductivity is required even in dark conditions, such as for transparent conductors (TCOs), external control of growth conditions and doping parameters is needed to improve their conductivity. For instance, it has been found experimentally that high electrical conductivity is generally associated with non-stoichiometry in metal-oxide systems [13]. As an example, conductivity in n-type metal oxides (In_2O_3, SnO_2, and ZnO) can be increased when these materials are grown under metal-rich/oxygen-deficient conditions.

Oxygen vacancies (V_O) and metal interstitials (M_i) are thus the potential candidates for electron donors in these systems; likewise, p-type conductivity is related to metal vacancies (V_M) or oxygen interstitials (O_i). However, a complete description of the origin of conductivity would require thermodynamic considerations to determine whether any of these defects are stable under normal conditions, as well as electronic structure calculations to investigate whether the energy level of each defect is shallow enough to contribute to the conductivity [14] [15].

It has long been believed that V_O are responsible for n-type conductivity, while M_i cause p-type doping, but an accurate picture for each species is more complicated and is still

under debate: for example, in the case of ZnO, recent DFT calculations have pointed out that V_O really behave as deep donors, and cannot contribute significantly to the n-type conductivity [16]. The last studies suggest instead that hydrogen is the likely contributor to n-type conductivity in most cases [17] [18].

In the case of oxide semiconductors, doping is usually one-sided: n-type materials can only be doped with donors and p-type with acceptors. In fact, doping with the opposite type of carrier has not been successful as most materials suffer from self-compensation, that is, the spontaneous formation of defects that contribute the opposite charge, which tend to neutralise the effects of doping [19]. Nevertheless, there are controversial reports, such as p-type doping in ZnO using *group V* elements, e.g. N, P, As, or S [20].

Finally, many oxide semiconductors exhibit both band-like and hopping-like charge transport characteristics: at low temperatures, impurity conduction dominates and hopping between localised states caused by defects and impurities occurs; approaching room temperature, on the other hand, charge transport becomes band-like [21] [22].

In addition to these mechanisms, morphology plays a significant role in the charge transport properties of material. In clustered-together nanoparticles and polycrystalline films, is of fundamental importance to consider the effects of particle and grain boundaries. Localised band bending/potential barriers at the surface and between grains/particles can also have important effects on charge transport. In the presence of such potential barriers and at high temperatures, charge transport can often be attributed to thermionic emission over the barrier, while at lower temperatures tunnelling of charges through the barrier is the primary mechanism.

1.3 Examples of applications

1.3.1 UV photo-detectors

As noted before, metal-oxide semiconductors like ZnO, Ga_2O_3, SnO_2, and In_2O_3 find applications in a range of different technological areas, predominantly as sensors, for UV light or gas species, and in high power electronic components.

Monoclinic gallium oxide (β-Ga_2O_3), with the wide bandgap of about 4.9 eV in the deep UV region, is one of the most promising candidates for high-performance UV photodetectors. β-Ga_2O_3 thin films and individual nanostructures, such as nanobelts and nanowires, have been demonstrated by several reports to be potential *solar-blind UV photodetectors* [23] [24] [25]. These detectors show good performances to 254 nm light illumination: the dark current density is on the order of a few $pA \cdot cm^{-2}$, which is one of the best properties of β-Ga_2O_3 nanostructures, while the conductance of the device in the deep UV region is about 1000 times higher.

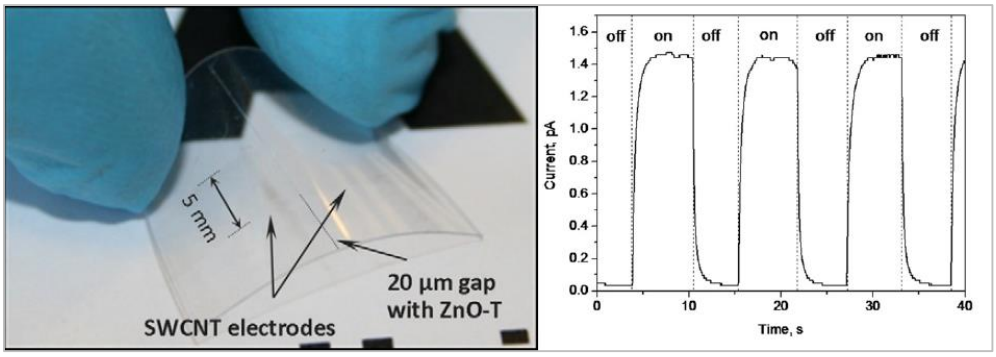

Fig. 2 Flexible UV sensor based on ZnO nano-tetrapod deposited over a polyethylene terephthalate (PET) substrate, with single-walled carbon nanotube (SWCNT) transparent electrodes (left). On the right is reported the photocurrent vs. time response of the device. Reproduced from [28].

Because of the high surface-to-volume ratio, and superior sensitivity to UV light with respect to single crystals, *ZnO nanostructures* have been widely developed for nanometer-scale visible-blind UV-light detection (energy gap of ZnO is about 3.3 eV) with a high sensitivity and selectivity. *Individual ZnO-based nanowire* photodetectors were reported by Yang et al. in 2002 [26]. The conductivity of ZnO nano-structures is extremely sensitive to UV light exposure (about 365 nm), with a decrease in resistivity with respect to dark conditions of 4 to 6 orders of magnitude. The photo-response is strongly dependent on the ambient gas condition, being slow in vacuum or inert gases and fast in air, indicating the role of the oxygen in the photocurrent process. *Flexible*, *low-cost*, photoconductive UV sensors were also developed in the last few years, based on ZnO nano-crystalline powders [27] and nano-tetrapods (Fig. 2) [28]. In the case of devices based on multiple nano-crystals, the overall opto-electronic behaviour is determined mainly by the fact that charge carriers have to cross several *inter-particle barriers* in a percolative type of conduction [29].

1.3.2 Gas sensors

Due to the strong dependence of electric conduction on the presence of surface adsorbed species, metal-oxides like ZnO, SnO_2 and Ga_2O_3 have been used to develop *gas sensing devices*. Metal-oxide gas sensors are usually based on clustered nano-structures or porous crystals, due to their higher surface to volume ratio.

Gas sensors based on metal-oxide (MO) nanostructures generally consist of three parts, i.e., sensing film, electrodes and heater [9]. The surface film of MO nano-structures will change in resistance upon exposure to target gases; a pair of electrodes is used to measure the resistance of the sensing film. Usually the gas sensors are equipped with a heater (e.g. a thermal resistor), so that they are heated externally to reach the optimal working temperature.

SnO_2 nano-belts based gas sensors, were developed by *Comini et al.* in 2002 [30]. They reported high sensitivity toward ethanol and NO_2 working at 300°C in air.

Zappettini et al. (2008) [31] used vapour-phase grown ZnO nano-tetrapods deposited on Al_2O_3 as gas sensing devices to probe a variety of reducing gas species: CH_3CH_2OH, NO_2, CO and H_2S (Fig. 3). Thanks to the high surface to volume ratio of the nano-structures, the reported sensitivity of the device reach the ppm range. To obtain high response time to gas pulses, the detectors must reach a working temperature of ≈400°C.

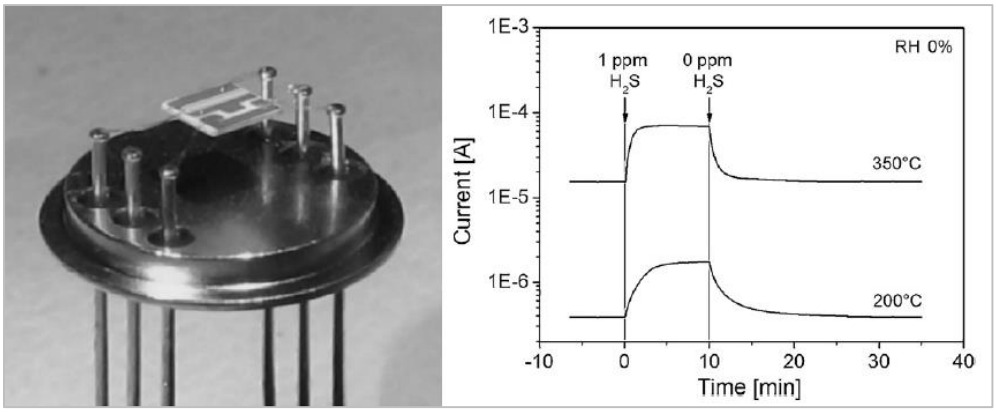

Fig. 3 ZnO nano-tetrapod based gas sensor (left). Tetrapod nano-crystals are deposited between two gold contacts on an alumina substrate; a platinum resistance is deposited near the active layer to heat the device to the working temperature (400°C). On the right, the current response of the device to a pulse of 1 ppm H_2S gas in air is reported at two different working temperatures. It is evident that the response time shortens as the temperature increase [31].

1.3.3 High power devices

High operating temperature, wide band gap, and high breakdown field, make Ga_2O_3 an optimal choice for developing high power devices, superior to even SiC and GaN.

For example, *Higashiwaki et al.* [32] developed in 2013 a metal-oxide-semiconductor field-effect transistor (MOSFET) from melt-grown single crystals of β-Ga_2O_3 (Fig. 4).

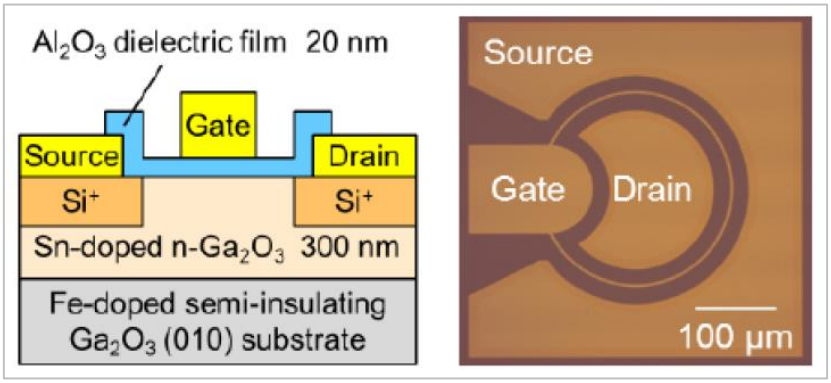

Fig. 4 Cross sectional schematics (left) and optical micrograph (right) of Ga_2O_3 MOSFET [32].

The reported Ga_2O_3 MOSFETs exhibits excellent characteristics including: a high on–state drain current of 39 mA/mm, a large off–state breakdown voltage of 370 V, an extremely low leakage current (less than a few pA/mm), and a high on/off drain current ratio of over 10 orders of magnitude. These excellent device characteristics can potentially lead to large reduction in power losses during switching operations and are suitable for practical power devices.

1.4 Specific materials

In this broad picture of current research regarding binary metal-oxides semiconductors for different applications, this particular thesis is focused on two of these materials for specific applications.

The first is *gallium oxide* (Ga_2O_3), in the form of *thin films* that were deposited by metal-organic vapour-phase epitaxy (MOVPE), for applications in UV opto-electronics.

Various thin film samples were morphologically and structurally characterized using x-ray diffraction and electron microscopy. Optical characterization was done by absorption spectroscopy and cathode-luminescence analysis, while the thermal stability of the samples was investigated by thermal annealing experiments.

Finally, electric contacts were deposited on some films, in order to develop *deep ultra-violet photo-detectors*. The electric and electro-optical characteristic of these detectors were then investigated by measuring the current-voltage characteristics of the device and the photocurrent spectral and time response.

The second material described in this thesis is *zinc oxide* (ZnO), in the form of *tetrapod nano-crystals*, which were grown by vapour-phase synthesis for gas sensing applications.

A ZnO gas sensing detector is constituted of a layer of multiple nano-crystal deposited on a substrate between planar electrodes. To characterize these devices and the properties of nano-tetrapods, electrical and electro-optical analysis were done on *multiple* and *single* zinc oxide nano-tetrapod based samples.

In particular, the unusual photocurrent vs. time response of these samples was investigated in different air pressure conditions, in order to understand the peculiar behaviour.

As a consequence, the following section of this thesis is divided into two chapters, the first, Ch. 2, describes the experimental results relative to Ga_2O_3 thin film samples, while Ch. 3 presents results regarding ZnO nano-tetrapod samples.

2 Gallium oxide thin films

This chapter is dedicated to the experimental results obtained from gallium oxide thin film samples grown on alumina substrates by *metal-organic chemical vapour deposition* (MOCVD) and *atomic layer deposition* (ALD) techniques. Ga_2O_3 thin films were characterized by different experimental techniques and an UV photodetector obtained from a chosen sample was demonstrated.

Before describing the experimental results, there will be a brief introductory section describing the material and the techniques used to grow the samples.

2.1 Introduction to Ga_2O_3 and its poly-types

Gallium (III) oxide (Ga_2O_3) is a metal-oxide material that has been investigated as a semiconductor only recently, mostly in the last 10 years. However, research interest has grown strongly in the last few years, mostly in Japan and Germany.

This is because gallium oxide is a very promising material, thanks to a wide range of properties that make it very good for high power devices and UV opto-electronics.

2.1.1 β-Ga_2O_3

The thermodynamically stable form of gallium oxide at atmospheric pressure and room temperature is the mono-clinic β-Ga_2O_3 (Fig. 5). The band gap of β-Ga_2O_3 is indirect and has a value of 4.83 eV, with the VBM located just off the M point, and is slightly smaller than the direct band gap of 4.87 eV at the Γ point. However, the weakness of the indirect transitions and the small energy difference between indirect and direct gaps effectively make β-Ga_2O_3 a *direct-gap material* [33]: this consistent with the experimentally observed sharp absorption onset at about 4.9 eV by several experimental groups [34].

Ga_2O_3 crystallize readily from the melt in the β phase, and tends to grow intrinsically n-type, while intentionally n-type doping can be achieved to concentrations of 10^{17}-10^{19} cm^{-3}.

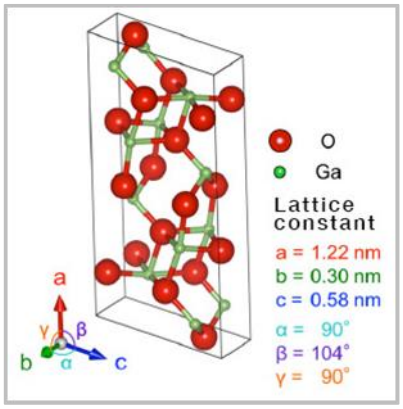

Fig. 5 Unit cell of monoclinic β-Ga_2O_3 phase with corresponding lattice parameters reported. Space group is C2/m.

As is the case for most metal-oxide semiconductors, Ga_2O_3 has good electron mobility of about 300 cm^2/Vs, while the hole mobility is 3 order of magnitude less, so that there is virtually only electron conduction in any intrinsic or n-doped material. Low hole mobility is caused by the very low curvature of the valence band, which is almost flat in Ga_2O_3; as introduced in Par. 1.2, this is a consequence of the highly localized oxygen 2p orbitals that make up the VB, and is a common feature of metal-oxide semiconductors.

A very important property of the beta phase of gallium oxide is its very high breakdown field of about $8 \cdot 10^6$ V/cm, that is the maximum electric field that the material can sustain before its dielectric properties are disrupted. In this respect Ga_2O_3 is much better than either silicon carbide (SiC) and gallium nitride (GaN), two of the best wide band gap semiconductor materials, and is a close second to diamond, for which can be a cheaper alternative (see Table 2).

	Si	GaAs	4H-SiC	GaN	Diamond	β-Ga_2O_3
Energy gap E_g (eV)	1.1	1.4	3.3	3.4	5.5	4.6-4.9
Electron mobility μ_e ($cm^2/V \cdot s$)	1,400	8,000	1,000	1,200	2,000	300 (est.)
Breakdown field E_{BD} (MV/cm)	0.3	0.4	2.5	3.3	10	8 (est.)
Relative dielectric constant ε_r	11.8	12.9	9.7	9	5.5	10
Thermal conductivity K_{th} (V/K·cm)	1.5	0.55	2.7	2.1	10	0.23

Table 2 Some of the material properties of gallium oxide compared to those of other important semiconductor materials, including diamond [8].

Thanks to the wide band gap, β-Ga_2O_3 devices can be operated at relatively high temperatures; this is because thermal noise in a semiconductor device depends primarily on the thermal generation and recombination of carriers [35], which in turn depends on the relative importance of the thermal energy *kT* with respect to the energy gap E_g. The high operating temperature, coupled with the high breakdown field, make it an excellent material for power electronics such AC/DC converters or high voltage switches [8].

Moreover, Ga_2O_3 conductivity is sensitive to surface adsorbed species: particularly oxygen (O_2) and water vapour; below 700°C it is also sensitive to reducing gases such as CO, H_2, and CH_x on the basis of surface reactions. On the other hand, above 900°C, it can be used as an oxygen sensor based on the existence of oxygen vacancies inside the material [36].

Other applications take advantage of the wide band gap in the UV region of the spectrum: high sensitivity deep UV photodetectors, working at wavelengths $\lambda<270$ nm and transparent to visible radiation, find application in a wide range of technological fields, such as solar UV research, military applications, fire detectors that can operate in broad daylight, etc. [4] [23].

Finally, β-Ga_2O_3 can be used as a low-cost substrate for the epitaxial growth of gallium nitride (GaN) thin films. Transparent, n-doped β-Ga_2O_3 substrates for GaN/Ga_2O_3 heterostructures allow the development of p-n junctions for the fabrication of blue light emitting diodes [37].

2.1.2 Other Ga_2O_3 poly-types

In addition to the monoclinic β polymorph, other 5 phases are known, and these are: **α**, **γ**, **δ**, **ε** and **κ**. These phases are obtained from Ga-containing inorganic precursors or by thermal treatments of β-Ga_2O_3 crystals; in addition, interconversion between different Ga_2O_3 poly-types can be obtained by thermal annealing at specific temperatures, as reported schematically in Fig. 6.

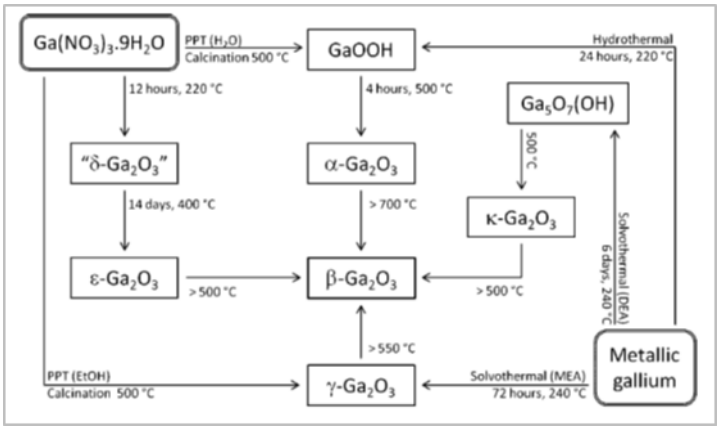

Fig. 6 Summary of the synthesis and interconversion of the polymorphs of Ga_2O_3. Note that δ-Ga_2O_3 is a nano-crystalline form of ε-Ga_2O_3, while κ-Ga_2O_3 is a transient phase, that was never isolated as in pure form. PPT=precipitate, DEA=diethanolamine and MEA=monoethanolamine [38].

Of these, the only relatively well known and most studied (after the β) is the metastable α phase (hexagonal, akin to α-Al_2O_3). Of the other four, κ is a transitional phase, that was never isolated in pure form, and δ was revealed to be a nano-crystalline form of the ε phase [38]. The remaining phases are poorly described, with only a handful of research papers detailing their structure, and this is mainly due for two reasons: first, it is extremely difficult to obtain pure samples, due to the low thermodynamic stability of these poly-types (at ambient temperature and pressure) with respect to β-Ga_2O_3, in which the samples tend to revert to, at least partially. Secondly, and more importantly, these phases are characterized by structural disorder. That make it difficult the resolution of the crystal structure.

2.1.3 ε-Ga_2O_3

The ε-Ga_2O_3 polymorph it is probably the least known of all: it was first synthesized in the 1950s through the thermal decomposition of $Ga(NO_3)_3$ [39]. Although the authors indicated a high thermal stability of their ε-Ga_2O_3 up to 870°C, the full structural characterization was not made, and the crystal structure remained unclear for over half a century.

The structure was resolved only very recently from x-ray and neutron diffraction data [38] [40], and was revealed to be hexagonal, space group *$P6_3mc$*, with *partially occupied lattice sites*, as reported in Fig. 7 and Table 3.

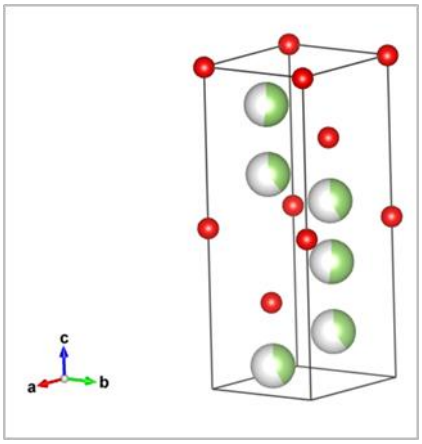

Fig. 7 Structure of the ε-Ga_2O_3 unit cell. Oxygen sites are red, while gallium sites are white/green.

Atom	Wyckoff Site	*x*	*y*	*z*	U_{iso} [Å^2]	S.O.F
Rietveld						
Ga1	2b	1/3	2/3	0.5598(6)	0.0044(2)	0.423(3)
Ga2	2b	2/3	1/3	0.6538(5)	0.0044(2)	0.399(2)
Ga3	2b	1/3	2/3	0.3705(4)	0.0044(2)	0.511(3)
O1	2a	0	0	−0.0016(6)	0.0091(2)	1
O2	2b	1/3	2/3	0.7556(6)	0.0091(2)	1
PDF						
Ga1	2b	1/3	2/3	0.5622(2)	0.01382(3)	0.3701(7)
Ga2	2b	2/3	1/3	0.65568(9)	0.01382(3)	0.322(2)
Ga3	2b	1/3	2/3	0.36433(5)	0.01382(3)	0.641(2)
O1	2a	0	0	0.99915(7)	0.01433(3)	1
O2	2b	1/3	2/3	0.75599(8)	0.01433(3)	1

Table 3 Refined crystal parameters for ε-Ga_2O_3. Space group is $P6_3mc$. Rietveld parameters: a=2.9036(2), c=9.2554(9) Å, wRp=1.48%. Measured density= 6.4299 g·cm-3, calculated density=6.0622 g·cm^{-3}. PDF parameters: a=2.90726(5), c=9.2559(3) Å, wRp=12.7% [38].

2.2 Deposition techniques

Ga_2O_3 thin films were grown on 1" and 2" substrates using a custom-made stainless steel metal-organic vapour phase epitaxy (MOVPE) reactor (see Fig. 8), starting from trimethyl-gallium (*TMGa*) as metal-organic precursor and ultrapure water as oxygen source. Depositions were carried out at the CNR-affiliated *Institute for Materials for Electronics and Magnetism* (IMEM) in Parma, Italy.

Thin films depositions were made using a combination of standard MOVPE deposition as well as atomic layer deposition (ALD) MOVPE techniques.

Fig. 8 Custom-made MOVPE reactor with which the Ga_2O_3 thin films were grown. The reactor is placed at the IMEM-CNR institute in Parma, Italy.

2.2.1 Chemical vapour deposition

CVD involves the formation of a thin film of solid material on a substrate via chemical reactions of precursors in the vapour phase. It is the chemical reaction that distinguishes CVD from other types of deposition from the vapour phase (e.g. physical vapour deposition or PVD) [41]. The chemical reactions can occur homogeneously in the gas phase and/or heterogeneously on the substrate.

To obtain high quality films, heterogeneous reactions are preferred [42]. In the CVD technique, precursors are delivered into a carrier gas stream, which transports the precursors to a substrate, onto which application of (thermal) energy cause the reaction. The key steps of CVD are (Fig. 9):

1. Evaporation and transport of precursors into the reactor trough the gas flow
2. Mass transport of the reactants to the surface of the substrate

3. Adsorption of the reactants on the substrate's surface
4. Surface diffusion to suitable reaction sites
5. Nucleation and surface chemical reactions leading to film growth
6. Desorption and mass transport of remaining fragments of the decomposition away from the reaction zone.

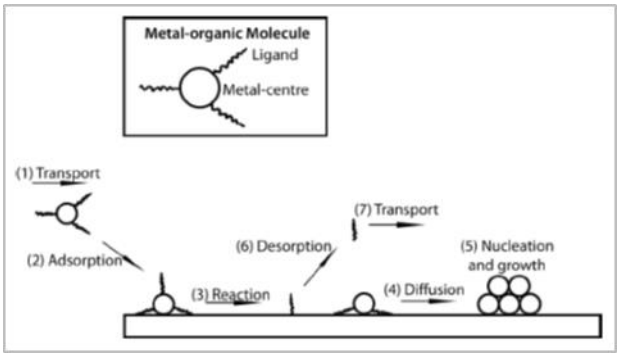

Fig. 9 Principal steps of the CVD growth from metal-organic precursors.

The film growth rate in thermal CVD is determined by the substrate temperature and the pressure inside the reactor, as well as the complex gas phase chemistry occurring in the reaction zone, which is specific to the reaction used. At lower substrate temperatures the film growth rate is determined by the kinetics of the chemical reactions occurring either in the gas phase or on the substrate surface, and it is generally denoted as *surface reaction limited* film growth. As the temperature is increased, the film growth rate becomes almost independent of temperature, and the growth is determined by the mass transport of the precursors through the boundary layer to the growth surface. This is known as *mass transport limited* film growth.

At higher temperatures, the growth rate decreases as the film precursors are desorbed from the film surface and/or depletion of reagents on the reactor walls due to gas-phase side reactions. These gas-phase side reactions become more important at high temperatures and higher partial pressures of the reagents.

2.2.2 Layer morphology

Layer morphology is crucial in determining the physical characteristics of a thin film. The layer morphology is determined by surface diffusion and nucleation during deposition; these, in turn, are affected by the temperature of the substrate, the partial pressures of the reagents and total pressure of the system. In the case of epitaxial growth on substrates of a different material than that of the film (*heteroepitaxy*), layer morphology

is also determined by the eventual difference in crystal structure between the two materials (e.g. cubic film on hexagonal substrate), as well as from the *lattice mismatch* (or misfit) *f*, that is the relative difference in the *in-plane lattice parameter*:

$$f = \frac{a_f - a_s}{a_f} \qquad (1)$$

Where a_f is the in-plane lattice parameter of the film, while a_s is that of the substrate.

Depending on the aforementioned factors, the film can grow as *epitaxial*, *amorphous* or *polycrystalline*. The growth of epitaxial (i.e. single crystal) layers usually occurs at high temperatures and relatively low growth rates, such that the rate of surface diffusion of species is faster than the rate of adsorption of new molecules on the surface of the film. This allows the surface migration of adsorbed species to their respective crystal sites, forming a well-ordered layer.

On the other hand, when the substrate temperature is low and/or the growth rate is fast, the opposite situation occurs, and surface adsorbed molecules do not have time to reach their crystal sites, and tend to solidify in a random position close to the adsorption site, which results in a disordered layer. In between these two extremes there is the growth of polycrystalline layers, that happens at intermediate temperatures and growth rates. The typical result is nucleation at many different sites on the substrate, which than grow to form many mono-crystalline islands; the islands then tend to coalesce and, if these do not have exactly the same crystallographic orientation, form a polycrystalline layer [43].

In the case of heteroepitaxy, the lattice mismatch f between the growing film and the substrate is an added parameter that influence the growth in important ways [44], some of which are listed below:

- If f is small (typically on the order of a few % points maximum), the film grows as a monocrystalline layer, adapting to the underlying substrate, but only up to a certain thickness. After this, the strain is released and the deposition proceeds by the formation and subsequent growth of defect-containing 3D islands.
- If f is large, the growth start by the nucleation of 3D defect-free islands, which can then coalesce, or a 2D layer is formed between the islands, with the final result of a single crystalline layer, usually with a rough surface. Over a certain thickness, however, defect-containing islands tend to form, due to the release of accumulated strain in the film.
- At larger still f values, the growth proceeds only by 3D island nucleation and accretion, that become defected after a certain value of the film thickness; there is no formation of a 2D layer due to the extreme mismatch with the substrate.

If the film and the substrate have different crystal structure, as it is the case with the deposition of monoclinic β-Ga_2O_3 on hexagonal α-Al_2O_3 that will be described below, other problems tend to arise. Typically, the main consequence is a tilting of the unit cell

of the growing film with respect to that of the substrate, which is also due to the different in-plane lattice parameters. Therefore there is the growth of a distorted layer, and the film tend to grow as a poly-crystal, due to the misalignment between different nucleating islands that try to adapt to the underlying structure of the substrate.

2.2.3 Metal-organic precursors

MOVPE is a chemical vapour deposition in which one or more of the precursors are organic compounds of the metal reagents, in our case trimethyl-gallium: $Ga(CH_3)_3$.

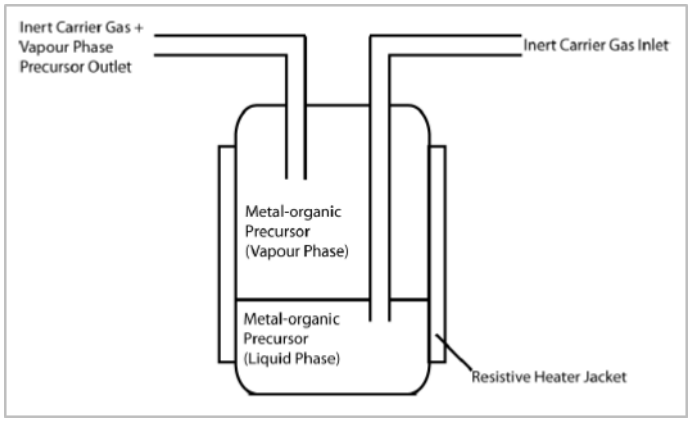

Fig. 10 Outline of the bubbler used to generate vapour of a metal-organic precursor and transport it to the reaction chamber.

The liquid metal-organic precursors and reactants are typically stored in dedicated bubblers (Fig. 10), themselves positioned thermal baths set at precise temperatures. The carrier gas is bubbled through the liquid reagents that are then transported in vapour phase to the reaction chamber.

The rate at which the precursors are supplied to the chamber is determined by the temperature at which the bubbler is held (i.e. the vapour pressure of the liquid reagent) as well as the rate at which the inert carrier gas is fed into the bubbler.

2.2.4 Atomic layer deposition

In the standard MOCVD technique, precursors are introduced into the reaction chamber simultaneously, along with the carrier gas.

An alternative technique is the *atomic layer deposition* (ALD): ALD is a deposition technique where vapour-phase precursors are introduced in the chamber separately as mono-reactant pulses, along with the carrier gas. In this way, growth is achieved through self-terminating surface reactions [45]. Self-terminating means that only a single monolayer of a reactant gas species can be adsorbed to the surface during a pulse.

Between pulses containing reactant gases, there are purging pulses where the ALD reactor is flushed with an inert gas (typically, the carrier gas is used). The purging pulses ensure that the reactant gas pulses do not mix: mixing of the reactant gas pulses would lead to continuous growth between pulses and accurate control of the reaction and the film thickness would be lost. The purging pulses also flush away reaction by-products, like detached ligands, as well as any excess reactants that are not adsorbed on the surface of the growing film.

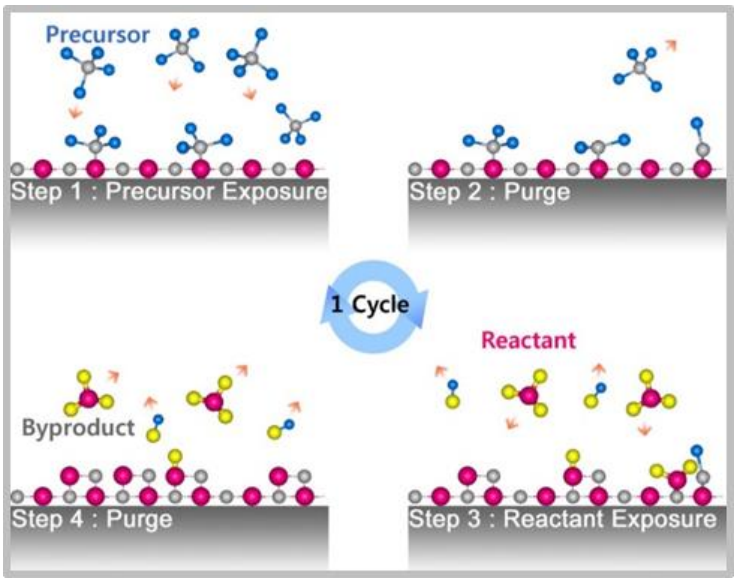

Fig. 11 ALD growth cycle for a bi-component film. Here, the metal-organic reagent is called precursor (i.e. the metal containing organic molecule), while the other is called reactant (e.g. the oxidizing agent in a metal-oxide film).

A complete set of gas pulses for every different precursor, along with the interspersed purging pulses, that is needed to deposit a single layer of the film's compound, is referred to as a cycle. If the deposition parameters have been chosen properly, the film thickness is determined by the number of cycles, rather than by the concentration of the reactant species; in fact, for every cycle, a single monolayer of film should be deposited.

Deviations from this ideal relation between the number of cycles used for deposition and the film thickness are however possible, due to phenomena like the substrate-enhanced and substrate-inhibited growth [45].

The ALD technique has various advantages over the standard MOVPE growth:

- The control over the film thickness is typically very good, in the optimal case down to a precision of a single mono-layer (about 1 nm).
- Due to the separate pulses of precursors, it is relatively easy to choose to terminate the surface of the film with one particular species.
- As the pulses are separate, surface diffusion of the adsorbed species to crystal sites is not influenced on the relative surface diffusivity of the different reactants, so that it is much easier to obtain good crystallinity at lower growth temperature with respect to classic MOVPE.
- Inert gas purging of the reaction products between pulses means that there is less incorporation of unintentional impurities, resulting in better film quality.

2.3 Growth of Ga_2O_3 thin films

Gallium oxide film were grown on the (001) plane of hexagonal α-Al_2O_3 substrates (c-plane), starting from $Ga(CH_3)_3$ (TMGa) and ultrapure H_2O reagents.

The growth was done mainly in two different conditions:

1) Depositions were done using standard MOCVD at *high substrate temperature*: T_s>700°C, and p_{H2O}/p_{TMGa}=300, (p_{H2O} and p_{TMGa} being respectively the partial pressures of H_2O and trimethyl-gallium inside the chamber), which results in a relatively *high growth rate* of the film.
2) Other growths were done at relatively *low substrate temperature* of T_s≤650°C, and *lower growth rates*, by maintaining a ratio of p_{H2O}/p_{TMGa}=4000, while using ALD deposition technique.

The flux of the gas components was set so that the total pressure inside the growth chamber, that is: $p_{tot} = p_{H2O} + p_{TMGa} + p_{H2}$ (sum of the partial pressures of H_2O, $Ga(CH_3)_3$ and the carrier gas H_2 respectively), was always set to 100 mbar.

Film of various thicknesses were grown in conditions 1) and 2) and with deposition parameters set between these two extremes.

Due to the high lattice mismatch between the alumina substrate and the Ga_2O_3 growing film, the growth proceeds always by nucleation of islands, that tend to coalesce to form a single film; the morphology of the final layer, however, depends strongly on the growth conditions.

Typically, films grown in conditions 1), i.e. high growth rate and high T_s, have a rough surface and are poly-crystalline, while those grown in conditions 2) have a smooth,

planar surface, and are single crystals. The causes of these differences are described in the following section.

2.4 SEM and XRD analysis of MOCVD-grown thin films

To determine the crystal structure and the surface morphology of thin films grown in different conditions, X-ray diffraction (XRD) and scanning electron microscopy analysis were done on various samples.

The results of these structural investigations point to the fact that films grown in conditions similar to 1) are composed of β phase gallium oxide, while film growth in condition 2) are made of ε-Ga_2O_3. These results are described and explained in the next two paragraphs.

2.4.1 β-Ga_2O_3 thin films

Films grown at Ts =715°C and high deposition rate, such as in the case of sample #54, have a rough surface due to a poly-crystalline morphology: the deposition proceeds by nucleation of islands that don't have the same crystal orientation with respect to each other and are also tilted with respect to the crystal plane of the underlying substrate; this results evident by observing the morphology of the surface of the film in Fig. 12.

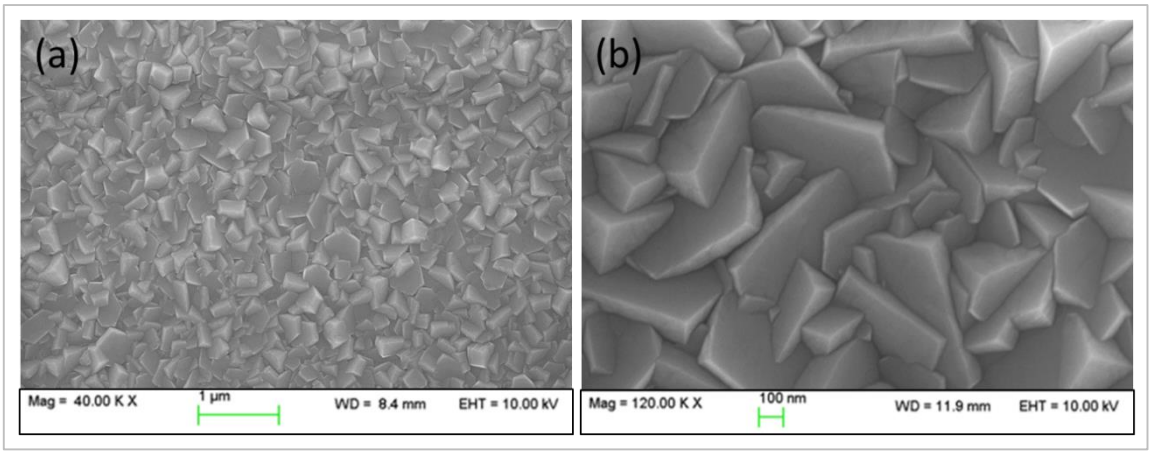

Fig. 12 (a) SEM image of the surface of a film grown at substrate temperature T_s=715°C and at high growth rates (p_{H2O}/p_{TMGa}=300). (b) Higher magnification of the same surface show clearly that the rough appearance is due to misaligned poly-crystals that have coalesced during the deposition.

X-ray diffraction data in Fig. 13 shows clearly that the Ga_2O_3 film is composed of pure β phase material, as the XRD peaks are consistent with those of bulk β-Ga_2O_3 and thin films that can be found in literature [46] [47].

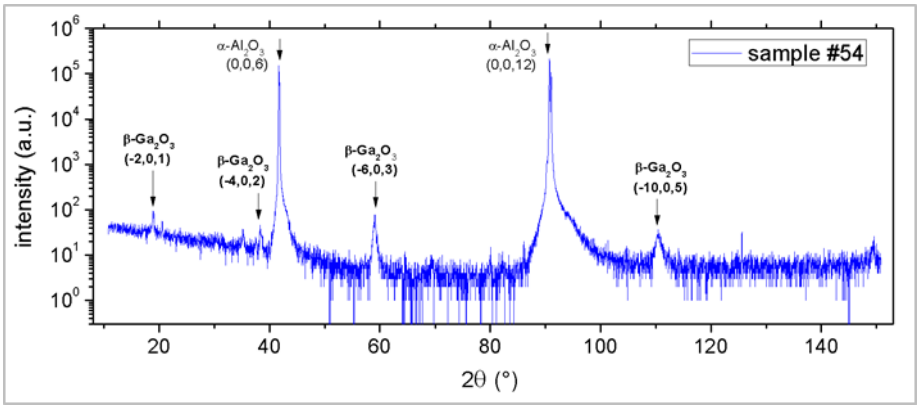

Fig. 13 XRD spectrum of sample #54, as measured x-ray intensity (in arbitrary units) as a function of the diffraction angle 2ϑ. The diffraction peak positions are consistent with those of a pure β-Ga_2O_3 thin film. Diffraction lines of the α-Al_2O_3 substrate are also present.

As evidenced by the SEM images, deposition of the β-phase on alumina substrates results in poly-crystalline growth with misaligned domains. This is due to the monoclinic structure of β-Ga_2O_3 adapting to the hexagonal (001) c-plane of the α-Al_2O_3 substrate (Fig. 14). In agreement with what was already observed in literature, the β-Ga_2O_3 film tend to grows with the (-201) parallel to the (001) plane of the substrate [47]. In addition, analysis of x-ray diffraction pole figures show diffraction peaks, split over 60° of rotation angle, indicating six types of orientations for the β-Ga_2O_3 crystals [48].

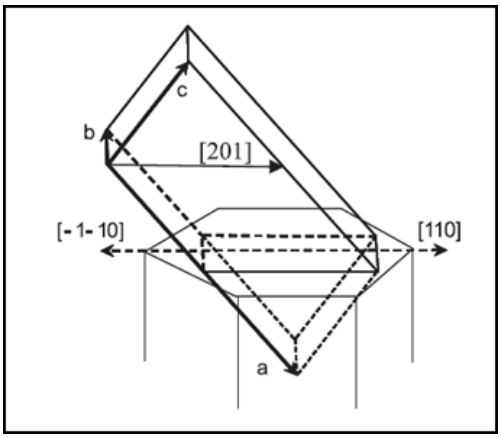

Fig. 14 Alignment of the (-201) direction of monoclinic β-Ga_2O_3 over the (001) plane of α-Al_2O_3 substrate during growth. There are 6 possible in-plane orientations of the crystal structure of the film with respect to the hexagonal Al_2O_3 below, set at an angle of 60° from each other.

Therefore the film has a strong tendency to grow as a poly-crystal, in which all the different crystallites grow in the same (-201) direction (perpendicular to the substrate), but are misaligned with respect to an in-plane axis (perpendicular to the (-201) direction). In addition, the misalignment angle is a multiple of 60°, due to the particular symmetry of the monoclinic cell with respect to the hexagonal one (i.e. to form a 6-fold symmetric unit, one needs 6 monoclinic cells oriented at 60° one to the other).

2.4.2 ε-Ga_2O_3 thin films

Samples grown at a lower temperature of T_s=650°C, and with lower growth rates using ALD deposition present a quite different morphology.

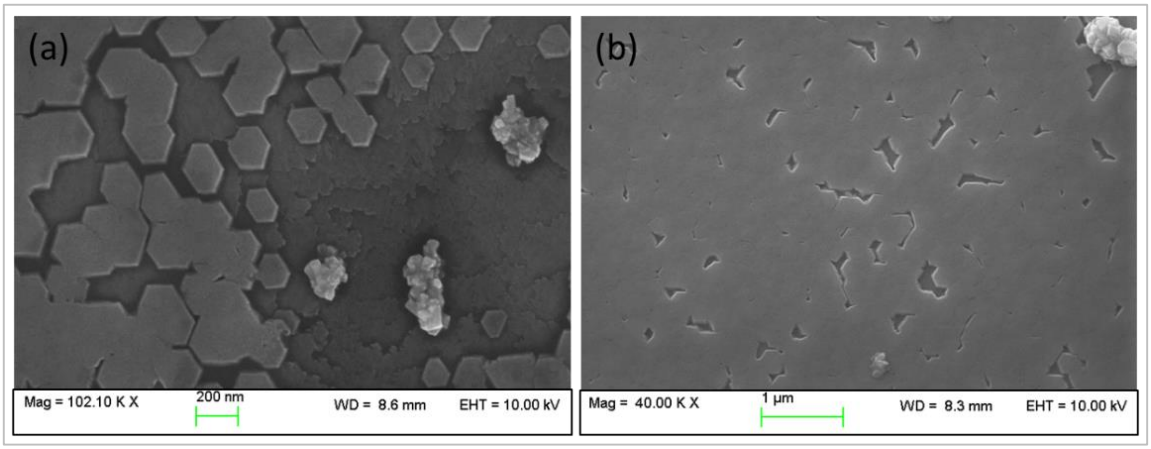

Fig. 15 (a) SEM image of the region of the film near the boundary of the substrate, where growth is incomplete. This image shows clearly that in the case of low T_s and growth rates, deposition proceeds by nucleation of hexagonal islands, which have the same orientation with each other and are seemingly not tilted with respect to the substrate. (b) In region nearer the centre of the film, the islands have coalesced almost completely, giving rise to a smooth surface.

From SEM images in Fig. 15 and Fig. 16, it is clear that the growth proceeds by islands nucleation and coalescence as before, but in this case the islands are clearly of hexagonal form, and are oriented in the same plane as the Al_2O_3 c-plane of the substrate, corresponding to the (001) direction. Moreover, the island have the same crystal orientation with respect to each other, so that when these coalesce completely, the resulting film has a smooth and planar surface.

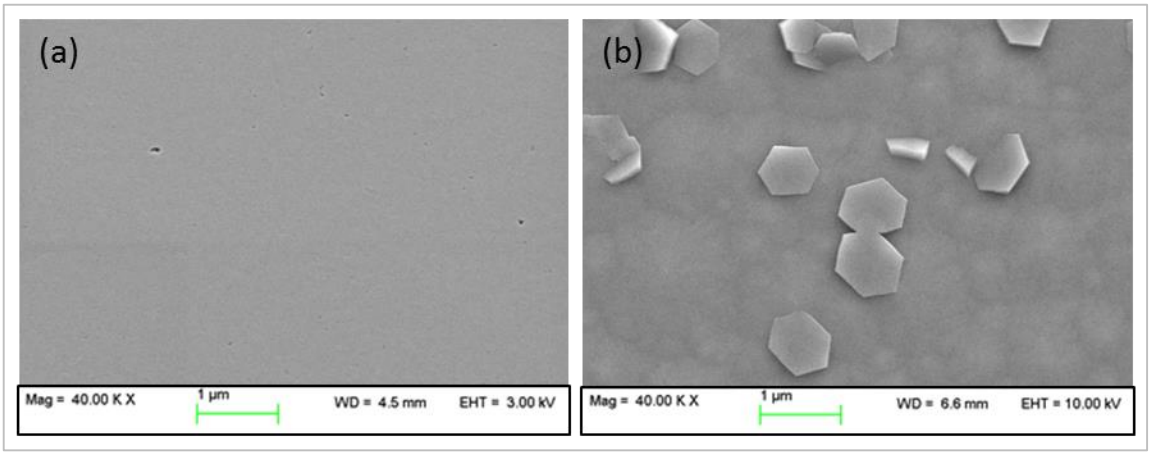

Fig. 16 (a) When there is complete coalescence, the resulting film has a smooth and plane surface. (b) The rare defect zones present highlight the hexagonal nature of the crystal structure of the layer.

X-ray diffraction data of the samples grown at low temperature (Fig. 17) show that the diffraction peaks are shifted with respect to those of β phase films. The position of all the XRD peaks, in fact, turns out to be consistent with that found in literature for a *pure ε-Ga_2O_3* sample [38] [40]. ε-Ga_2O_3 has a *hexagonal crystal structure*, that was resolved only recently (2013) by *Playford et al.* trough neutron and X-ray diffraction [38]. Before then, the ε phase was thought to be rhombohedral; the error was likely due to the difficulty of obtaining pure samples that are not contaminated by the more stable β polymorph.

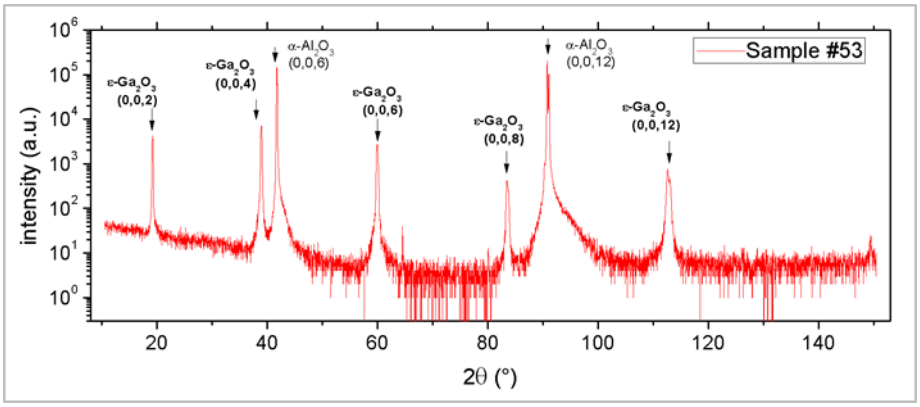

Fig. 17 XRD pattern of sample #53, growth at 650°C. The peak positions are consistent with those of the hexagonal ε-Ga2O3 phase, as described in literature [38] [40].

It is important to note that *this is the first instance* in which a ε phase film is grown on Al_2O_3 using the MO-CVD technique, in pure form, and it is recognised as such. As of 2015, there is only one paper describing the deposition of pure ε-Ga_2O_3 by *Oshima et al.* [40]; in that instance, the film was grown by halide vapour phase epitaxy on different substrates.

Another important point to note is the similarity between the XRD pattern of the ε and β phases: the diffraction peaks are found in very similar positions, and the shift between them becomes apparent only at high diffraction angles. This fact can become important, as it is difficult to distinguish between the two phases, so that it is conceivable that films assumed to be grown as β-Ga_2O_3 can in fact be made of the lesser known ε phase, or possibly a mixture of the two poly-types, a condition that we have found to occur quite often at growth temperatures lower than 650°C.

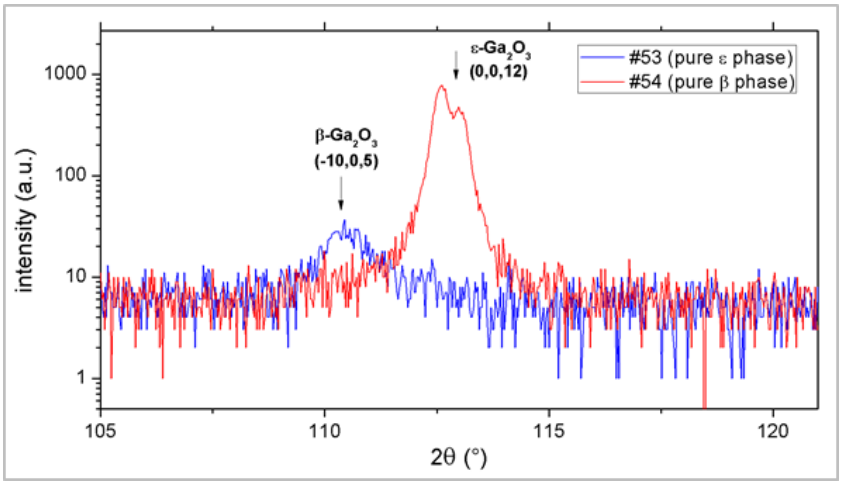

Fig. 18 The XRD peak shift between ε- and β-Ga_2O_3 samples is apparent only at high diffraction angles, due to the similarity in the atomic distances between the two phases. As the XRD spectra was obtained using a bi-chromatic source (Cu-Kα_1 and CuKα_2 lines), the diffraction peaks are split into two, as can be seen clearly from the ε-Ga_2O_3 peak.

The similarity between the XRD patterns is due to the fact that the two phases have similar inter-atomic distances, but the atoms are packed differently, giving rise to the observed XRD shift at large values of 2θ.

2.5 Absorption spectroscopy

Samples of *ε-Ga_2O_3 thin films* of different thickness were analysed using absorption spectroscopy in the ultra-violet, visible and near-infrared wavelength range (UV-VIS-NIR), in order to determine the value of the optical band gap of the material in the ε phase.

The absorption spectra were acquired in transmission mode (i.e. measuring the fraction of light intensity transmitted through the film) using a *Varian 2390 double-beam spectrophotometer*. The instrument operates in the wavelength range: 200<λ<800 nm (corresponding to photon energies: 1.55<hν<6.2 eV).

The study was carried out on a large set of films with thickness from 175 nm to 2 µm. Ga_2O_3 is effectively a *direct band gap* semiconductor (see Par. 2.1.1), and direct optical transitions are allowed, so that, assuming parabolic bands, the absorption coefficient α of the material for photon energies E_{ph}=hν (h=Planck's constant and ν=photon frequency) close to the band edge (hν≈E_g) should have the form:

$$\alpha \propto \frac{(h\nu - E_g)^{1/2}}{h\nu} \qquad (2)$$

where E_g is the value of the direct energy gap of the material, while hν is the photon energy of the incident (mono-chromatic) light, which is related to the photon wavelength λ and frequency ν trough the well-known relation:

$$E_{ph} = h\nu = \frac{hc}{\lambda} \qquad (3)$$

where h is Planck's constant and c the speed of light in vacuum.

The spectrometer measures the intensity of the light beam transmitted through the sample as a function of the photon energy $E_{ph}=h\nu$. The quantity obtained is the absorbance *A(hν)*, measured in *optical density* (OD):

$$A(h\nu) = log_{10}\frac{I(h\nu)}{I_0} \qquad (4)$$

Where *I(hν)* and I_0 are the transmitted and incident beam intensities respectively.

Transmission spectra of samples of different thickness are shown in Fig. 19. It is evident that the films start to absorb light at about 4.7 eV (≈260 nm), but the shape of the absorption edge varies widely among films of different thickness; in general, the more thick is the film, the more sharp is the edge, and vice-versa.

The absorption curve exhibits a small but detectable optical activity below the band edge down to 2 eV. Optical absorption at photon energies hν<E_g reveals the presence of energy levels in the band gap, usually defect-related.

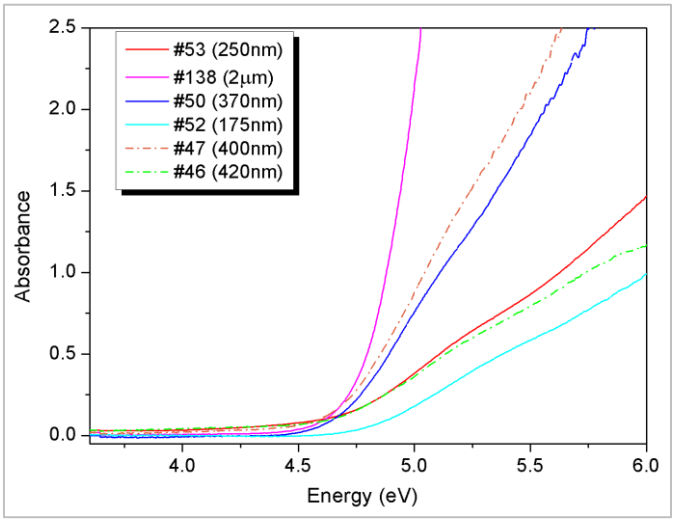

Fig. 19 Transmission spectra of various ε-Ga_2O_3 thin films of thickness between 175nm and 2µm, expressed as absorbance (in OD) vs. photon energy (in eV).

The standard way to deduce the precise value of the band gap in a direct band gap semiconductor with parabolic band, is to use the *Tauc plot* method [49] [50]. Knowing the *film thickness d*, from the absorption spectrum *A(hv)* it is possible to deduce the *absorption coefficient α(hv)* as:

$$\alpha(h\nu) = -ln10 \cdot \frac{A(h\nu)}{d} \cong -2.3\frac{A(h\nu)}{d} \qquad (5)$$

From Eq. (2), the square of the product between the absorption coefficient and the photon energy in the vicinity of the absorption edge is then related to hv by the simple linear relationship:

$$(\alpha h\nu)^2 = B \cdot (h\nu - E_g) \qquad (6)$$

where *B* is a constant, and E_g is the energy gap of the material. The Tauc plot is the plot of $(\alpha h\nu)^2$ as a function of *hv*, so that a *linear fit* of the edge region should have a zero in $h\nu = E_g$.

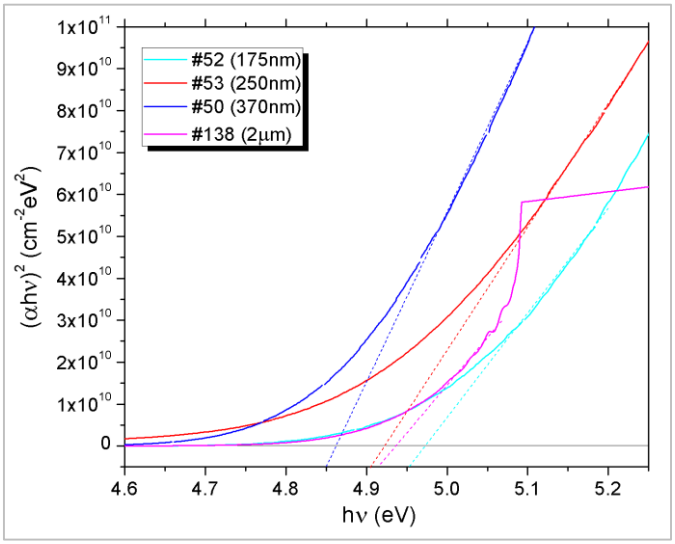

Fig. 20 Tauc plots (solid lines) for some of the ε-Ga_2O_3 thin films of different thickness. The value of the energy gap should be given by the intersection of the linear fit (dashed lines) of the absorption edge with the $(\alpha h\nu)^2=0$ line (solid black). It is evident from this graphic that a different value of E_g is obtained for films of different thickness.

As shown in Fig. 20, however, the Tauc plot representation is not suitable for a sensible evaluation of the ε-Ga_2O_3 thin films energy gap. In fact, the value of E_g obtained from this method is different from different film thicknesses, due to fact that the slope of the curve in the vicinity of the absorption edge depends strongly on film thickness.

The calculated band structure of monoclinic Ga_2O_3 [51] justifies the unfulfilling results of the Tauc plot, predicting a direct bandgap at the Γ point slightly higher (a few tens of meV) than the indirect one located just off the M point. Although vertical transitions at the Γ point are dipole-allowed and indirect dipole matrix elements decrease rapidly approaching the M-point. Poly- and/or nano-crystallinity, disorder, residual strain, co-existence of different phases could make indirect transitions possible. As a consequence, the optical band-edge could be described as a combination of different transition mechanisms. In addition, lattice anisotropy surely affects the band edge profiles, even if the bigger influence on the absorbance curves in thin films arises from the thickness of the film itself.

The increasing of the optical bandgap with decreasing the sample thickness has been already observed in amorphous silicon thin films [52], and it led to the conclusion that an absolute determination of the optical bandgap through a simple Tauc plot approach is therefore, in certain cases, undermined.

It is noteworthy that, when the thickness is just smaller than the photon penetration length, light intensity transmitted beyond the sample is not zero even at energies above

the optical gap: the thinner the film the less steep is the absorption edge. Photons with energies higher than the band gap that interact with the film can excite states that far away from conduction and valence band extrema. This in turn can drastically affect the shape of the absorption curve, as shown in Fig. 19 and in the Tauc plots of Fig. 20.

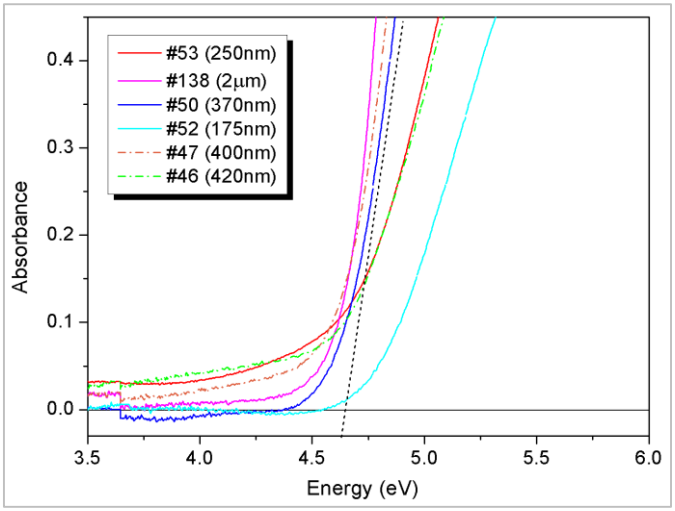

Fig. 21 Absorption edge of various films plotted to 0.45 OD. The value of the energy gap obtained is similar for all samples and is about 4.6 eV.

As shown Fig. 21, it emerges that the plot of absorbance up to optical density values corresponding to the penetration length, gives very similar curves for thickness higher than 300 nm. Curves for thinner films are highly affected by contribution from photon absorption above the band-edge, while thicker film are not, therefore the latter are more indicated to estimate the band gap value of the material. Our analysis, repeated on a large set of films with thickness between 300 nm and 2 μm, led us to estimate that the optical bandgap of ε-Ga_2O_3 is likely to fall between 4.6 eV and 4.7 eV, relatively close to that observed in bulk β-Ga_2O_3 [53].

The only optical bandgap value for ε-Ga_2O_3 available until now, calculated by *Oshima et al.* from the Tauc plot of the absorbance data of a single 670 nm thick film, was about 4.9 eV [40].

Our result indicates that the bandgap energy is quite similar to that of bulk β-Ga_2O_3 [54], and therefore, opto-electrical properties in general might be comparable for both phases.

2.6 Cathodoluminescence spectroscopy

Radiative recombinations in ε-Ga_2O_3 samples were investigated as function of the electron penetration depth by means of *cathodoluminescence spectroscopy* at room temperature.

Cathodoluminescence (CL) is an optical analysis technique in which an electron beam accelerated by a voltage of a several kV impinges on the sample surface to excite a luminescent emission, usually in the UV-VIS range of the electromagnetic spectrum. Photon emission is due to electron-hole couples generated by the high energy electrons in the material that recombine radiatively, the emitted photons have hν equal to the energy difference between the electronic levels involved in the recombination.

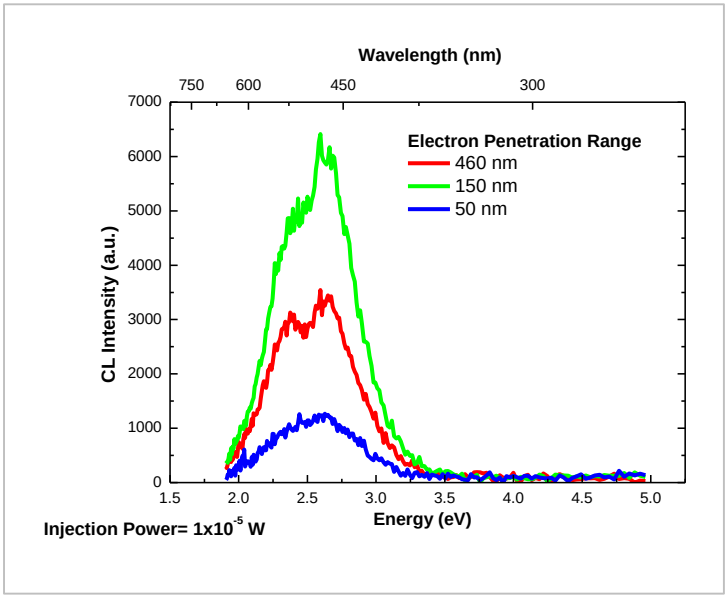

Fig. 22 Depth-resolved CL analysis. CL emission is due radiative recombination trough defect-related levels inside the energy gap.

Depth-resolved CL spectra for an ε-Ga_2O_3 thin film (red line) are reported in Fig. 22. Using a Gaussian peak deconvolution procedure, three peaks are resolved, centered at E_1=2.34 eV, E_2=2.67 eV and E_3=2.75 eV: these emissions are indicative of the presence of radiative deep centers, related to states inside the energy gap. As it is evident from the picture, the band edge emission due to radiative band-to-band transition is absent in ε-Ga_2O_3. This was also reported in the case of β-Ga_2O_3 bulk and film samples. Depth-resolved CL analysis is thus used in order to study the depth resolved distribution of the intra-gap radiative recombination centers inside the samples [55] [56]. To obtain the

depth-resolved CL analysis, the accelerating voltage was varied between 2.5 keV and 10 keV, in order to vary the electron penetration range from 50 to 450 nm. The value of the penetrating depth of the electrons was obtained through the implementation of Monte Carlo simulations; an example of the simulation's results is showed in Fig. 23. The electron beam interact with the sample in a quasi-spherical region called the interaction volume; photon are emitted only from this circumscribed region, and simulations show that the mean depth at which the electron beam energy is deposited inside the sample depends strongly on the energy of the beam itself.

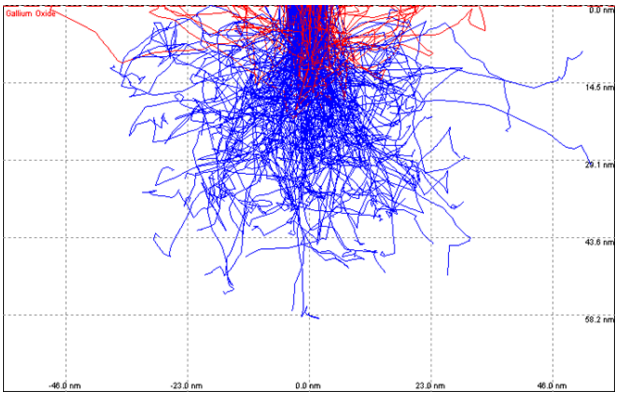

Fig. 23 Monte Carlo simulation of the trajectories of electrons inside a Ga2O3 thin film sample. Red lines correspond to paths of electrons that have left the material after entering it, due to repeated collisions. Blue lines indicate electrons that stopped inside the sample.

Fig. 24 reports the integrated intensity of the single emissions as function of the electron penetration depth of thin film, showing a deep inhomogeneity in the depth distribution of the radiative recombination centers; the highest integrated intensity is obtained at 5 keV (green line), corresponding to a depth of 150 nm. It is worth noting that the generation-recombination volume, using an accelerating voltage of 10 keV, crosses the interface with the underlying sapphire substrate, and therefore a part of the energy released by the electron beam is dispersed in the Al_2O_3 layer. At 2.5 keV (electron penetration range = 50 nm), the CL integrated intensity is weak probably due to a large concentration of non-radiative recombination centers near the surface. Non-radiative centers are probably caused by a high concentration of defects in the surface region of the film. The origin of the CL emissions in ε-Ga_2O_3 requires more detailed study, but comparing these results to the literature on β-Ga_2O_3, it is possible to suppose that the emissions reported in this work are related to donor-acceptor pairs due to point-defects [57].

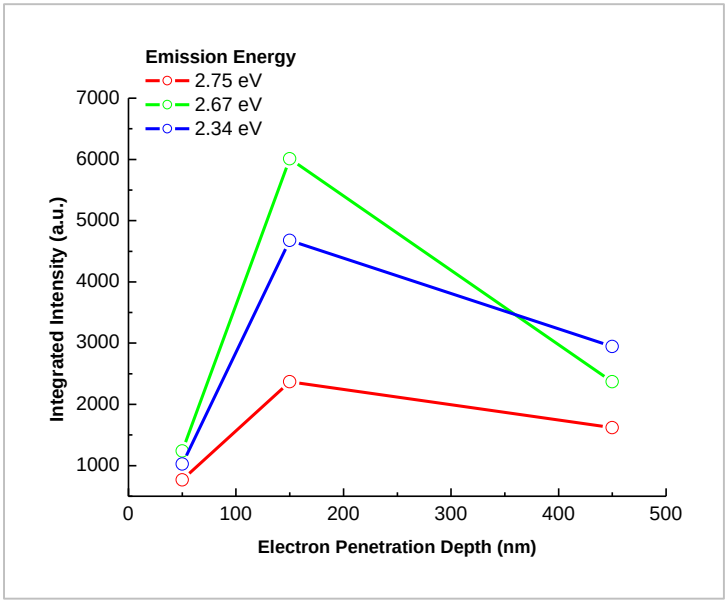

Fig. 24 CL integrated intensity as function of the electron penetration depth.

2.7 Contact deposition and electric measurements

To evaluate the electric characteristics of ε-Ga_2O_3 thin films, electrodes were obtained by thermal evaporation of metals on the surface of two ε-Ga_2O_3 layers of thickness 370 and 250 nm (sample #40 and #53 respectively), deposited on Al_2O_3 substrates. In this way, *single-face planar metal-semiconductor-metal* devices were obtained (see **Errore. L'origine riferimento non è stata trovata.**). The physical dimensions of the samples, cut from Ga_2O_3 thin films of 2" diameter, are about 2x2 cm.

Each *double layer* metal electrode consist of a 100 nm thick Au layer on top of 50 nm of Ti. The layers were easily deposited through a metal mask by thermal evaporation in vacuum, and the metal deposition shows very good adhesion properties on the ε-Ga_2O_3 film. In this way, we obtained thin film large-area *UV photodetectors* with a distance between the electrical contacts of about 2 mm.

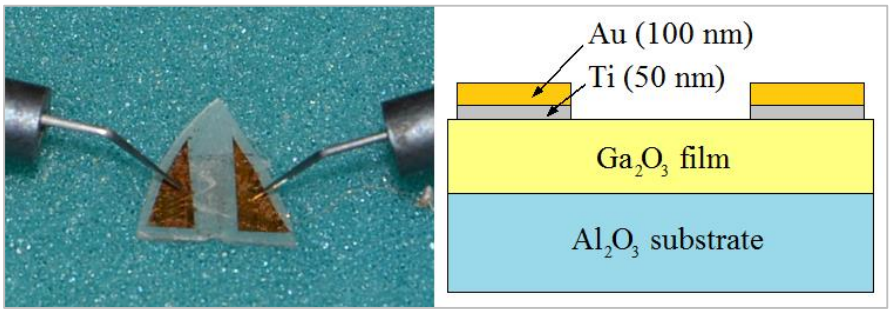

Fig. 25 Picture of an ε-Ga_2O_3 thin film sample with deposited Au/Ti planar contacts (left), along with the cross-section schematics of the sample (right).

The *current vs. voltage characteristics* (IV) of the devices were acquired at room temperature using a *Keithley 2400 source-meter* apparatus. The current was measured in dark conditions between -200 and +200 V, in order to evaluate the characteristics of the deposited metal electrodes and to obtain an estimation of the resistivity of the ε-Ga_2O_3 thin films.

The curve in Fig. 26 is the measured IV characteristic of sample #53. Due to the high resistivity of the films and the small dimensions and thickness of the devices, the current in the dark is extremely low, on the order of few tens of pA, even at 200 V; as the measured currents are close to the sensitivity limits of the measuring instrument, the IV characteristic shows a relatively high signal-to-noise ratio. However, the current dependence on the voltage is clearly linear: this point to the fact that the Au/Ti contacts behaviour is *ohmic*.

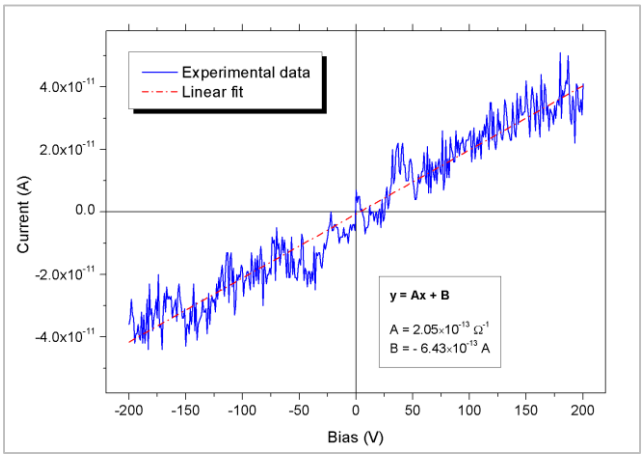

Fig. 26 IV characteristic of an ε-Ga_2O_3 thin film based photo-detector measured at RT in dark conditions. The data were fitted with a linear equation to obtain the resistance of the gallium oxide layer (thickness 250 nm).

The current-voltage curve was then fitted linearly to extrapolate the *resistance R* of the film, and the obtained value is:

$$R = (4.88 \pm 0.06) \cdot 10^{12}\ \Omega$$

From this, the *resistivity ρ* of the material was estimated:

$$\rho = (1.52 \pm 0.02) \cdot 10^{9}\ \Omega \cdot cm$$

From this value, it is possible to estimate the carrier concentration inside the material using the well-known relation:

$$\sigma = \frac{1}{\rho} = e\mu_e n \qquad (7)$$

Where σ is the electric conductivity (reciprocal of the resistivity), e is the elementary electron charge (e = 1.6022 ·10^{-19} C), μ_e is the electron mobility and n the concentration of carriers, in this case electrons. Only electrons appear in Eq. (7) because of the negligible hole mobility μ_h with respect to μ_e, that makes electron the dominant charge carriers in Ga_2O_3 (as in most metal-oxides, see Par. 1.2).

Using the value for the electron mobility μ_e = 300 cm^2/V·s [8], the electron concentration n was estimated as:

$$n = (1.4 \pm 0.2) \cdot 10^{7}\ cm^{-3}$$

The measured ε-Ga_2O_3 thin films were thus demonstrated to have *good semi-insulating properties*, which are necessary for photo-detector applications; this is in strike contrast with what is reported for bulk Ga_2O_3 grown from the melt, which typically grows with high unintentional n-type doping, probably due to intrinsic defects like oxygen vacancies.

Moreover, easy deposition of metallic contacts was demonstrated on ε-Ga_2O_3 thin films, with good ohmicity and reliability. For comparison, ohmic contacts cannot be obtained reliably on β-Ga_2O_3 thin films (i.e. films grown at higher temperatures), while ohmic contacts on β-phase bulk crystals grown from melt, as reported in literature, required complex deposition techniques such as reactive ion etching and post-process Si ion implanting to work properly [8] [32].

2.8 Photo-current characterization

The *photo-response properties* of ε-Ga_2O_3 thin film photo-detectors were studied to deduce the sensitivity, selectivity and response time toward UV light of the devices.

The photocurrent measurement apparatus consists of a 350 W xenon-filled arc light source with high emission intensity in the UV-VIS region of the spectrum, between 200 and 800 nm. The current response of the detectors is then measured using the Keithley 2400 source meter as before.

2.8.1 Time evolution of the photo-current

The rise time of the photocurrent (PC) in the sample was examined at constant temperature and humidity using white light at various intensities, to investigate response time and linearity of the devices. The detector was biased at 100 V, the dark current at this voltage being I_{dark}=25 pA.

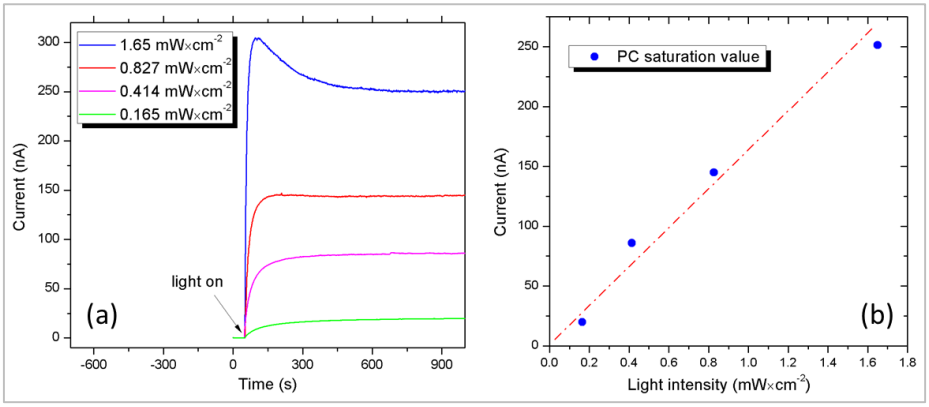

Fig. 27 a) PC vs. time plot of sample #53 at 100 V in white light of different intensities. Illumination is turned on at the instant t_0=50 s. b) Plot of the equilibrium value reached by the current as a function of light intensity showing a linear relationship.

As is evident from Fig. 27-a, the rise time of the photocurrent is relatively slow, taking a few seconds to reach the saturation value, as is usual for metal-oxide semiconductor materials. However the rise time depends on light intensity, becoming faster as the intensity increase. It is important to note that the current in the detector rise strongly when it is illuminated with UV light, increasing up to several thousand times.

Finally, the saturation value of the photocurrent increase linearly with the intensity of the incident light (Fig. 27-b); this property is in itself very important for UV opto-electronic applications, and, in addition, signifies that the detector can handle relatively high photon fluxes without being saturated, losing linearity.

The device show also good reproducibility under repeated on-off cycles, even when illuminated with high intensity UV light, and the current returns rapidly to the dark value after the light is turned off without persistent photocurrent effects that can be observed.

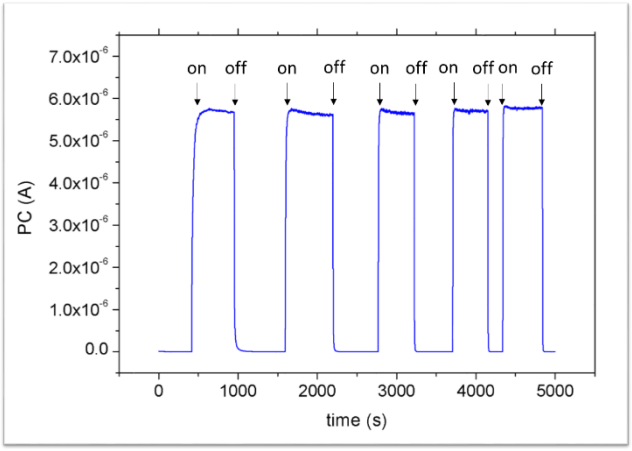

Fig. 28 Photo-current at 210 V of the device after several on-off cycles of illumination with white light.

2.8.2 Photocurrent spectroscopy

Spectroscopic analysis of the PC response of the samples was done in order to characterize the material properties as well as the performance of the UV detectors.

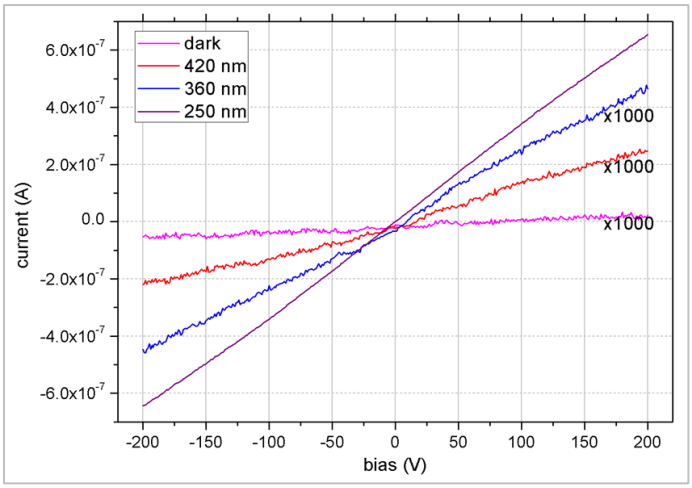

Fig. 29 IV characteristic of ε-Ga_2O_3 UV detector under illumination with 3 different wavelengths (420, 360 and 250 nm) compared with the dark IV.

Current voltage characteristics of the detector were measured under illumination with light at different wavelengths, and the results are reported in Fig. 29.

The device was illuminated with light of 420 and 360 nm wavelength, corresponding to photon energies (hν=2.95 and 3.44 eV respectively) below estimated the band gap of the material, and with above-gap energy light of λ=250 nm (corresponding to hν=4.96 eV), to determine the behaviour of the detector in different conditions.

The characteristics are clearly approximately linear in all conditions between -210 and +210 V: this fact shows that the Au/Ti electrodes behave in an ohmic way even under illumination, other than in the dark. The ohmic behaviour of the contacts under light is evidence that the energy barrier between the metal and the semiconductor is not influenced by light irradiation of energy either below or above the band gap. There is a slight deviation from linearity at high bias when the detector exposed to light of $h\nu > E_g$, corresponding to a slight back-to-back Schottky behaviour of the electrodes at high carrier concentrations that tends to limit the current that traverse the device at high bias. This tendency can be considered negligible, as the effect is small and only apparent at higher than normal operating bias.

	R (Ω)	δR (Ω)	ρ (Ω·cm)	δρ (Ω·cm)	n (cm^{-3})	δn (cm^{-3})	$\Delta n/n_0$
dark	4.29E+12	1.27E+11	1.34E+09	3.16E+07	1.55E+07	3.66E+05	0.00
λ=420 nm	7.42E+11	6.18E+09	2.32E+08	1.54E+06	8.97E+07	5.97E+05	4.78
λ=360 nm	3.98E+11	2.49E+09	1.24E+08	6.22E+05	1.67E+08	8.35E+05	9.77
λ=250 nm	2.92E+08	1.08E+05	9.12E+04	27.08	2.28E+11	6.78E+07	14702

Table 4 Device properties obtained from the linear fit of the IV curves in the dark and under illumination with light at different wavelengths. R is the resistance of the detector, while ρ and n are the estimated values of the resistivity and carrier concentration in the material. $\Delta n/n_0=(n-n_0)/n_0$ is the relative increase in the carrier concentration with respect to the dark value n_0.

As can be readily observed from Fig. 29 and Table 4, the below gap photo-response is not zero: this correspond to light absorption and carrier generation from states inside the gap, probably caused by intrinsic point defects like oxygen or metal vacancies or complexes. However, below gap generation is extremely low when compared to photo-current response above the band edge, which is at least 3 order of magnitude larger. This is important for the development of deep UV photo-detectors that have the property of being blind (i.e. with very low sensitivity) to visible and near-UV light. *Visible-blind* (a.k.a. *solar-blind*) *UV photo-detectors* find application in a range of technological field, from solar astronomy to missile guidance, among others.

The *rise time* of the photocurrent, as stated earlier, is relatively slow, being on the order of a few seconds. However, the time constant of the PC rise depend strongly on the

wavelength of the incident radiation. These constants were determined by measuring the PC vs. time response of the device for a number of different wavelengths in the range 240-580 nm.

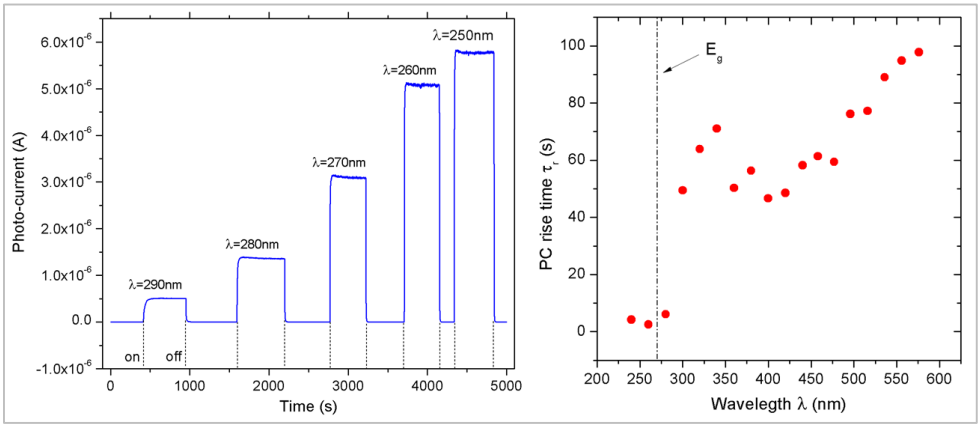

Fig. 30 (Left) Example of the change in shape of the PC vs. time curves as the wavelength of the incident light approaches the band edge at 270 nm. (Right) Time constant τ_r of the PC rise obtained by simple exponential fitting of the PC vs. time curves as a function of the incident light wavelength. The position of the band edge is reported as E_g.

In Fig. 30 (left) the data corresponding to 290<λ<250 nm are reported, showing how the shape of the PC vs. time curve changes when the photon energy hv approaches the band gap of the material at E_g≈4.6 eV (corresponding to λ≈270 nm), becoming more "squared" due to the current rapidly reaching the saturation value. To calculate *the rise time* τ_r of the PC *as a function of* λ, the curves were fitted by a simple exponential equation:

$$I(t) = I_0 + A(1 - e^{-t/\tau_r}) \qquad (8)$$

The obtained values of τ_r as a function of λ are reported in Fig. 30 (right), showing that the rise time is relatively long at photon energies hv<<E_g, but tend to decrease rapidly as hv approaches E_g, becoming comparable with about one second at hv≈E_g; as Δt=1 s is the time resolution of our measurement, the true value of the rise time τ_r is probably shorter.

The saturation value reached by the photocurrent as a function of the wavelength of incident light was then used to construct the photocurrent spectra of the ε-Ga_2O_3 devices. PC spectra can give information about electronic transitions between energy levels occurring in the material, that result in the generation of electrons in the conduction band or holes in the valence band, which give rise to the photocurrent.

The PC spectra for samples #40 and #53 were measured under a 200 V bias, at constant temperature of 25°C and humidity, using a Cornerstone diffraction grating mono-

chromator and the same light source and electric apparatus as before. The obtained photocurrent vs. photon energy $I_{PC}(hv)$ curves are reported in Fig. 31.

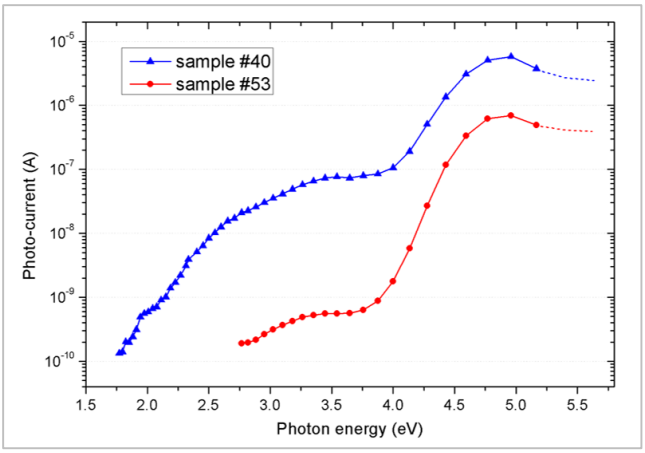

Fig. 31 PC spectra taken at 200V of the two ε-Ga_2O_3 thin film photodetectors #40 and #53. The dashed line at high energies signals the range in which the instrumental apparatus becomes unreliable.

The spectra show that the two samples #40 and #53 (of thickness 370 and 250 nm respectively) have a very similar photocurrent dependence on the photon energy, indicating similar properties of the ε-Ga_2O_3 layers the samples are made of. The PC has different magnitude in the two sample mainly because of geometrical differences.

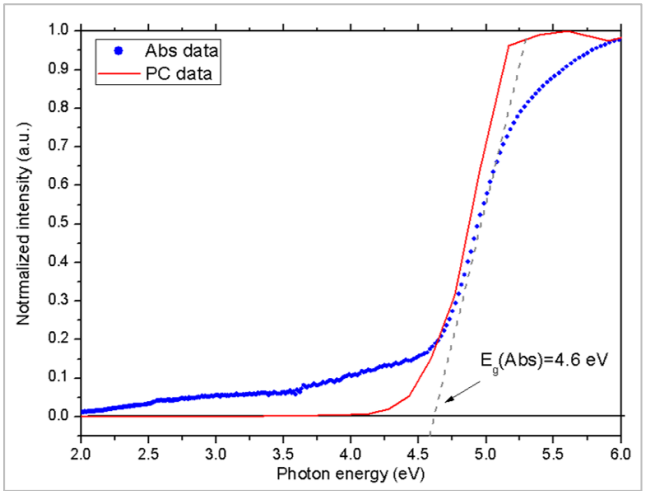

Fig. 32 Comparison of the PC spectrum of sample #53 with the absorption spectrum of the same sample. The value of the optical band gap $E_g(Abs)$ is also reported.

Comparison with the absorption spectra of the same samples show very similar trends, as expected. There is a very low but measurable response for $h\nu<E_g$ down to about 2 eV for sample #40, in agreement with the illuminated IV data: PC spectroscopy is particularly sensitive in a semi-insulating material, and even a very low change in the free carrier density can be detected thanks to very low conductivity in the dark.

The fast increase of photoconductivity at about 4 eV places the *mobility edge* slightly below the absorption edge, as can be observed in Fig. 32. This result could be justified by the presence of a high concentration of point defects or complexes with energy levels located up to 0.5÷1 eV over the top of the valence band, as was already observed in β-Ga_2O_3 [58].

Importantly, The devices are highly sensitive to UV light, with maximum responsivity reached at about 4.6 eV; the PC increase 5-6 order of magnitude over the dark current, which is I_{dark}≈10 pA at 200 V, and the response to light with hν close to E_g is at least 100 times higher than below gap.

The opto-electronic properties of ε-Ga_2O_3 thin films are thus demonstrated to be optimal for developing UV photodetectors that are sensitive to light with λ<300 nm, but, at the same time being transparent and relatively insensitive to visible and near infra-red light.

2.9 Temperature dependence of conductivity

The *temperature dependence of the dark conductivity* of the devices was studied using a climate-controlled chamber in an inert gas atmosphere. The inert gas (dry nitrogen) function was to completely remove humidity and to obtain uniform temperature throughout the material by thermal convection.

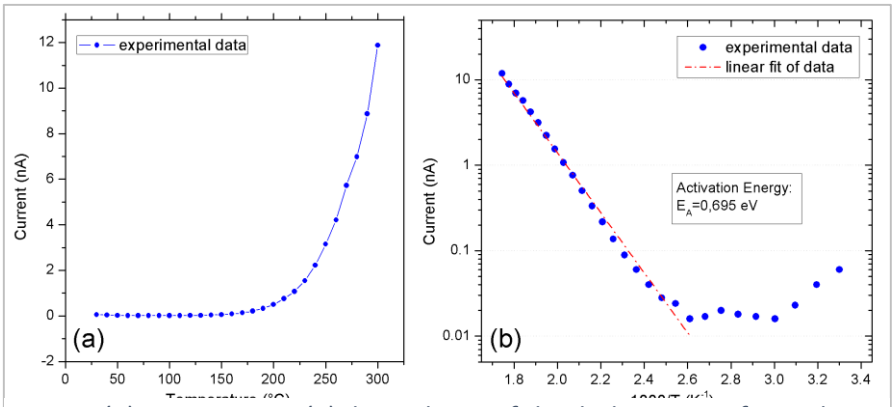

Fig. 33 (a) Temperature (T) dependence of the dark current of sample #40 between RT and 300°C. (b) Arrhenius plot of the same measurement giving an activation energy E_a = 0.695 eV.

As evidenced in Fig. 33-a, the current *I* grows *exponentially* as the temperature *T* increases from 25 to 300°C. The current grow is due to an increase in thermally generated carriers, and becomes not negligible only at about T>150°C. The general form of the thermal dependence is thus of the simple form:

$$I(T) = I(T_0) + Ae^{-E_a/kT} \quad (9)$$

Where T_0 is the initial temperature (RT), *A* is a proportionality constant, *k* is Boltzmann constant and E_a is the *activation energy* of the process responsible for the current increase.

The value of E_a can then be determined plotting the current in a logarithmic scale as a function of the inverse of T. The linear fit of the curve thus obtained gives the value of the activation energy as the slope of the line (see Fig. 33-b).

In this case, the value obtained is:

$$E_a = 0.69 \pm 0.01\ eV$$

For other samples the result is consistently near E_a=0.7 eV, as in this case, indicating that the result is evidence of an intrinsic characteristic of the material.

The value of 0.7 eV is probably the energy difference between a surface-related defect level inside the gap of ε-Ga_2O_3 and the conduction band. This level may function as an electron trap in normal conditions, and can be excited at higher temperature to release electrons in the conduction band, increasing the conductivity of the material.

2.10 Thermal annealing

We have determined at the beginning of the chapter that depositions at high temperatures (T>700°C) tend to produce β-Ga_2O_3 films, while at lower temperatures, the films are grown in the ε-phase, the optimal T value being 650°C.

To determine the thermal stability of ε-Ga_2O_3 samples and try to control the ε→β phase transition, thermal annealing experiments were done on ε-Ga_2O_3 thin film samples, and the results were characterized by XRD and CL techniques.

Annealing experiments were done for 6 hours at 1000°C in a pure oxygen flux to prevent evaporation of oxygen from the film with formation of vacancies.

X-ray diffraction of the sample before and after annealing was measured using a bi-chromatic Cu-$K\alpha_1$ + Cu-$K\alpha_2$ X-ray beam. A detail of the XRD spectra of the sample before and after annealing, compared with *bulk* β-Ga_2O_3, is reported in Fig. 34.

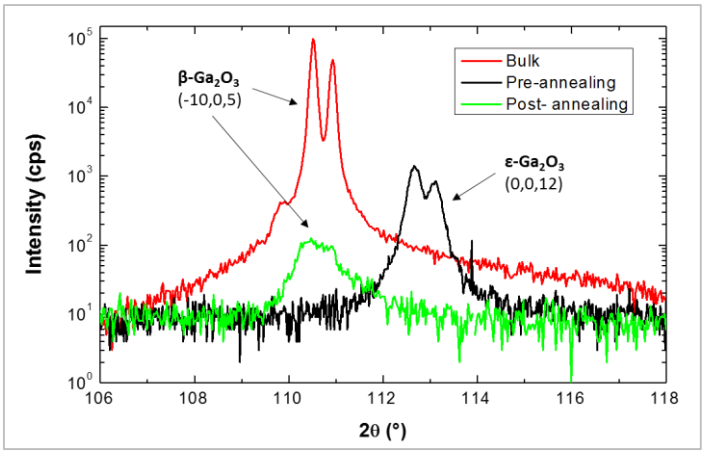

Fig. 34 High diffraction angle (2ϑ) XRD spectra of the sample before and after thermal annealing at 100°C in O_2 flux. ϐ-Ga_2O_3 spectrum is inserted for comparison.

From the XRD spectra is clear that the annealing process resulted in the phase transition of the thin film *from pure ε-Ga_2O_3 to pure ϐ*: i.e. there was *complete phase transition* of the crystal. This is evidenced by the shift in the diffraction peak from the ε (0,0,12) position before the annealing, to the β (-10,0,5) position after, which is consistent with that of a melt-grown β-Ga_2O_3 single crystal. However, as evidenced by the less intense diffraction peaks, the crystal quality is probably inferior after the annealing

Cathodoluminescence investigation of the before and after annealing conditions reinforce this interpretation, as there is a shift in the CL defect peak from about 2.6 eV, which is typical of the ε phase, to ≈3.2 eV, again consistent with a bulk β-Ga_2O_3 single crystal sample measured for comparison (see Fig. 35).

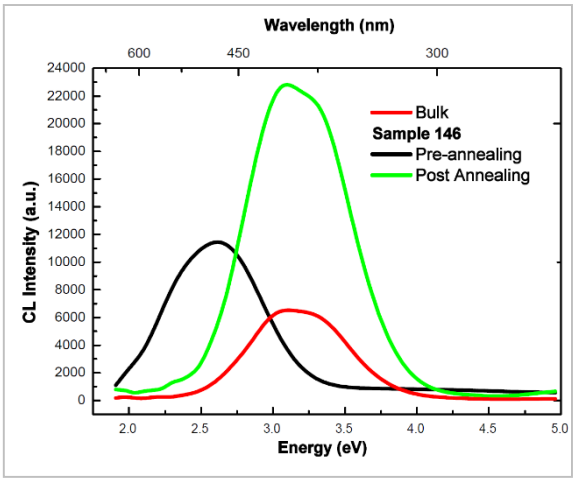

Fig. 35 CL spectra of a Ga_2O_3 thin film sample measured before and after annealing at 1000°C. Results are consistent with a ε to ϐ phase transition, as evidenced by the peak shift in a position corresponding to the emission of a bulk ϐ-Ga_2O_3 sample.

Moreover, it is important to note the increase in intensity of the defect emission after the ε→β phase transition: as these emissions correspond predominantly to defect levels close to the film surface, higher intensity should correspond to higher surface defect density. These CL spectra therefore reinforce the interpretation that the surface of β-Ga_2O_3 thin films is generally more defective than that of ε-Ga_2O_3 samples. This is probably the reason why ohmic metallic contacts are easier to deposit on ε-phase samples; the ε-phase thus tend to be better in most respect, but must not be heated over the phase transition temperature to remain stable.

2.11 Conclusions

The possibility of growing ε-Ga_2O_3 on α-Al_2O_3 at relatively low temperatures was demonstrated by XRD and CL analysis. As ε-Ga_2O_3 is hexagonal, and thin films grown in this phase have very good and planar surfaces with lower defectivity with respect to β-Ga_2O_3, as demonstrated by depth resolved CL analysis. Therefore ε-Ga_2O_3 can be a better alternative than β-Ga_2O_3 for low-cost substrates used in the epitaxial grown of GaN thin films (lattice parameter a_{GaN}=3.18 Å) [37], as both have hexagonal crystal structure, while the in-plane lattice parameter of ε-gallium oxide is a_ε=2.88 Å (quite similar to that of β-Ga_2O_3), that is sufficiently matched to that of GaN as to permit heteroepitaxial deposition. In fact, GaN can grow even on α-Al_2O_3, that have a much larger parameter of 4.75Å.

Absorption spectroscopy of the samples of ε-Ga_2O_3 thin films showed a peculiar shape of the optical band edge which made difficult the measurement of the optical band gap of the material. Nevertheless, E_g was estimated at about 4.6 eV, a value that is only slightly less than the 4.57-4.72eV of β-Ga_2O_3 (depending on the direction of polarization), thus demonstrating the comparable wide gap properties of the two phases.

Metallic electrodes with ohmic characteristics can be easily deposited on ε-Ga_2O_3 by thermal evaporation of Au/Ti bilayers. The reliability, durability and good ohmic behaviour in all testing conditions of these contacts are contrasted with the difficulty and complexity of ohmic contact deposition on β-Ga_2O_3 [8] [32]. The probable cause of this is related to the better surface properties of ε-phase Ga_2O_3 described before as well as a lower surface energy barrier. Moreover, by electrical investigation, the thin films were demonstrated to have very high electrical, resistivity thus good semi-insulating properties, which are necessary for most opto-electronic applications.

A low-cost, simple UV detector was obtained from two different samples of ε-Ga_2O_3 thin films; opto-electronical characterization of the devices showed very good sensitivity to UV light with λ<280 nm, thanks to the high resistivity of ε-Ga_2O_3 grown by MOCVD, as well as good reproducibility and reliability. Photo-current response of the detectors to below-gap-energy light is present, but 10^3 to 10^6 times lower in intensity than above-

gap PC, thus demonstrating the suitability of the described devices to solar- (or visible-) blind deep UV detectors.

Solar-blind UV detectors are one of the main applications of Ga_2O_3 [4] [58], and this is the first time solar blind-UV detectors based on ε-phase Ga_2O_3 thin films are demonstrated, and their properties described.

Finally, thermal annealing experiments were done on ε-Ga_2O_3 thin films at 1000°C in O_2 atmosphere, and the complete ε→β phase transition of the samples was demonstrated. However, to precisely pinpoint the transition temperature, other thermal treatments at lower temperatures must be implemented in the future.

The thermal stability of ε-Ga_2O_3 thin films is of extreme importance for most applications as the β phase is more thermodynamically stable, while the ε-phase has better opto-electronic and morphological properties, thus is important to determine the transition conditions to avoid them during device operation to avoid an irreversible degradation of the quality of the device.

3 ZnO nano-tetrapods

This chapter describes the experimental results on samples made from ZnO nano-tetrapods grown from vapour deposited as a film between Au contacts on an insulating substrate. These samples were developed as gas sensing detectors, due to the sensitivity of ZnO conductivity to surface adsorbed species. The experimental techniques descried in this chapter aim at analysing the opto-electronic characteristics of the nano-tetrapod films in various conditions and oxygen partial pressures.

3.1 Introduction to ZnO and its nano-structures

ZnO is a II-VI metal-oxide semiconductor that is very promising material for semiconductor device applications [59] [60] [61]. It has a *direct* and *wide band gap* of about 3.3 eV [2], and a large free-exciton binding energy of 60 meV [16], so that excitonic emission can be observed even at room temperature.

3.1.1 Crystal structure

Zinc oxide crystallizes in two main forms, *hexagonal wurtzite* and *cubic zincblende*. The wurtzite structure is the most stable at ambient conditions and thus ZnO typically crystallizes in this phase; the space group of wurtzite structure is $P6_3mc$, with lattice parameters a=3.25 Å and c=5.2 Å. In both phases, the zinc and oxide centers have *tetrahedral symmetry*, which the most characteristic geometry for Zn(II). The structure of hexagonal ZnO is schematized in Fig. 36-a.

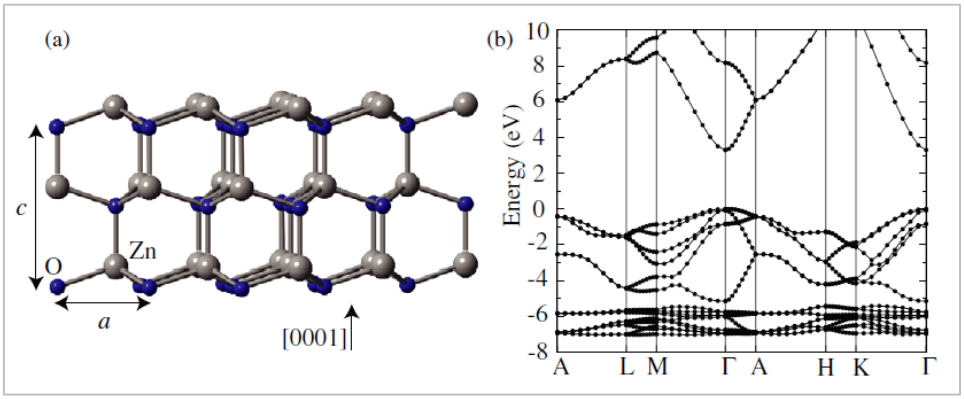

Fig. 36 (a) ZnO wurtzite ($P6_3mc$) crystal structure with lattice parameters a and c indicated. (b) Calculated band structure of ZnO using HSE hybrid functionals [16]. The energy of the valence-band maximum (VBM) is set to zero.

We already introduced in Par. 1.1 that one of the properties of most metal oxides is the possibility of growing nano-structures easily and with simple techniques.

Zinc oxide is remarkable in this respect because it shows probably the largest array of different self-assembled nano-crystalline structures among metal-oxide materials.

Other than nano-crystal shapes like nano-particles, nano-rods, nano-ribbons, etc., ZnO displays the tendency to grow in a variety of *branched nanostructures*. These are nano-structures in which ZnO (usually hexagonal) nanorods branch out from either a *core* or *trunk* ZnO parent crystal, which can be composed of the same crystal phase (i.e. wurtzite) or a different one (i.e. zincblende) [62]. One of the simplest branched nano-crystals is the *tetrapod* [63] [64]. This consists of four rod-shaped hexagonal rod-like structures, joined at tetrahedral angles to a central core [65] [66].

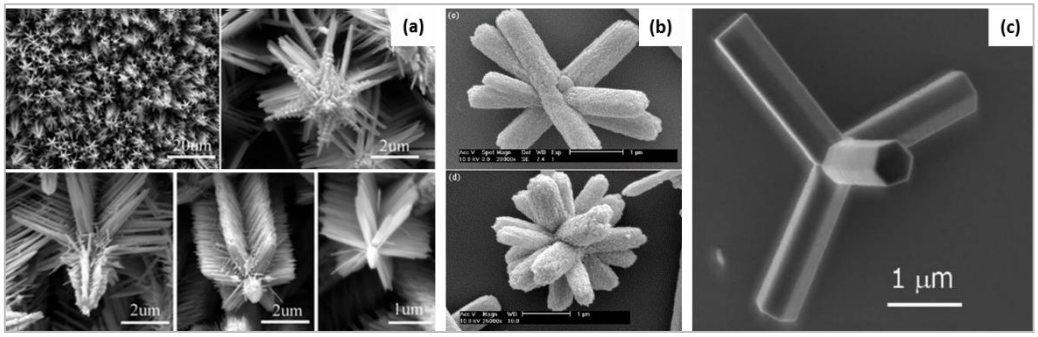

Fig. 37 SEM micrograph of branched ZnO nano-structures: (a) trunk-branched ("nano-trees"), (b) core-branched and (c) tetrapod.

3.1.2 Electronic properties

The properties of this material have been studied since the 1950s, but the use of ZnO as a semiconductor for electronics has been hindered by the difficulty of controlling its electrical conductivity. In fact, ZnO crystals grow intrinsically n-type, which is common for metal-oxides, and the cause of the preferentially n-type conductivity has been a matter of extensive debate and research [16] [59] [60] [61]. For a long time it has been postulated that the unintentional n-type conductivity in ZnO was caused by the presence of oxygen vacancies or zinc interstitials. However, recent DFT calculations, along with by optically detected EPR measurements on high quality ZnO crystals, have demonstrated that this attribution to native defects cannot be correct, showing instead that V_O are actually deep donors, and other point defects (e.g. Zn interstitials and antisites) are also unlikely causes of the observed n-type conductivity [2] [16] [67]. Instead, the cause would be related to the unintentional incorporation of impurities that act as shallow donors, such as hydrogen, which is present in almost all growth and processing environments [18].

3.1.3 Gas sensing properties

As was already pointed out in Par. 1.3.2, sensitivity to atmospheric conditions is a fundamental property of electronic transport in most metal-oxides, that is the basic mechanism for gas sensing applications [9] [10]. ZnO is one of the most important gas sensing materials, along with SnO_2 and In_2O_3.

The mechanism by which electron conduction is influenced by the partial pressure of gases, mainly *oxygen* is not completely understood; however, there is a general consensus over the qualitative explanation of the phenomenon.

Typically, oxygen molecules are adsorbed on the ZnO crystal surface in air. Adsorbed oxygen species can capture electrons from the bulk of the crystal forming O_2^- trough the reaction:

$$O_2(g) + e^- \rightarrow O_2^-(ads)$$

The negative charge trapped in these oxygen species causes a *surface depletion layer* and thus a reduced conductivity by decreasing the width of the neutral conducting channel in the bulk of the crystal. When the partial pressure of O_2 is reduced, or the material is exposed to reducing gases, the electrons trapped by the oxygen adsorbate will return to the bulk of ZnO, leading to a decrease in the potential barrier height and thus an increase in conductivity [10] [68].

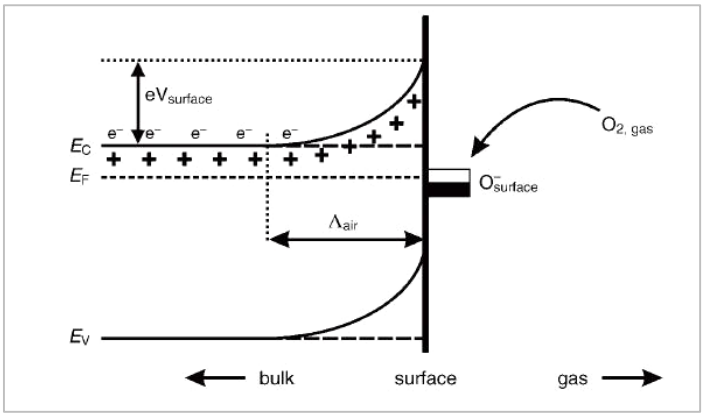

Fig. 38 Diagram of the band bending after chemisorption of charged oxygen species. E_C, E_V, and E_F denote the energy of the conduction band, valence band, and the Fermi level, respectively, while Λ_{air} is the thickness of adsorption-induced depletion layer, and $eV_{surface}$ the surface potential barrier. The conducting electrons are represented by e^-, while + represents ionized donors [68].

3.1.4 Nanoparticle aggregates

When ZnO nano-crystals are aggregated together and a voltage is applied, the effect of gas adsorption on the current that pass through the aggregate depends also on the energy barrier between nano-crystals in contact with each other [9] [10] [69]. Aggregate sensors are composed of multiple nano-particles that are connected to their neighbours by *necks*. On the surface of the nano-crystals, a *surface depletion layer* is created by adsorbed oxygen molecules, that trap conduction electrons and form O_2^- ions. The dependence of the overall conductivity of the aggregate on the concentration of surface adsorbed species depend on the relative dimensions of the particles *D* with respect to the surface depletion layer thickness *L* (see Fig. 39) [70].

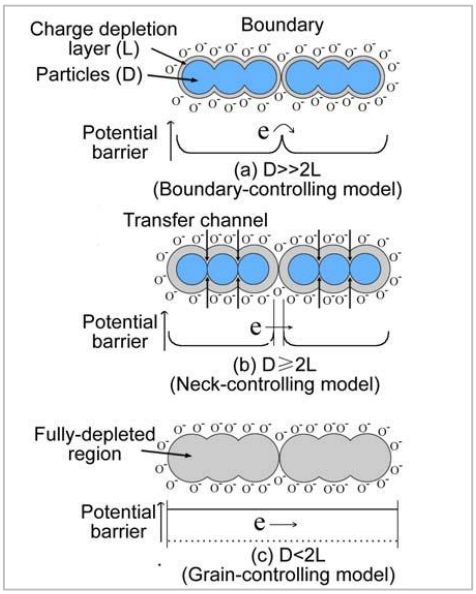

Fig. 39 Schematic model of the crystallite size on the sensitivity of metal-oxide nano-particle aggregates to gas adsorption. D is the nanoparticle diameter, while L is the surface depletion thickness [9].

Three different cases can be distinguished, according to the relationship between the particle diameter D and the depletion layer thickness L, produced around the surface of the crystallites due to chemisorbed ions. The size of L is on the order of a few nm for most metal oxides, including ZnO; the exact value depends on the concentration of surface species, which in turn depends on the species partial pressure in the surrounding atmosphere.

- When *D >> 2L*, the conductivity of the whole structure depends on the inner mobile charge carriers and the electrical conductivity depends exponentially on the intrinsic barrier height between particles. The current is not particularly sensitive to charges acquired from surface reactions.

- When *D ≥ 2L*, the space charge layer region around each neck forms a constricted conduction channel within each aggregate. Consequently, the conductivity not only depends on the particle boundaries intrinsic barriers, but also on the cross section area of those channels and so it is sensitive to reaction charges. Therefore, the particles are sensitive to the ambient gas composition.

- When *D < 2L*, the space-charge layer region dominates the whole particle and the crystallites are almost fully depleted of mobile charge carriers. The energy bands are nearly flat throughout the whole structure of the interconnected grains and there are no significant barriers for inter-crystallite charge transport, so the conductivity is controlled only by the inter-crystallite conductivity. Few charges acquired from surface reactions will cause large changes of conductivity of the whole structure, so that it becomes highly sensitive to ambient gas molecules when its particle size is small enough.

As most ZnO branched nano-structures have "branch" diameters of ≈100 nm and are a few µm long, aggregates of these nano-particles such as nano-tetrapod clusters will have the 2nd type of behaviour, having *D ≥ 2L*.

3.1.5 Photocurrent behaviour

The photocurrent behaviour of ZnO nano-crystals and nano-crystal aggregates show very unusual characteristics, that are a consequence of the gas adsorption-related conductivity. When light is shone on ZnO crystals that have adsorbed oxygen molecules in the form of O_2^- ions, electron-holes pairs are generated, and holes (h^+) that diffuse to the surface of the crystals neutralize O_2^- ions by the reaction:

$$O_2^-(ads) + h^+ \rightarrow O_2(g)$$

This release molecular oxygen to the atmosphere and reduces the width of the surface depletion layer, increasing the overall conductivity of the sample by widening the neutral conduction channel [71] [72] [73].

This mechanism can explain qualitatively many of the unusual features observed in the PC behaviour of ZnO and other metal oxides, such as:

- ZnO-based devices can have PC rise and decay times that can be *extremely long*, typically much longer than the characteristic carrier recombination times, and for some samples on the order of hours or days. The PC characteristic time are highly variable among different type of samples and nanostructures, as well as mong different experimental groups working on similar structures [28] [71] [73] [74] [75].

- Moreover, most samples show *persistent photocurrent* (*PPC*), that is the retaining of part of the photo-conduction properties for a long time after light is turned off [71] [74] [76] [72].

Addressing the problem of slow and persistent photoconductivity is a fundamental part of ZnO material research, in particular for nanostructures, where these effects are typically more important. Understanding the causes of this behaviour is necessary to control its effects on ZnO nano-structure-based photo -detectors, and this could lead to more reliable and faster response.

3.2 ZnO nano-tetrapods grown by vapour phase

ZnO nano-structures can be grown with a number of different techniques, such as chemical vapour deposition (CVD), thermal evaporation, pulsed laser deposition (PLD), electrochemical deposition and hydrothermal growth, among others [28] [77] [78] [79].

The samples described in this thesis are composed of ZnO *tetrapod nano-crystals*, which were obtained by a simple and cost-effective vapour phase growth technique, that is described briefly in the following section [31] [80].

3.2.1 Vapour-phase growth of ZnO nano-crystals

The vapour-solid growth described here is a method optimized for the production of ZnO nano-TPs in large quantities, i.e. tens of mg per run in small laboratory-scale reactor, a quantity that is much larger than in standard techniques. The technique is based on the thermal evaporation of metallic zinc and subsequent oxidation of Zn vapours in an oxygen flow; this method does not make use of any catalyst or precursor, in order to reduce as much as possible unintentional doping or contamination in the final nanostructures.

The growth of ZnO TP nanostructures is carried out in a tubular furnace composed of a quartz tube (see Fig. 40-a) fitted with two gas inlets carrying pure oxygen and argon gas inside the reactor separately; only one gas outlet is present.

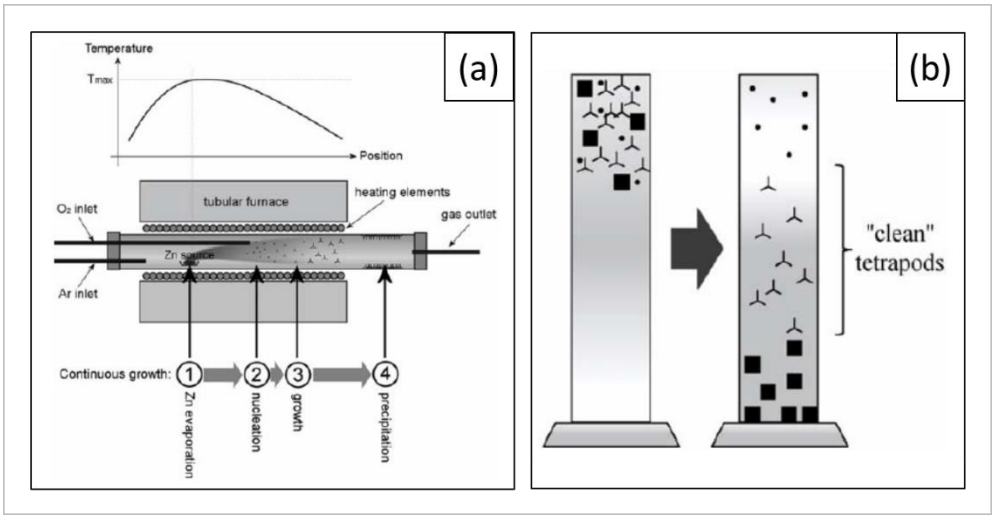

Fig. 40 (a) Schematic representation of the reactor setup for the vapour growth of ZnO nano-tetrapods; 4 different thermal zones are shown along with the temperature profile along the reactor. (b) Outline of the gravimetric separation of ZnO nano-tetrapods of a particular size from other nano-structures and impurities based on the different floating behaviour in an organic liquid suspension [80].

Thermal elements outside the reactor provide a thermal profile (also shown in Fig. 40-a) such that the *evaporation zone* of the source in the first part of the tube, is kept at a higher temperature (max. ≈700 °C) than the mid-section of the tube (*nucleation* and *growth zones*), where the maximum temperature does not exceed ≈600 °C. The mid-section of the reactor is characterized by negative temperature gradient.

The source material, consisting of 99.999% (5N) pure Zn powder, is located inside the evaporation zone within an alumina vessel. Because pure Zn melts at 420 °C, the charge in the evaporation zone (T=650-700°C) is completely melted, and gives rise to Zn vapours at pressures in the range of 37 - 82 mbar.

The vapours are then transported by the argon flow in the nucleation region, where the reaction with O_2 gas, injected in this region by the 2nd line, takes place. The products of this reaction are solid Zn nuclei in large quantities. Oxygen gas injection does not take place directly above the molten Zn charge, but in a downstream position along the chamber, in order to avoid the formation of an oxide layer on the surface Zn source that would prevent further evaporation, thus reducing the overall yield of the process.

During O_2 injection in the vapour phase of Ar gas and Zn vapours, the nucleation of ZnO crystal cores formation is observed as the formation of a characteristic white smoke that fills the final part of the reactor tube. These nuclei, suspended in the gas stream, move then to the lower temperature *growth zone*, meeting favourable supersaturation conditions that result in the branching out of the nuclei, which results in the growth of TP nanocrystals in very large concentrations. This growth process ends when the crystals reach the coldest region of the reactor and precipitate on the cold walls of the quartz

tube (*precipitation zone* in Fig. 40-a), where they can easily be collected in the form of a thick, fluffy film.

The three-dimensional symmetry of the tetrapod nano-crystals is a product of the fact that the growth happens completely in gas phase, without any constraint due to the chamber walls.

The described growth process is not self-inhibited as the standard one, being Zn source protected by oxidation, and can run continuously up to total consumption of source material. This is probably the biggest advantage of this technique, which results in very large growth yields.

After the growth and collection, the reaction products are placed in an isopropanol suspension, in which ZnO is insoluble, in order to decant and separate the TP nanocrystals from any other spurious structure. The separation is carried out by gravimetric effect, by which the different ZnO morphologies mixed with the tetrapods, are separated thanks to their different flotation properties (Fig. 40-b).

3.2.2 Nano-crystals structure

ZnO nano-tetrapods obtained in this way have leg diameters of ≈100 nm and length of ≈1 µm. Actual leg dimensions and aspect ratio depend on various growth conditions, such as temperature in the reaction zone and gas flow. X-ray powder diffraction analysis of ZnO nano-tetrapods show that the structures are well crystallized, and diffraction peak positions are consistent with an all-wurtzite structure, that is, only the hexagonal phase is present, despite the tetrahedral symmetry.

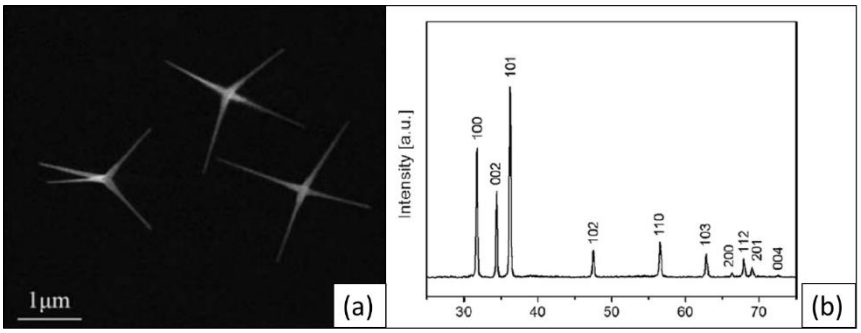

Fig. 41 (a) SEM image of ZnO nano-tetrapod crystals obtained by vapour-phase growth. (b) X-ray powder diffraction spectrum of the same crystals showing all-wurtzite crystal structure [31].

The tetrahedric shape can be explained by the *octa-twin nucleus model* [65]. According to this model, ZnO nuclei formed in an atmosphere containing oxygen are octa-twins nuclei which consist of eight tetrahedral-shape crystals, each consisting of three (1,1,-2,2) pyramidal facets and one (0,0,0,1) basal facet (Fig. 42-b). The eight tetrahedral crystals are connected together by making the pyramidal faces contact one with another to form an octahedron (Fig. 42-c). The surfaces of the octa-twin are all basal planes.

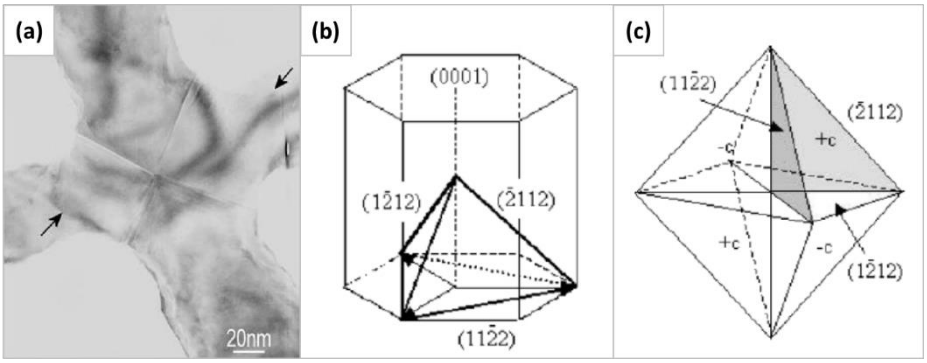

Fig. 42 (a) TEM image of a ZnO tetrapod nano-crystal showing the twin planes in the nucleus. (b) A pyramid formed by three (1,1,-2,2) and one (0,0,0,1) facets. (c) The octa-twin model composed of eight pyramidal inversion twin crystals [65].

3.3 ZnO nano-tetrapod samples

Two types of samples were studied in this thesis: multiple and single ZnO nano-tetrapod-based devices, the characteristics of which were analysed separately and then compared with each other to understand the electric and photo-conductive behaviour of nano-tetrapod aggregates under different conditions.

In particular the devices studied are the following:

1) A device constituted by *multiple ZnO nano-tetrapods* (MTP), deposited as a film on an Al_2O_3 substrate between two Au electrodes. The deposition was made by precipitating an isopropanol suspension of tetrapods on the substrate using a mask. These samples were also used as gas sensing devices in dark conditions as described in previous works [31], and are thus equipped with a Pt resistor to attain a working temperature of ≈400°C. An image of a MTP sample and its schematic outline are showed in Fig. 43-a and Fig. 43-b respectively.

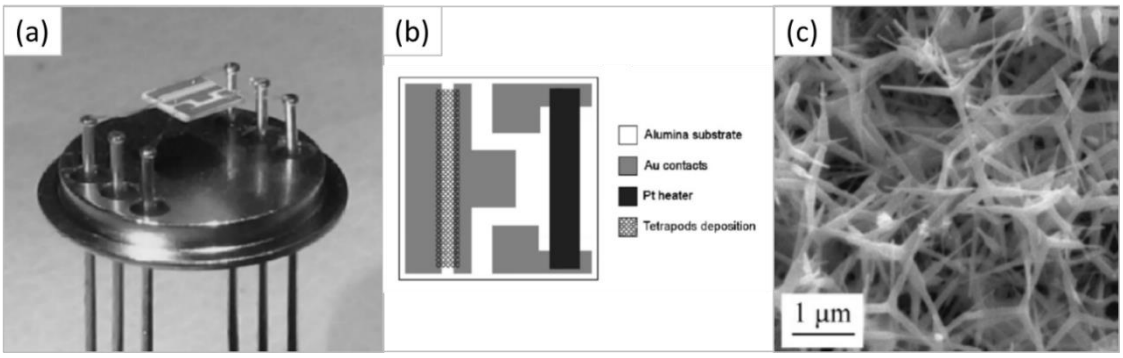

Fig. 43 (a) Picture of a ZnO multiple nano-tetrapod (MTP) sample. The substrate is suspended over the TO base with gold leads to provide thermal insulation. (b) Schematic diagram of the Al_2O_3 substrate over which the nano-tetrapod film is deposited, along with Au electrodes and Pt resistor. (c) SEM image of the film showing the densely packed structure of the nano-tetrapods.

2) A *single ZnO nano-tetrapod* (STP), deposited between comb-like Au electrodes (electrode distance = 2 µm) on a semi-insulating Si substrate (Fig. 44-b). These type of samples were obtained by precipitating a highly diluted $(CH_3)_2CHOH$ suspension of ZnO nano-crystals on the substrate. Electric contact between gold electrodes and the nano-tetrapod "legs" was obtained using focused ion beam (FIB) technology (Fig. 44-c).

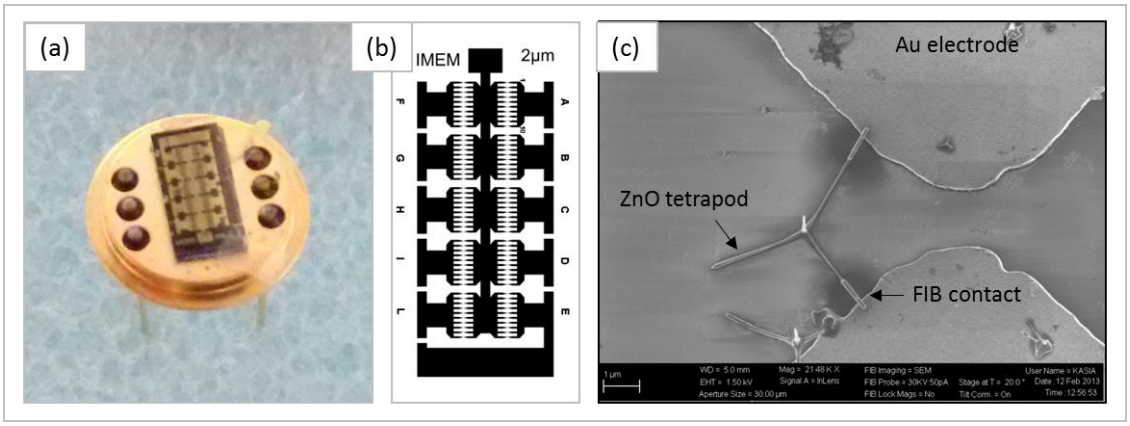

Fig. 44 (a) Picture of a ZnO single nano-tetrapod (STP) sample. (b) Diagram of the semi-insulating Si substrate with comb-like Au contacts at a distance of 2 µm from one another. (c) SEM micrograph of a single nano-tetrapod between two Au electrodes with FIB depositions providing the electric contact between the tetrapod "legs" and the triangular-shaped electrodes.

In the following sections, the characterization of these two type of samples is described, and the results are compared to analyse the difference in the behaviour of nano-crystals in single and aggregated form.

Samples of ZnO nano-tetrapods were characterized by optical techniques, such as photo-luminescence spectroscopy and powder reflectance spectroscopy, to determine the value of the optical band gap of the material, as well as the eventual defects present.

Moreover, electric behaviour of the samples was determined, along with the temporal evolution of the photocurrent response, and the spectral PC analysis. The main objective of the electro-optical characterization was that of trying to resolve aspects of the unusual PC response of ZnO nano-structures that are not clear and in some aspects different from the expected behaviour described in the relevant literature.

3.4 Photoluminescence spectroscopy

Photoluminescence (PL) characterization of ZnO nano-tetrapod aggregates (*MTP samples*) was done to investigate the material properties of the nano-structures.

PL spectroscopy, as a technique, is very similar to *cathodoluminescence*, described in Par. 2.6, the main difference is the excitation method. The sample is illuminated with a laser source having photon energy $h\nu > E_g$ (E_g is the energy gap of the material); in this way, free carriers (e^-- h^+ *couples*) are generated in the semiconductor through band-to-band transitions. Excited carriers lose then energy by thermalization to the CB and VB extrema, from which can then *recombine radiatively* with carriers of the opposite type emitting a photon of energy hν. The energy of the photon is equal to the energy difference between the levels E_1 and E_2 involved in the radiative recombination process, i.e.:

$$h\nu = \frac{hc}{\lambda} = E_2 - E_1 \qquad (10)$$

Thus the *PL spectrum* $I_{PL}(\lambda)$, i.e. the intensity of emitted light as a function of photon energy hν or wavelength λ, gives information about the band gap E_g, as well as eventual energy levels inside the gap.

The technique is most efficient for direct band gap semiconductors like ZnO, as the probability of radiative band-to-band transitions is typically much higher than in the case of indirect semiconductors.

3.4.1 PL spectrum of ZnO nano-tetrapods

PL spectra of aggregate ZnO nano-tetrapod samples were acquired at room temperature using UV laser excitation. The spectra relative at 3 different samples are reported in Fig. 45.

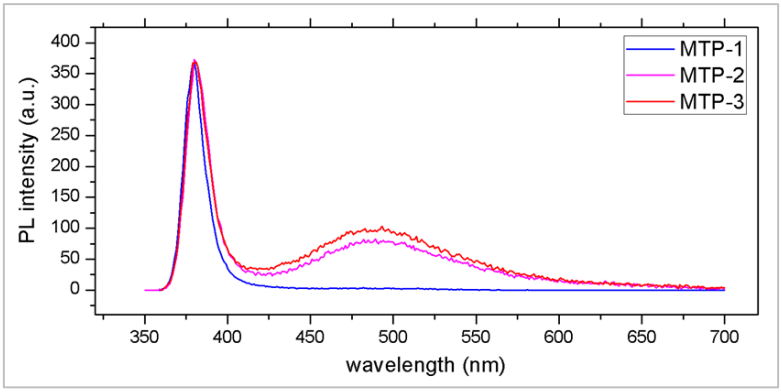

Fig. 45 Photoluminescence intensity (in arbitrary units) as a function of the wavelength of emitted light, measured for 3 different samples of ZnO nano-tetrapods. The PL intensities are normalized at the intensity of the band edge emission.

PL spectra of ZnO tetrapods grown form vapour typically show two emission lines, the one at λ≈380 nm is the *near band edge* (NBE) *emission* due to the direct conduction to valence band recombination, while the other (at λ≈490 nm) is a *defect emission*, that is well known in literature as the *green band* (GB), that corresponds to defect-related levels inside the band gap [81] [82].

From the three normalized spectra it is possible to observe that the visible peak positions in all three samples are exactly the same, pointing to a highly reproducible growth technique that results in consistent material properties over different growth runs. However, it is evident that the relative intensity of the band edge and defect peaks can vary widely for different samples, as the defect line can even almost disappear in some cases (MTP-1 sample in Fig. 45).

As the narrow band at λ≈380 nm is due to radiative recombination of excitons across the energy gap of ZnO, while the broad peak centered about λ≈490 nm is defect-related, the ratio of the (integrated) intensity of the two can give an information on the quality of the nano-crystals. In general, better nano-tetrapod crystals show an intense near band edge emission, with a very small or zero defect line intensity, and vice-versa.

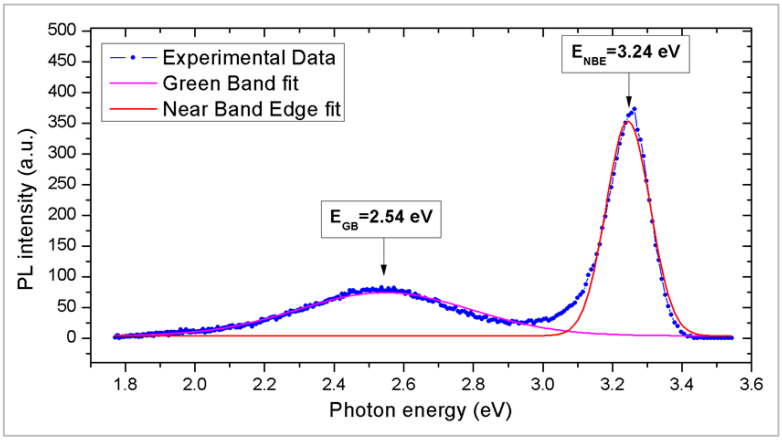

Fig. 46 PL intensity as a function of photon energy for a ZnO nano-tetrapod sample. Experimental data was fitted with two Gaussian functions to resolve the positions of the two peaks.

To determine the exact positions (*barycentres*) of the two PL bands, the spectral data was fitted using two Gaussian curves (Fig. 46). The fitting parameters, showed in Table 5, are consistent with what can be found in literature for the energy of the near band-edge in ZnO nano-tetrapods and the defect emission called green band, that is characteristic of ZnO crystals and nano-structures [81] [82].

	$h\nu_0$ (eV)	$\delta h\nu_0$ (eV)	w_{FWHM} (eV)	δw_{FWHM} (eV)
NBE	3.245	0.001	0.127	0.001
GB	2.544	0.004	0.50	0.01

Table 5 Parameters relative to the two PL bands in Fig. 46, obtained by Gaussian fitting of the experimental PL spectral data. NBE and GB represent the near band-edge and green band respectively, while $h\nu_0$ is the peak's barycentre and w_{FWHM} is the width at half maximum of the corresponding band (in eV). The δ- prefix denotes the fitting errors.

The near band edge energy obtained from PL data of $h\nu_{NBE}$=3.24 eV is considerably inferior than the know band gap value for ZnO of about 3.37 [16]. This due in part to the high exciton binding energy of ZnO (≈60 meV), but also to the spectral shift caused by native surface defects; in fact, the shift was observed to vary depending on the dimensions and type of nano-structures, due to the different surface-to-volume ratio

[81]. Quantum effects in ZnO nanostructures of this size (diameter of about 100 nm) can be ruled out, as the Bohr radius for ZnO is 2.34 nm [81].

Green emission is often attributed to singly ionized oxygen vacancies [83] [84], although this assignment is highly controversial. Other hypotheses include antisites oxygen [85], which was proposed on the basis of band structure calculations [86]. Green emission was also attributed to oxygen vacancies and zinc interstitials [87], as well as Cu impurities [88].

While the type of defect responsible for the green emission has not yet been conclusively identified, it probably derives from intrinsic types of defects, and there is convincing evidence that it is located at the surface. It was shown that coating ZnO nanostructures with a surfactant suppressed green emission, whereas nanostructures of different dimension and shape show variation in the green band intensity, due to the variation in surface-to-volume ratio [82].

3.5 Diffuse reflectance spectroscopy

The ZnO nano-tetrapods in loose form have the appearance of a white powder that strongly scatter light. The method of choice of optical characterization with this type of material is by using the *diffuse reflectance spectroscopy* technique.

Diffuse reflectance spectroscopy is the measurement of the intensity scattered from the sample in the UV-VIS-NIR range. The spectrum was acquired with a *Varian 2390 double-beam spectrophotometer*, used also for the transmission spectra described in Par. 2.5. In order to acquire detect the intensity of light scattered in every direction by the sample, the instrument was fitted with a BaO-coated *integrating sphere*. The diffuse reflectance spectrum between 200 and 800 nm of a sample of ZnO nano-tetrapods powder is reported in Fig. 47.

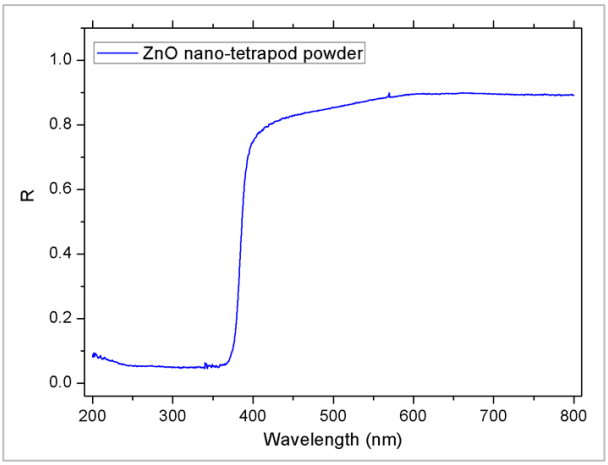

Fig. 47 Diffuse reflectance spectrum of a sample of ZnO nano-tetrapod powder. $R=I_R(\lambda)/I_0$ is the diffuse reflectance, i.e. the ratio between the reflected and incident intensity of light.

The spectrum is expressed as the ratio between the light intensity scattered from the sample I_R and the incident intensity I_0 as a function of light wavelength λ; the quantity $R=I_R(\lambda)/I_0$ is called *reflectivity*. In general, as materials tend to reflect more light in the region where they are transparent and be opaque for light wavelength that are absorbed, the diffuse reflectivity spectrum has an edge in a region as the transmission spectrum, that is for $h\nu=hc/\lambda\approx E_g$. From Fig. 47 it is clear the reflectivity of the sample rises sharply at about 390 nm, that is close to the band gap of ZnO.

However, to obtain a more precise determination of the optical band gap of the sample, the *Kubelka-Munk theory* can be used [89]. The K-M theory allows to extract, from the diffuse reflectance spectrum *R(λ)* of a *powder sample*, a quantity *f(R)* that is *proportional to the absorption coefficient α(λ)* [90]:

$$f(R) = \frac{(1-R)^2}{2R} \propto \alpha(\lambda) \qquad (11)$$

This relation is verified only for thick powder layers that scatter or absorb all incident light (no transmitted intensity).

As f(R) and α(λ) are proportional, the *Tauc plot* can be used as in Par. 2.5 to deduce the optical band gap; as ZnO is a direct band gap semiconductor, substituting f(R) for α in Eq. (6), one obtains [91]:

$$[h\nu \cdot f(R)]^2 = A(h\nu - E_g) \qquad (12)$$

Where $h\nu=hc/\lambda$ is the photon energy, *A* is a constant and E_g is the optical band gap. From this equation, the value of the optical band gap can be easily deduced by fitting linearly the *absorption edge* of the curve.

Fig. 48-a show the spectrum f(R) as a function of photon energy hν, obtained using the Kubelka-Munk relations. It is easily observed how the absorption coefficient rises sharply when the photon energy approaches 3.3 eV, even in logarithmic scale, indicating intense absorption of light in the near-UV range. Additionally, there is a low but measurable absorption at $h\nu<E_g$, that starts at about 2 eV; this effect is due to a broad distribution of intrinsic defects, such as oxygen or Zn vacancies in the material [92].

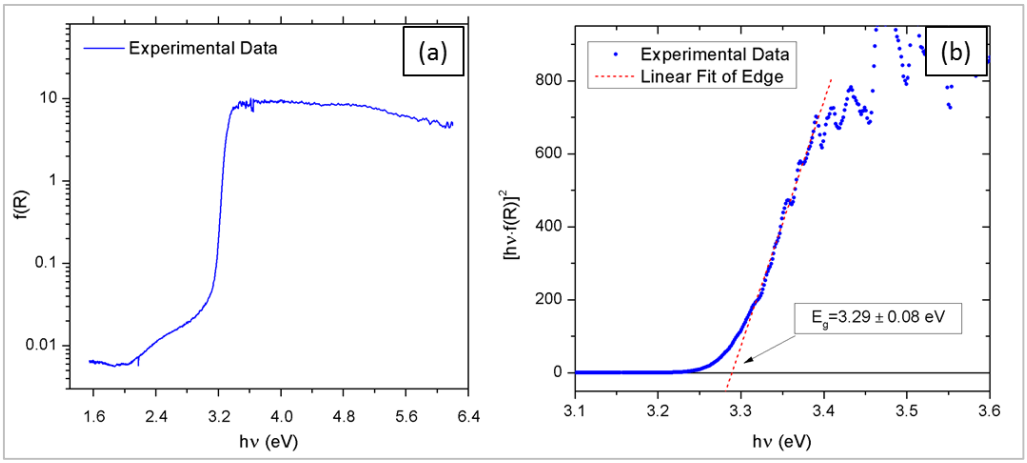

Fig. 48 (a) The quantity f(R), proportional to the absorption coefficient α, as a function of the photon energy hν. (b) Tauc plot of f(R) used to deduce the optical band gap of the material.

The linear fit of the Tauc plot is showed in Fig. 48-b, along with the result obtained for the optical band gap of the sample of ZnO nano-tetrapods. The obtained value is E_g=3.29 ± 0.08 eV, that is remarkably close to values that can be obtained from literature on ZnO nanostructures [2] [16] [81], thereby validating the method as well as verifying that the band gap of vapour-grown ZnO nano-tetrapods do not differ from that of single crystal ZnO.

3.6 Electrical characterization of multiple and single nano-tetrapod devices

Characterization of the current-voltage characteristic of multiple and single nano-tetrapod samples was made in order to determine the conduction properties of the different types of devices in the dark and under light. Measurements were made with a *Keithley 2400 source-meter* with sensitivity of 10 pA, and the voltage range of the measurements was determined beforehand so as to not damage the samples, in particular the single nano-tetrapod device, that is particularly delicate due to the small dimensions. To illuminate the sample a 300 W Xe-filled arc lamp was used, along with a Cornerstone grating monochromator.

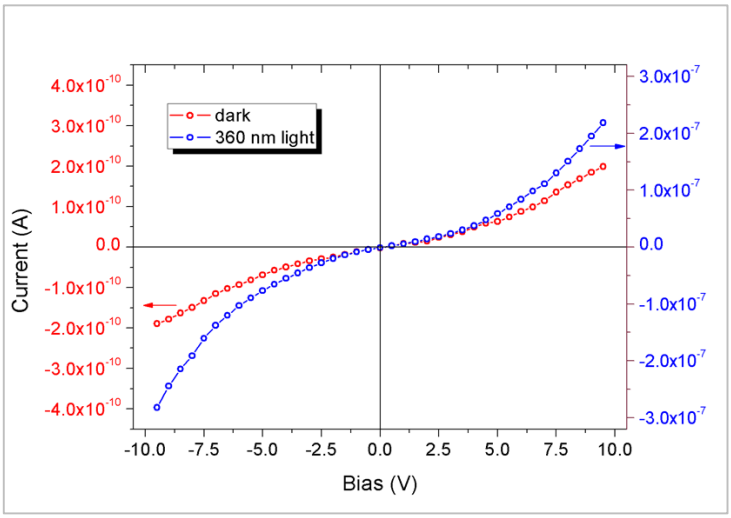

Fig. 49 Current-voltage characteristic at room temperature of a multiple (aggregated) nano-tetrapod sample in the dark and under UV light at 360 nm (intensity ≈1.2 μW·cm^{-2}).

The dark IV characteristic of aggregated nano-tetrapods (MTP sample) between Au electrodes (Fig. 49) is clearly non-linear in the (-10 V, +10 V) interval. Moreover, at room temperature the dark current is very small, being of a few hundreds of pA at 10 V. When the sample is illuminated with UV light of energy $h\nu > E_g$ (λ=360 nm), with an intensity of about 1.2 μW·cm^{-2}, the current increases strongly, while the IV characteristics remains strongly non-linear in the high bias region (over 1.5 V and below -1.5 V).

To quantify the change in conductivity of the sample, the resistance of the device in the approximately linear region at small bias (between -1.5 V and +1.5 V) was computed:

	R (Ω)	δR (Ω)	$\Delta G/G_0$
Dark	$9.85 \cdot 10^{10}$	$6 \cdot 10^{8}$	-
360nm light	$1.17 \cdot 10^{8}$	$5 \cdot 10^{6}$	842

Table 6 Resistance value R at low bias in dark and under 360 nm light for a MTP sample at room temperature, with error δR. The quantity ΔG/G0 represent the relative increase in conductance of the sample when it is illuminated.

The strong increase in the current when illuminated is due to a nearly 1000 times increase of the conductance G of the sample.

The non-linearity of the IV curve is a strong indication of the Schottky behaviour of the device as a whole: to better understand the origin of this behaviour similar IV measurements were made on a single ZnO nano-tetrapod-based device (STP sample).

The current-voltage characteristics of a STP sample, measured between -0.8 and +0.8 V in the dark and under illumination, are reported in Fig. 50. The small voltage range was chosen due to the small scale of the single tetrapod sample, which has limited ability to dissipate heat induced by the passage of current.

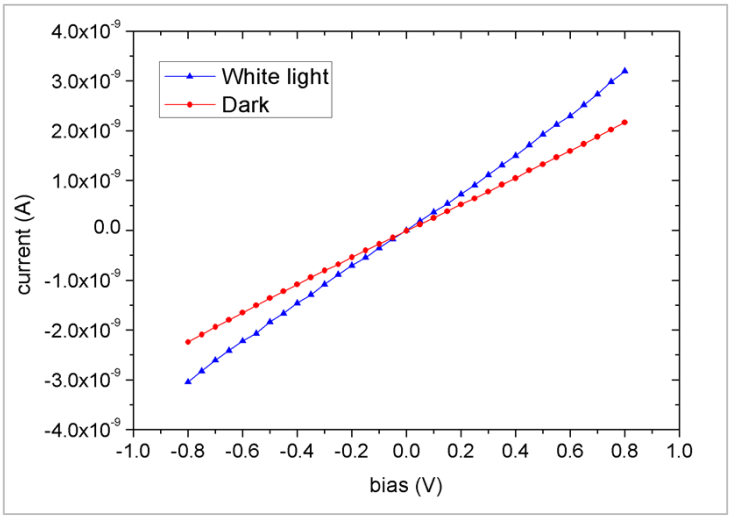

Fig. 50 Current-voltage characteristic at room temperature of a single nano-tetrapod-based sample (STP) in the dark and illuminated by a white light source with integrated intensity $I_0 \approx 1.6\ mW \cdot cm^{-2}$.

The IV under illumination was measured using full power (of intensity $I_0 \approx 1.6\ mW \cdot cm^{-2}$) white light, instead of monochromatic UV light as before. This was found to be necessary, because of the remarkably low sensitivity to light of the STP sample, for which response to monochromatic is too low to be measured reliably, even at or above the band gap. However, as we have already observed in Par. 3.5, absorption of light of $h\nu < E_g$ is negligibly small with respect to that above gap, so the photo-response of ZnO nano-tetrapods to white light can be safely considered a response to UV light at $h\nu \geq E_g$.

In contrast with the MTP sample, the IV characteristic was found to be remarkably linear in the whole range of measurement, in the dark as under illumination. The ohmic behaviour of the single nano-tetrapod sample can be attributed to ohmic contacts with the Au electrodes. As a consequence, the Schottky behaviour of the MTP samples is probably caused not by the contacts with the metal electrodes, but instead by the *inter-particle barriers* that charge carriers have to traverse. These barriers are formed by the contact between nano-tetrapod wurtzite legs, so are constituted mainly by the band bending at the surface of the crystals. It is worth noting that, due to the much smaller dimensions, the mean electric field inside the STP sample is ≈500 times higher than that

in the MTP device, at the same voltage; that is, the electric field inside the MTP sample at 50 V has the same order of magnitude that the field inside the STP sample at 0.1 V.

As can be observed in Table 7, the dark value of the resistance of the STP sample is almost 2 order of magnitude less than that of the MTP; indicating a higher value of the dark current of the device; this is probably due to the absence of the Schottky barriers in the STP. Moreover, the relative increase in conductance $\Delta G/G_0$ when the STP sample is illuminated is modest in comparison with that of the MTP, even if the light intensity is $\approx 10^3$ times higher; that is, the single tetrapod device has low photosensitivity.

	R (Ω)	δR (Ω)	$\Delta G/G_0$
Dark	$3.68 \cdot 10^9$	$1 \cdot 10^6$	-
360nm light	$2.63 \cdot 10^8$	$1 \cdot 10^6$	0.401

Table 7 Resistance value R in the dark and under illumination with white light for a STP sample at room temperature (δR is the corresponding error). The relative increase in the conductance of the sample is indicated as $\Delta G/G_0$.

The increase in photo-detecting capabilities of aggregated nano-crystal was also reported in literature [28] [93], and is probably caused by the presence of an electric field at the junction between nano-crystals that reduces the recombination rate of carriers, increasing the photocurrent.

3.7 Photocurrent analysis

We have already introduced in Par. 3.1.5 that ZnO, in particular when in the form of nanostructures, has peculiar photocurrent (PC) behaviour. The most important aspects are the long time scale of PC variation under constant illumination, and the presence of persistent photo-current (PPC) after removing the illumination.

In samples composed of aggregated nano-tetrapod crystal that are described in this work, these peculiar PC and PPC effects are particularly important, as will be shown in the next section.

3.7.1 Temporal dependence of the photocurrent

PC response of MTP and STP samples as a function of time were acquired by illuminating the samples and recording the variation of the current as a function of time. As ZnO nano-structures with high surface to volume area like ZnO nano-tetrapods aggregates are highly sensitive to surface adsorbed oxygen, PC measurements in air (oxygen partial pressure p_{O2}=210 mbar) were confronted with others acquired in a controlled

atmosphere or in vacuum, in order to determine the effect of the atmosphere of the PC of ZnO multiple and single nano-tetrapod crystals.

The PC vs. time measurement reported in Fig. 51 was acquired at atmospheric pressure in air (21% oxygen concentration) illuminating the sample with above gap UV light (λ=370 nm). The entire measurement is longer 24 hours.

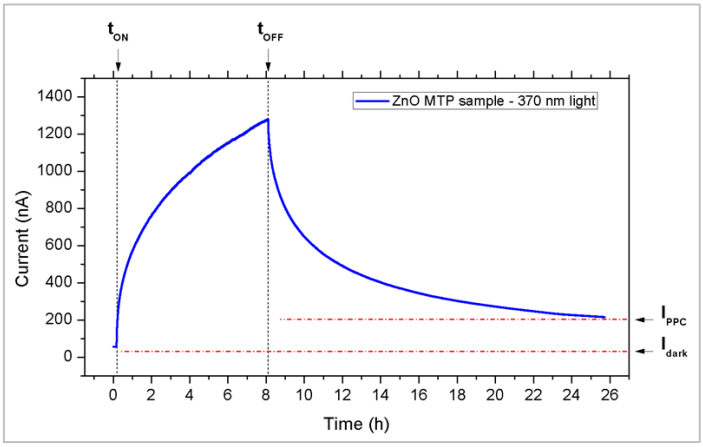

Fig. 51 Photocurrent of a MTP sample at 5 V bias in air as a function of time. The sample was illuminated in the time interval between t_{ON} and t_{OFF} with light of 370 nm ($h\nu=3.35$ eV>E_g). I_{dark} is the dark current while I_{PPC} is the persistent PC value.

The slowness of the process is evident from the fact that even after about 8 hours of constant illumination, the PC has not yet reached the saturation value, i.e. the sample is not in equilibrium. After light is turned off, the current does not return to the dark value even after waiting for 2 times the illumination time, so there remains a persistent photocurrent that is about 10% of the maximum attained value.

As explained in Par. 3.1.5, this effect is due mainly to photo-desorption of adsorbed oxygen from the surface of the ZnO nano-tetrapods. The PC increase is not caused directly by carrier photo-generation inside the material, whose contribution is small and can safely be neglected [73], but by reduction of the surface-related depletion layer. The characteristic time of this process is much longer than the carrier recombination time in ZnO (τ≈1 ns), depending on photochemical processes.

3.7.2 PC dependence on atmospheric composition

As the photocurrent process depends on surface adsorption and desorption of species, it is important to study the dependence of the time-resolved PC on the oxygen concentration in the atmosphere.

The PC as a function of time for a ZnO MTP sample was measured at 5V, under illumination with low intensity multi-wavelength light and at different values of the air pressure in the chamber containing the sample under investigation. The results are reported in Fig. 52. As the persistent photocurrent effect is always present, the value of the starting "dark" current value for one measure is influenced from the PPC of the preceding one; to eliminate this effect, all the curves were shifted so as to set the initial dark current value to zero.

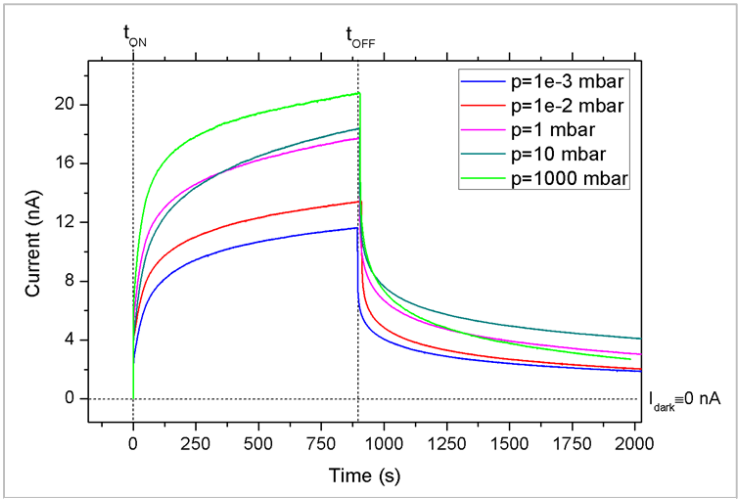

Fig. 52 Photocurrent of MTP sample as a function of time measured for different external air pressures. The sample was illuminated with white light between the instants t_{ON}=0 and t_{OFF} (Δt=900 s). The Dark current value I_{dark} was set to zero nA to compensate for the persistent photo-current effect.

The most evident effect is the general tendency of the PC to increase when the pressure is increased, i.e. after a set amount of time (900 s), the PC increase ΔI_{PC} of the MTP device in air is about 2 times the increase in vacuum. This effect is interesting because it is the exact opposite of the behaviour that is typically observed in literature for ZnO single crystals, thin films [94] and other nano-structures, such as isolated nano-wires [71] [73]; in those instances, when the sample is exposed to a vacuum, the PC tend to increase with respect to the value in air, where the O_2 concentration is higher [74]. The shape of the PC vs. time curve does not depend strongly on the external atmosphere, indicating that the underlying process is likely the same in all conditions.

As a means of comparison, measurements of PC vs. time were also made for the STP sample (bias 1 V), using white light in air and vacuum conditions: the results are reported in Fig. 53.

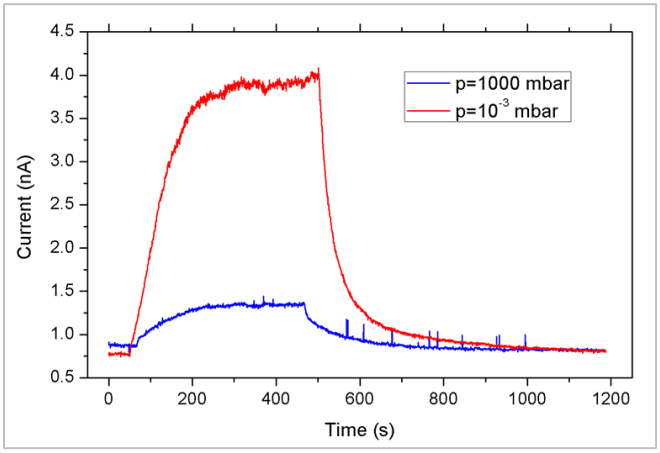

Fig. 53 Temporal evolution of the PC of a STP sample at 1 V bias under white light. The measurement was made at room temperature in air (atmospheric pressure) and in vacuum conditions (p=10^{-3} mbar).

The general photoconductive behaviour of the single tetrapod is quite differently from the aggregated tetrapods in the MTP sample, as evidenced from the relatively short rise time of the PC when the STP is illuminated with white light: the PC reaches a saturation value in less than 200 s. Moreover, when light is turned off, the current returns to the dark value in approximately the same amount of time, and there is no measurable persistent photocurrent effect.

In addition, the maximum value reached by the PC has an inverse dependence on the external air pressure, i.e. the photocurrent increase ΔI_{PC} in vacuum is more than 6 times larger than that in air, while the dark current does not vary appreciably.

As stated earlier, this inverse relationship on the O_2 concentration in the atmosphere is in line with observations made by other research groups on ZnO nanostructures, in particular single nanowires [71] [73] and nano-tetrapod [95] samples.

Summarizing the data in Fig. 52 and Fig. 53, it is evident that:

- The *single nano-tetrapod* (STP) sample, when illuminated show relatively fast PC rise and decay, reaching an equilibrium value after about 200 s. The PC rise in vacuum is several times higher than that in air, where the oxygen partial pressure is higher. This behaviour is consistent with that of ZnO single crystals and isolated nanostructures.
- In contrast, *multiple nano-tetrapod* (MTP) devices have very slow PC rise and decay, which do not show saturation of the photocurrent even after several

hours of constant illumination. In addition, there is a strong PPC effect, which persist for days before returning to the dark current value. Finally, the PC rise after a set amount of time increase with increasing external air pressure, in contrast with the STP sample behaviour and with literature data.

The STP sample behaviour can be thus explained by the standard surface-desorption mechanism that is typically used to explain the photoconduction of isolated ZnO nano-wires [71] [73]. When the sample is illuminated with UV light, desorption of oxygen cause reduction of the surface depletion layer thickness, increasing the width of a *neutral channel* inside the "legs" of the sample, which increase the conductance (see Fig. 54). This mechanism can be called *channel conduction*, and is more efficient when the oxygen concentration in the atmosphere is lower, because there is less re-adsorption of O_2, which results in a higher photocurrent at the equilibrium.

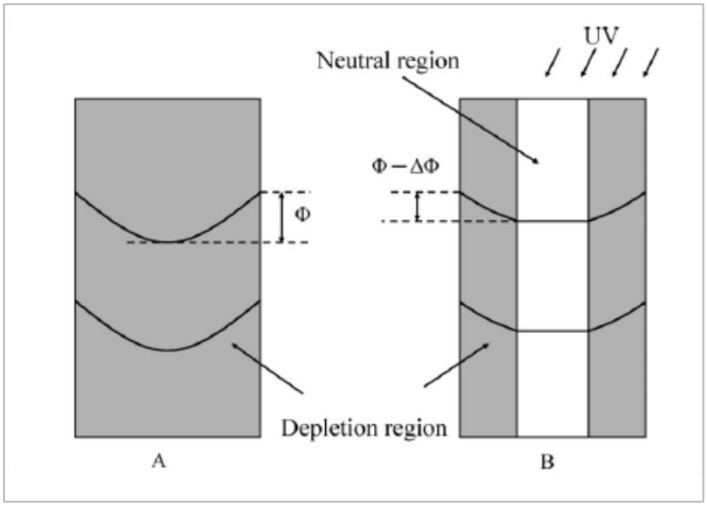

Fig. 54 Channel conduction mechanism for a ZnO nano-wire illuminate by UV light. (a) Dark conditions, in which the wire is almost fully depleted due to O_2 adsorbed on the surface. (b) Illumination with UV light desorbs oxygen and widen the conduction channel, thereby increasing the conductance of the nano-wire [73].

However, as the MTP sample has a remarkably different photoconduction behaviour, a different mechanism is necessary to explain the experimental observations. Determining why aggregated nano-tetrapods behave so differently to single tetrapods and other forms of ZnO is also important for future technological applications of these nano-structures.

3.7.3 Photocurrent spectroscopy of MTP devices

Spectroscopic analysis of the photo-response, i.e. the measurement of the PC response of the sample at different photon energies, was used as a characterization technique for the multiple nano-tetrapod samples. Unfortunately, a spectroscopic analysis of the STP samples was not possible, due to the low responsivity of these devices that rendered the photocurrent undetectable for mono-chromatic light.

Due to the very long rise/decay times involved, it proved difficult to measure the PC spectrum of the sample. As we have already pointed out, ZnO MTP show high PC sensitivity to UV light, but the response time tend to be very slow, ad is next to impossible to wait for the PC to saturate properly. This fact is obviously problematic when one tries to measure the PC response as a function of the wavelength of incident light in a standard way, with the aid of a lock-in amplifier and a light chopper running at frequencies of the order of hundreds of Hz. As the response time of the samples is much longer than several ms (on the order of several minutes to several hours), the sample has not enough time to vary appreciably in any light/dark cycle, and the net effect is that the amplifier cannot measure almost anything.

To overcome this problem, and to be able to measure the PC response of the sample with increased accuracy and sensitivity, we came out with a simple method whereas the PC is acquired at every wavelength after a pre-set amount of illumination time ($\Delta t = t_{OFF} - t_{ON} \approx$ 300-1000 s, depending on the sample), then the value of the current at $t=t_{ON}$ is subtracted to this value. In this way, we measure only the photocurrent increase ΔI_{PC} for every wavelength, compensating for the eventual persistent photocurrent that may be left from previous measurements.

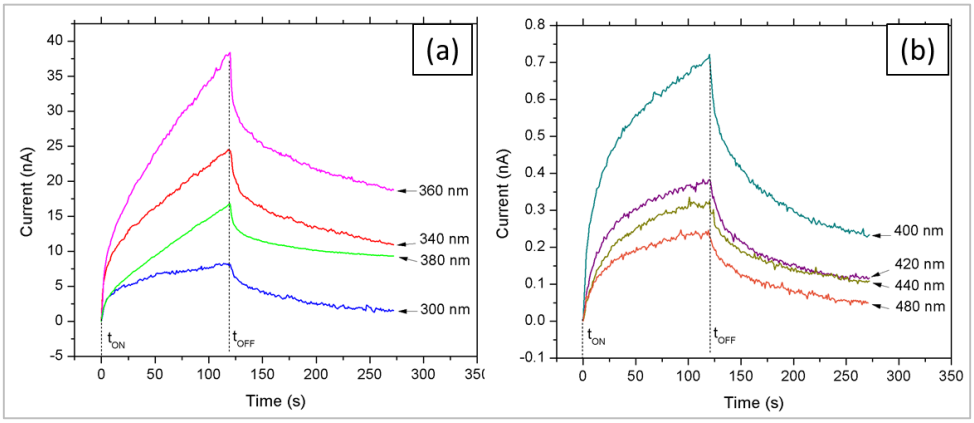

Fig. 55 Photocurrent vs. time at 5 V for a ZnO MTP sample in standard conditions under illumination with (a) above gap and (b) below gap mono-chromatic light. The initial current at $t=t_{ON}$ was set to zero to eliminate the PPC effect.

Measuring the PC increase after a relatively long amount of time has the added benefit of increased sensitivity to photocurrent variations, in particular to below gap light. In Fig. 55 are reported examples of the PC vs. time measurements for a MTP sample at 5 V bias under illumination with mono-chromatic light of different wavelengths, corresponding to photon energies above and below the band gap.

The PC spectrum of a MPT samples was measured in *air* (atmospheric pressure) and in *vacuum* ($p \approx 10^{-3}$ mbar) conditions, at room temperature under 5 V bias. Both spectra are reported in Fig. 56.

The PC response in air is *≈10 times higher* than that in vacuum, consistently with PC vs. time observations described in the preceding chapter, but in direct contradiction with the observed behaviour of single nano-tetrapod samples and literature data.

Remarkably, however, the ratio between the PC in air and vacuum remains approximately constant for every value of the energy hv, so that the overall dependence on the photon energy is the same in both cases. This observation is important because it indicates that we are observing the actual material properties of the ZnO nano-tetrapods, thus validating the method used to measure the spectra.

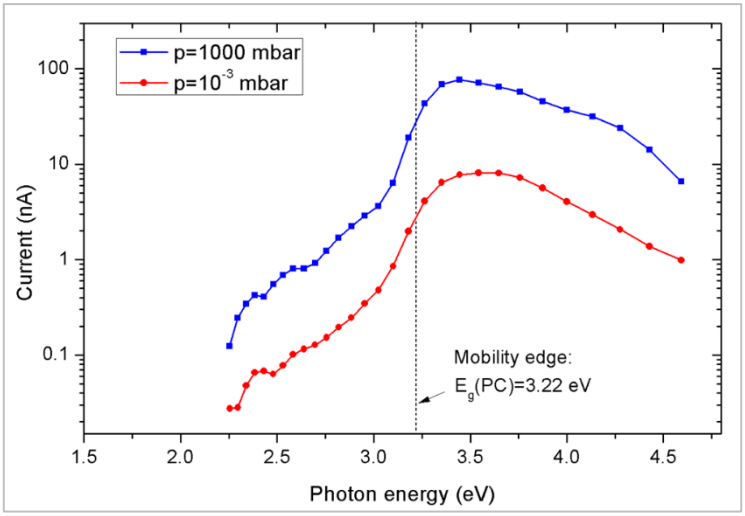

Fig. 56 Photocurrent response of a MTP sample as a function of photon energy hv at 5 V bias. The spectra were measured at room temperature in air (blue) and vacuum (red) conditions in the range 2.25<hv<5eV (corresponding to wavelengths between 550 and 250nm). E_g(PC)=3.2 eV is the value of the mobility edge obtained from the PC spectra, defined as the median hv value of the PC edge.

From the spectral data in Fig. 56 it is clear that there is non-negligible photo-response at energies below the optical band gap of the sample (E_g≈3.3 eV), that form a broad, continuous defect-related band from 2.25 eV to 3.1 eV. This is consistent with optical absorption data obtained from diffuse reflectance spectroscopy, as described in Par. 3.5, and is a common feature of most metal-oxide semiconductors. Below gap photocurrent in probably related to excitation of electrons from the VB to levels inside the energy gap, leaving a corresponding number of holes in the valence band: free holes generated in this way can then diffuse to the surface and recombine with adsorbed oxygen ions, increasing the photocurrent. Gaussian peak fitting of the below gap PC data gave 2 energy level bands centered around 2.5 and 3 eV; assuming that the transitions corresponding to these energies are due to excitation of electrons from the VB to the defect levels, these are respectively 0.9 and 0.3 eV below the CB minimum (see Fig. 56).

Common intrinsic defects in ZnO are attributed oxygen or zinc vacancies, as these are the most common native defects in metal-oxides like ZnO [16] [67] [81]; high concentration of defects or structural disorder can result in energy levels that have a continuous or almost-continuous energy distribution, so that electronic transitions to these levels appear as broad bands in the PC or absorption spectra.

At photon energies from about 3.1 to 3.5 eV there is a sharp PC rise attributed to band-to band transitions. The mobility edge value obtained from the PC spectra for ZnO MTP samples is E_g(PC)=3.22 eV (corresponding to λ_{BE}≈380 nm). The value of the mobility edge is close to the exciton line of the PL spectrum of 3.24 eV, indicating that holes forming excitons do contribute to the PC by surface recombination with electrons trapped by adsorbed O_2^- ions.

The maximum PC increase is observed at hν=3.44 eV, corresponding to λ=360 nm. For wavelength shorter than 360 nm the sensitivity decreases steadily; this effect is caused by the shorter absorption depth of light with energy hν>>E_g that decreases the interaction volume inside the sample, thereby reducing the total number of e^--h^+ couples generated inside the material.

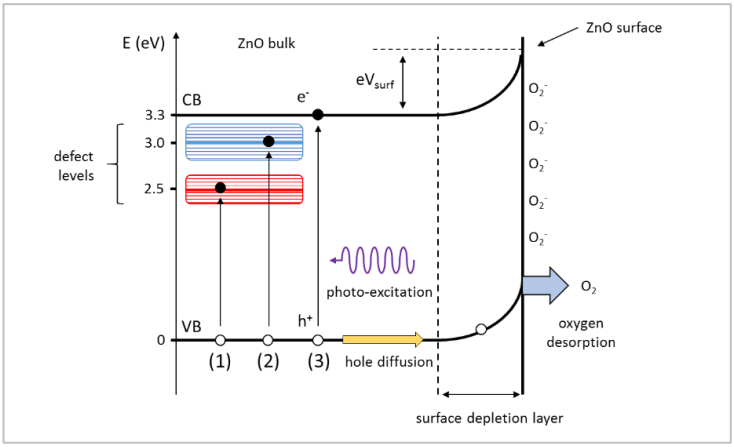

Fig. 57 Schematic diagram of the electron transitions that can give rise to the measured increase in photoconductivity. (1) and (2) correspond to electron transitions from the VB to a defect level inside the band gap, while (3) is a band-to-band transition.

3.8 Temperature dependence of the conductivity

To understand why the aggregated nano-tetrapods have different behaviour than isolated, but otherwise identical, single tetrapods, we analysed the temperature dependence of the conductivity of the MTP device.

Measurements on various samples were made in a controlled inert atmosphere composed of dry N_2 gas in a climatic chamber; the gas is fluxed continuously inside the chamber, and has the additional task of transferring heat from the chamber walls to the sample, in a homogeneous way.

The current-voltage characteristic of the sample under investigation was acquired with the Keithley source-meter in the dark at various temperatures, between RT (298 K) and 573 K. The IV characteristics of a MTP sample for a few value of the chamber temperature are reported in Fig. 58.

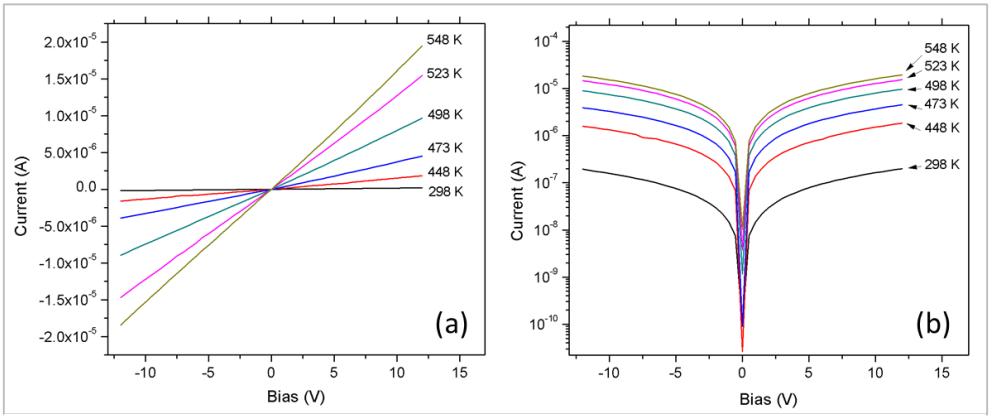

Fig. 58 Current-voltage characteristics of a ZnO MTP sample in N2 atmosphere measured at 6 different temperatures. The data are reported in (a) linear and (b) logarithmic scale.

After acquisition of the IV curves for all temperatures of interest, the value of the conductance of the device for every temperature was computed by linear fitting of the current-voltage curve at low bias, where the dependence is approximately linear.

Estimation of the *conductance* of the device *G=dI/dV* (proportional to the electrical conductivity), for every temperature between 25 and 300°C (298 to 573 K), can allow to understand the characteristic properties of the conduction mechanism of aggregated tetrapod crystals. This can be done because, in general, the thermal dependence of the conductance in the dark can be expressed as:

$$G(T) \approx Ae^{-E_a/kT} \qquad (13)$$

Where *T* is the temperature in Kelvin, *A* is a proportionality constant, *k* the Boltzmann constant and E_a the *activation energy* for the process. Therefore, the following linear relation holds:

$$\ln(G) = \ln(A) - \frac{E_a}{kT} \tag{14}$$

The plot of *lnG* as a function of the inverse of the temperature can thus be fitted linearly to obtain the activation energy E_g: this is commonly called the *Arrhenius plot*.

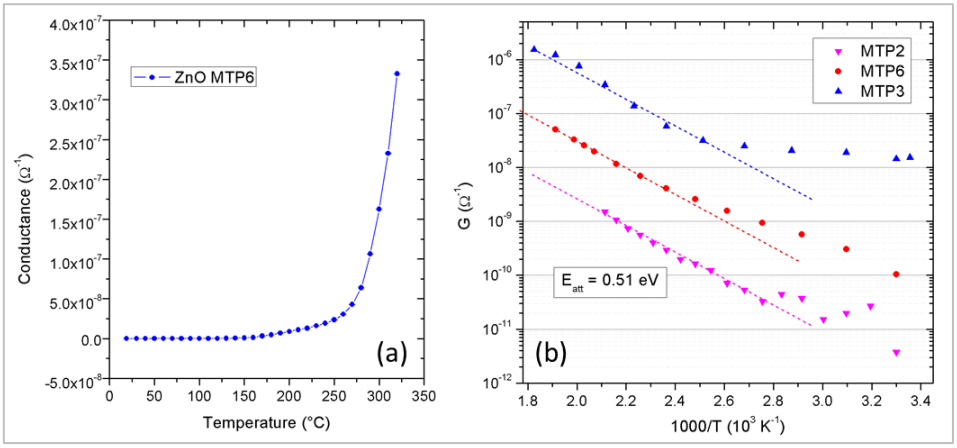

Fig. 59 (a) Conductance G as a function of the temperature T (in °C) for a MTP sample showing the exponential dependence. (b) Arrhenius plot of the conductance for 3 different samples reporting remarkable similarity in the linear fit slope. The activation energy is E_a≈0.5 eV in all three cases.

The conductance of a sample as a function of temperature is reported in Fig. 59-a, showing that the conductivity does not depend on the sample temperature from RT up until about 150°C. From this temperature on, the dependence is clearly exponential, and there is an increase of about 3 orders of magnitude from 150 to 300°C.

The exponential dependence is showed as a linear relation on the Arrhenius plot in Fig. 59-b, which reports the conductance of three different samples of multiple nano-tetrapods (called respectively MTP2, MTP3 and MTP6). Linear fitting of the plot gives the results reported in the following table:

	E_a (eV)	δE_a (eV)
MTP2	0.51	0.01
MTP3	0.53	0.02
MTP6	0.49	0.02

Table 8 Values of the activation energies for 3 different samples obtained from the Arrhenius plot.

The value of the activation energy, which is close to 0.5 eV for all measured samples, can be interpreted as the value of the energy barrier between different nano-crystals in the multiple nano-tetrapod samples [96]. Thus, the sharp increase in the conductance of the devices can be attributed to thermal emission of carriers over the energy barriers at the contact between different nano-tetrapod crystals. Therefore, the conduction of aggregated nano-tetrapods is dominated by these barriers, which are caused by the surface depletion layer, as evidenced by the Schottky current-voltage characteristics of the sample described in Par. 3.6.

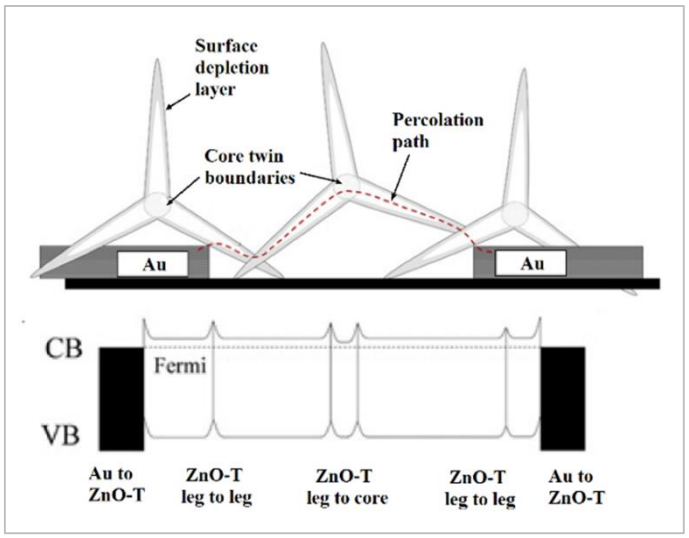

Fig. 60 Schematic representation of the barrier-dominated conduction in MTP samples. To arrive at the electrodes, carriers have to traverse a percolation path passing through several nano-tetrapod crystals. Between each adjacent crystals there is a potential barrier formed by the surface depletion layers.

3.9 Conclusions

The material properties of vapour-grown ZnO nano-tetrapod crystals were investigated using several optical, electrical and electro-optical experimental techniques. The samples were found to have an energy gap close to 3.3 eV, by confronting data obtained by diffuse reflectance spectroscopy, photo-luminescence and photocurrent spectroscopy. Moreover, the distribution energy levels inside the band gap were analysed, mainly by a sensitive photocurrent analysis, described in Par. 3.7.3. A broad, continuous distribution of defect-related levels inside the gap, arising due to crystal disorder or high defect concentration, was assigned to zinc or oxygen vacancies, by comparison with literature data.

More importantly, the unusual photoconduction behaviour of ZnO nano-tetrapods in aggregated form, deposited on gold contacts, was investigated. These samples showed high sensitivity to UV light, the PC increasing several orders of magnitude with respect to its dark value; however, MTP samples have also remarkably long PC rise and decay times when illuminated with UV light, which is problematic for opto-electronic applications of these nano-structures. In fact, under constant illumination, the current continues to grow for hours or days, without reaching a constant equilibrium value in practical times. Moreover, there is a significant persistent PC that remains for days before returning to the initial dark value, as shown in Par. 3.7.1.

As the photo-conduction process in this material is due to O_2 adsorption and desorption processes from the surface, the dependence on external O_2 partial pressure was investigated, and we found an opposite behaviour with respect to what is described in the relevant literature: the PC is enhanced by exposure to a higher external concentration of oxygen, that is the opposite of the expected behaviour.

The same measurements made on STP samples obtained from the same vapour-grown nano-crystals showed however that these have much shorter response times, do not present persistent PC effects, and have higher sensitivity to light in vacuum with respect to air.

The different behaviour can attributed to the different conduction mechanism: in fact, the STP sample is composed of a single crystal, without grain boundaries (Par. 3.2.2), and shows an ohmic IV characteristic (Par. 3.6); this indicates that the STP does not contain important energy barriers to the current transport, and the conduction is *channel-dominated*, just like single nano-wire devices [73] [74].

On the other hand, STP samples show Schottky-type IV characteristics, indicating a *barrier-dominated conduction*: when the sample is illuminated with UV light, the effect of the reduction of the depletion layer thickness at the surface is not as important as the effect of light irradiation and O_2 desorption on the inter-particle barriers.

Barrier dominated conduction tend to enhance UV light sensitivity [28], due to the presence of an electric field that reduces carrier recombination at the inter-particle boundary, but is also responsible for the much longer response times of aggregated

nano-tetrapods, and probably of the reversed dependence on oxygen concentration of PC sensitivity.

The exact mechanism by which the photo-current is influenced by external pressure, inter-particle barriers, and UV light is not clear at present, due to the complex interactions between these variables, the disordered, percolative nature of the sample and due to the long response times of the sample, which limit the number of measurements that can be done.

However, by measuring the temperature dependence of the current and using the Arrhenius plot, we were able to observe the effects of the inter-particle barriers , the height of the inter-particle energy barriers, and to measure their value in dark conditions as about 0.5 eV. This result was verified for different samples and is consistent with observations made by other experimental groups.

Appendix

4 Appendix A: Transient current technique on CdTe and CdZnTe samples

The first part of my doctoral work was not focused on metal-oxides, but on II-VI semiconductors CdTe and CdZnTe (CZT), for x- and γ-ray detectors applications.

This section describes briefly the experimental investigation CdTe and CZT samples by the *transient photocurrent technique*, aimed at characterize the transport properties of these semiconductors and the form of the internal electric field of CdTe and CZT-based detectors when under bias.

4.1 Introduction to CdTe and CdZnTe

CdTe is a II-VI semiconductor with a relatively wide band gap of about 1.5 eV at room temperature, that can be widened to 1.6 eV or more by substitution of a fraction of Cd with Zn atoms, to form the ternary semiconductor $Cd_{1-x}Zn_xTe$, also called *CZT*.

CZT can be viewed as a solid solution between CdTe (E_g=1.5 eV) and ZnTe (E_g=2.2. eV), with an energy gap that is intermediate between the two, and depends on the degree of substitution of Cd atoms with Zn following the relation [97]:

$$E_g = 1.606 + 0.38x + 0.463x^2 + 4.5 \cdot 10^{-4} \cdot \frac{T^2}{264 + T} \ \ eV \qquad (15)$$

Where x is the Zn fraction in $Cd_{1-x}Zn_xTe$, and T is the absolute temperature.

Typically, x≈10%, that gives an energy gap of about 1.6 eV, while maintaining most of the physical properties of CdTe.

4.1.1 General material properties

CdTe and CdZnTe are important materials for fabricating x-ray and γ-ray detectors capable of working at or near room temperature. This is because of the materials interesting characteristics that are suitable for high-energy radiation detection:

1. CdTe has a considerably high average atomic number Z≈50 that enhance the photoelectric effect probability. In CZT, for a zinc fraction of x = 0.1, the value is Z=49, from which the importance of selecting x not too high to balance a wide band gap with high enough Z.

2. Relatively high density, that is necessary to absorb high energy radiation (e.g. 4 mm is enough to absorb efficiently photons with hν≤180 KeV). This, along with the high atomic number, results in high quantum efficiency of the photo-electric process that converts x- and γ-ray photons in e^--h^+ couples.
3. Very high resistivity, about 10^9 Ω·cm for CdTe and 10^{11} Ω·cm for some CZT samples. High resistivity imply low leakage currents and is therefore important when detecting low energy x-rays.
4. Wide band gap (1.5 eV for CdTe and 1.6 eV or more for CZT at RT) reduce thermal noise and allow detectors to work at room temperature.
5. Good electron transport properties ($\mu_e \approx 1000$ cm^2/V·s), but low hole mobility ($\mu_h \approx 120$ cm^2/V·s).

4.1.2 Mobility and lifetime of carriers

In General, the transport proprieties like the carrier mobility μ and life-time τ of the material are the most important properties for all kinds of detector applications. Moreover, high resistivity is of fundamental importance to have high sensitivity and efficiency.

Melt-grown CdTe and related compounds tend to have a native p-type doping, and semi-insulating properties must obtained by doping n-type with Cl or In to achieve compensation of native acceptors.

However, intentional introduction of doping impurities, along with native defects, can decrease the values of mobility and lifetime of carriers, degrading the properties of the material. In fact, the mobility is limited by scattering between carriers and charged defects, while lifetime decrease with the increasing concentration of defects either by trapping or recombination effects. In general, reduction of the carriers' μτ product in the material, degrades the energy resolution of the detectors, thus affecting negatively the performances of spectroscopic sensors based on CdTe and CZT.

In order for the effect of defects to be negligible, the transit time of the carriers in the detector t_d must be much smaller than the lifetime of the charges τ:

$$t_d = \frac{d}{\mu E} = \frac{d^2}{\mu V} \ll \tau \qquad (16)$$

Where d is the thickness of detector that must be traversed by the carriers, while E and V are respectively the electric field and applied voltage. This is an approximate formula that holds as stated only for planar detectors with uniform electric field, but it gives insight on the importance of the mobility-lifetime product of the material from which is made. To work properly as a spectroscopic detector, the semiconductor has to verify:

$$\mu\tau \gg \frac{d^2}{V} \qquad (16)$$

In principle, it might be possible to reduce t_d in Eq. (16) by simply increasing the voltage applied to the detector (for a fixed thickness). However at the same time the leakage current inside the device increases with the applied voltage thus increasing the background noise value. Is important therefore to have a good $\mu\cdot\tau$ value to achieve good spectroscopic resolution. Usually CZT detectors operate with electric field in the range between 1000-2000 V/cm.

When growing CdTe or CdZnTe crystals for high-energy photon detection application, or when testing a prototype device, it is therefore of primary importance to have a method to measure reliably and non-destructively the values of the mobility and life-time of the samples.

4.2 Signal formation in x- and γ-ray detectors

The simples form of photo-detector is a parallelepiped slab of single-crystal semiconductor material of thickness *d<<l*, with *l* being the lateral dimensions of the device. A simple planar semiconductor detector is shown in Fig. 61. The electric contacts are provided by two metal electrodes on two parallel and opposite plane surfaces.

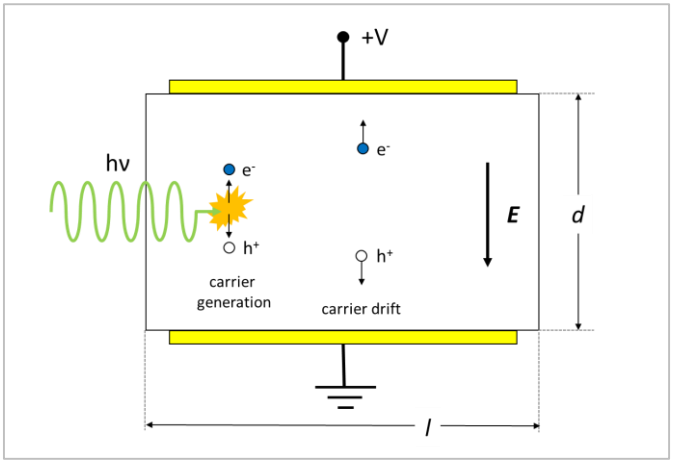

*Fig. 61 Schematic diagram of a planar detector of thickness d and length l. The detector is biased at +V with respect to ground generating an uniform electric field **E** inside the device. Electrons and holes are indicated with e^- and h^+ respectively.*

A voltage ΔV difference is maintained across the two metal electrodes generating an uniform electric field **E**.

When a x- or γ-ray is absorbed by the detector via *photoelectric interaction* (that is the most important generation process for CdTe and CZT), carriers pair are generated in a number that is proportional to the incident photon energy hv.

Electrons and holes in the generated cloud are immediately separated by the applied bias: electrons drift in the direction of the positive contact and holes drift in the opposite direction (cathode). Typically, the active layer of the detector is fabricated with high resistivity materials, or constitute the depletion area of a diode junction: for this reason, charges move inside a layer that is almost completely depleted of free carriers. Thus, the only free carriers present other than those produced by the incoming radiation, are the thermally electron-hole pairs, which are responsible for the dark current.

In high resistivity materials like CdTe and CZT, there are not enough free carries to shield the charge of the cloud when it travels inside the material subject to the applied field. This means that after separation, electron and holes can induce a current onto the electrodes as they drift: i.e. the signal is generated by *charge induction*, as opposed to charge collection.

4.2.1 Ramo-Shockley theorem

The calculation of induced charge on any number of electrodes due to a moving charge can be found using the *Ramo-Shockley theorem*, which holds whenever there is no space charge, or when the space charge is fixed.

Consider now a general system constitute by N electrodes at constant voltage V_i (i=1, 2, ..., N) with relative surfaces S_i, a moving charge q and a spatial static charge ρ(x). In this case, the charge *Q* and the current *i* induced on an electrode by a moving charge q is given by the Ramo-Shockley theorem as:

$$Q = -q\varphi_0(\boldsymbol{r}) \tag{17}$$

$$i = \int q\boldsymbol{v}(\boldsymbol{r}) \cdot \boldsymbol{w}(\boldsymbol{r}) d\boldsymbol{r} \tag{18}$$

where *q* is the value of the moving charge, *v* is the instantaneous velocity of the charge, while $\varphi_0(\boldsymbol{r})$ and $\boldsymbol{w}(\boldsymbol{r})$ are called respectively the *weighting potential* and *weighting field* of the configuration of electrodes in the instantaneous position ***r*** of the charge q. These last two quantities can be calculated in **r** by placing the selected electrode at *unit potential*, all other i-1 electrodes *grounded*, and removing all charges in the system (q and ρ(**r**)).

An important corollary is that the charge induced is independent from the space charge ρ(**r**) and the actual value of the potential applied at the N electrodes.

4.2.2 Current transient

When considering the current generated by a short pulse of light with energy $h\nu \geq E_g$ inside a semiconductor detector, one can use the Ramo-Shockley theorem to deduce the shape of the current transient. Considering a plane detector of thickness d, in which z is the point between cathode (set at z=0) and the anode (z=d), the weighting field is constant in module and has the simple form:

$$w(z) = {}^{1}/_{d} \tag{19}$$

In this simple case, for a photon absorbed at a depth z_0 inside the detector, the R-S theorem for the total current takes the form:

$$i = \int_{z_0}^{d} en(z,t)w(z)\mu_e E(z)dz + \int_{0}^{z_0} ep(x,t)w(z)\,\mu_h E(z)dz \tag{20}$$

Where n(z,t) and p(z,t) are the electron and hole densities, w(z)=1/d is the weighting field, μ_e and μ_h are the electron and hole mobilities and E(z) is the electric field in the material.

If the light pulse is not highly penetrating, such as for visible light, absorption by the material happens in the first few μm below the surface, and, for a relatively thick detector $z_0 \approx 0$. In this case, it is clear from Eq. (20) that only electrons contribute to the current, the second member of the equation being negligible. If the polarity of the detector is reversed, the opposite happens, and only holes give rise to a signal.

Considering carrier trapping, the density of electrons generated by an instantaneous light pulse, can be expressed as:

$$n(z,t) = n_0 e^{-t/\tau}\,\delta[z - z(t)] \tag{21}$$

Where n_0 is the density of generated carriers and τ is the electron life-time due to trapping.

Therefore, one obtains for the current pulse:

$$i(t) = \frac{\mu_e Q_0 e^{-t/\tau}}{d} E[z(t)] \tag{22}$$

Where $Q_0 = en_0$ is the initial photo-generated charge, while z(t) is the barycentre of the charge cloud as it drifts inside the detector.

It is important to note the direct dependence of the photo-generated current from the shape of the electric field E(z) along the thickness z of the detector. The total collected charge, that is the integral of the current pulse signal, also depend on the electric field shape when trapping is present; the maximum collection is obtained when the field is uniform, and the collected charge is reduced when the field profile deviates from this special case.

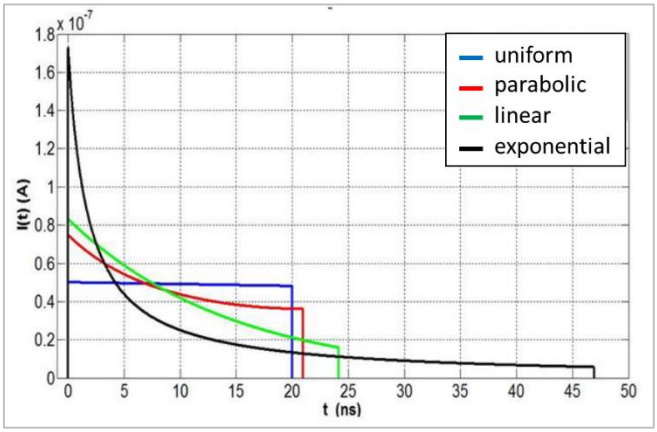

Fig. 62 Example of current transients for pulsed excitation in a planar detector calculated for different shapes of the electric field E(z).

4.3 Electric field inside a detector

The spatial profile of the electric field inside a biased solid-state photodetector depends not only on the material quality (impurity concentration and homogeneity) but also on the nature of the electrical contacts. In a planar detector, the creation of *space charge* due to trapping produces a deviation of the electrical field profile from the ideal uniform one. As photo-detectors are typically made of semi-insulating semiconductor materials, to reduce the dark current and improve the signal-to-noise ratio, a number of theoretical and experimental work has been done trying to understand the behaviour of the electric field inside semi-insulating materials [98] [99] and to construct suitable theoretical models that describe it [100] [101].

One well-known relatively direct method to investigate the profile of the electric field is by making use of the Pockels effect [102]. Alternatively, the electric field can be investigated indirectly, by measuring the *time of flight* (TOF) and analysing the shape of a current pulse: this method is commonly known as the *transient current technique* (TCT). Brief current pulses can be induced in the detector by irradiation with pulsed lasers or alpha particles; the shape of the pulses can then be analysed to evaluate the carriers' mobility μ and lifetime τ.

Additionally, from the shape of the pulses should be possible to deduce the profile of the electric field. Much effort was spent to reconstruct the electric field from the TCT measurements in the last decades, however, results were obtained only under strong hypotheses, such as absence of carrier trapping (infinite carrier lifetime) [99]. However, carrier trapping is important in semi-insulating materials like CdTe and CZT, due to compensation and native defects.

Another approach is to hypothesize a particular shape of the field in advance, typically a linear dependence on the depth z inside the material, and to deduce the free parameters like the slope and the strength at the cathode [100].

However, recent experimental findings and simulations have shown clearly that the electric field inside a semi-insulating detector is non-constant with a typically non–linear shape in most operating conditions [102] [103] suggesting the need to search for a more general method to reconstruct its spatial distribution.

4.3.1 TCT field reconstruction method – Theory

To arrive at an experimental method capable of determining the field inside a semi-insulating material, it is necessary to deduce the exact dependence of the current from the electric field profile in the experimental conditions, i.e. in a plane detector irradiated by pulsed light at $h\nu \geq E_g$.

In Par. 4.2.2 we have already pointed out that only one carrier type contribute to the current pulse for non-penetrating (i.e. visible) radiation, and we arrived at Eq. (22), describing the dependence of the pulse from the electric field profile E[z(t)].

E[z(t)] is the electric field at the depth z(t) inside the detector, as experienced from the charge carrier travelling towards its collecting electrode following the laws of motion. The only assumption made are negligible de-trapping of carriers, independence of μ and τ from the electric field, and negligible carrier diffusion.

The problem is that the electric field does not appear as simply E(z), but as it is observed by a charge carrier moving along the barycentre of the charge cloud z(t), so it should be necessary to know the law of motion z(t) to extract the field profile directly.

However, we know that the electric field profile must satisfy two physical constraints regarding the sample thickness d and the applied voltage V_i:

$$d = \int_0^{T_i} v[z(t)]dt = \mu \int_0^{T_i} E[z(t)]dt \tag{23}$$

$$V_i = \int_0^{d} E(z)dz = \mu \int_0^{T_i} E^2[z(t)]dt \tag{24}$$

Where T_i is the transit time of the charge at the voltage V_i. Using Eq. (22) we obtain:

$$Q_{0i} = \int_0^{T_i} I_i(t) e^{t/\tau} dt \tag{25}$$

$$\mu Q_{0i}^2 = \frac{d^2}{V_i} \int_0^{T_i} [I_i(t) e^{t/\tau}]^2 dt \tag{26}$$

The current transient profile $I_i(t)$ and the transit times T_i are quantities that can be measured experimentally at different values of the voltage V_i, with i=1,2, …, N.

The first term Q_{0i} of Eq. (25) can be calculated numerically as a function of τ, for each i. In this way, one obtains a series of N curves $Q_{0i}(\tau)$ that can be plotted together: the N curves then should ideally cross each other at the correct value of the life-time τ of the material. In practice, experimental curves do not cross exactly in one point, but come closest together in an area that contains the true value of the lifetime τ. The best value of τ can thus be obtained by minimizing the weighted variance of Q_{0i}.

The same procedure can be applied separately to Eq. (26) that therefore provide an additional method to obtain the best value τ. A suitable value of the lifetime τ could be the average of two values from the two minimization procedures.

After deducing the value of τ, the initial photo-generated charge Q0 and the mobility μ can then be calculated easily. Thereafter, the law of motion z(t) can be deduced, that allow to reconstruct the electric field profile E(z) inside the material [104].

4.4 Transient current technique

The method was tested on cadmium telluride and cadmium zinc telluride planar detectors, of thickness on the order of a few mm. These materials have a suitably high resistivity and have high PC response to above-gap light. Moreover, due to the high resistivity, standard methods to measure the mobility and lifetime of carriers, like the Hall effect, do not provide accurate informations.

To measure current pulses suitable for the investigation of the transport properties of the material and reconstruction of the electric field, the transient current technique was used.

The sample is excited by illumination with a pulsed laser beam on the surface of one of the two planar electrodes. As photons of the laser are absorbed in a very small thickness below the illuminated surface, by selecting which contact is illuminated (or reversing the sample polarization), it is possible to isolate the contribution of electrons (or holes) to the induced current pulse.

The optical source is a *Koheras supercontinuum pulsed laser*, with an optical output spectrum that covers the range from 500 to 2000 nm and provides a total optical power of 100 mW. Optical pulses are less than 2 ns long with repetition rate of about 25 kHz and the wavelength is selected by means of a narrowband (10 nm full width at half maximum, FWHM) filter with transmission peaked at 820 nm. Due to the low value of the penetration depth at that wavelength, the device is measured in a single carrier transport configuration.

For every different bias applied to the detectors, a few hundred current pulses were averaged to increase the signal-to noise ratio, and to average out every possible laser instability, to allow a constant value of the photo-generated charge Q_{0i}.

The output of the detector was amplified about 60 times by a custom-made amplifier with a bandwidth of 80MHz and very low noise. The detector was biased using a Keithley 237 High Voltage Source-Measure Unit between 5 and 200 V.

The data in Fig. 63 was acquired in these conditions using a CdTe planar detector of thickness 1 mm with platinum electrodes. The sample was held at negative bias to measure the electronic current data (i.e. the laser impinging on the cathode).

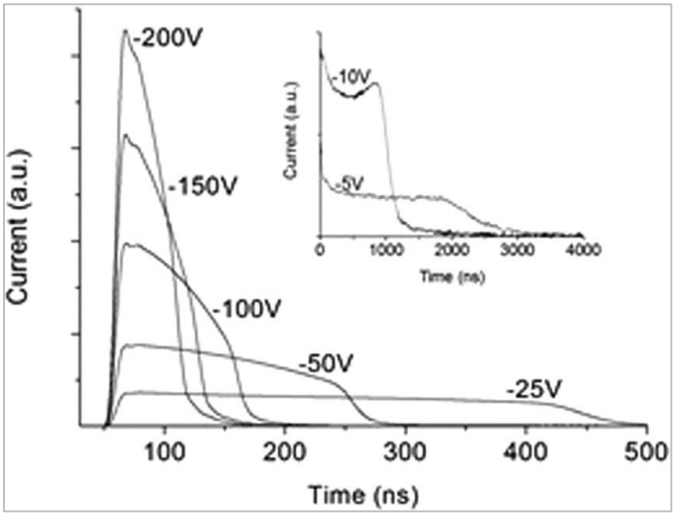

Fig. 63 TCT data for a CdTe sample of 1 mm thickness, obtained illuminating the sample with a 820 nm pulsed laser source. The sample was biased at different voltages between -5 and -200 V.

The current pulses are characterized by a sharp rise, an intermediate decay due to electron drift and with trapping of carriers, and then there is a diffusion related decay (tail) at the end of the pulse. Simulations show that the transit time for each applied bias can be obtained as the time difference between the flex points of the sharp rise and diffusion-related decay respectively.

4.5 Reconstruction of the electric field

The theoretical model described in Par. 4.3 can be then used to calculate the transport parameters for the electrons. In order to do so, the value of the transit times for every value of the applied voltage V_i must be obtained from the data. Then, the quantities in Eqs. (25) and (26), can be calculated as a function of some values of the life-time τ in a range chosen so as to contain the probable true value τ_R.

Let us fix a value for lifetime τ in this range: for each value of measured bias V_i we obtain $Q_{0i}(\tau)$ and $\mu Q_{0i}^2(\tau)$. As the total charge generated was kept constant for every applied

voltage, every curve of either family intersect each other ideally in only one point, that is the "true" value of the lifetime. Therefore, as we shall see the value of τ can be obtained in two independent ways. The mean and the variance value over the index i can be calculated for every value of τ: in this way, for every τ one can evaluate the dispersion about the mean value using the following quantities, that are weighted for the errors estimated from Eqs. (25) and (26):

$$Y_1(\tau) = \ln \sum_i \left(\frac{Q_{0i}(\tau) - \langle Q_0(\tau) \rangle}{\delta Q_{0i}(\tau)} \right) \tag{27}$$

$$Y_2(\tau) = \ln \sum_i \left(\frac{\mu Q_{0i}^2(\tau) - \langle \mu Q_0^2(\tau) \rangle}{\delta [\mu Q_{0i}^2(\tau)]} \right) \tag{28}$$

Where the quantities between '< >' represent mean values calculated over the index i, while the quantities preceded by 'δ' represent the errors relative to those quantities.

Y_1 and Y_2, are dimensionless quantities that can be minimized with respect to τ, to obtain two well defined best values for the life-time τ_{R1} and τ_{R2}. The minimization procedure is shown in Fig. 64.

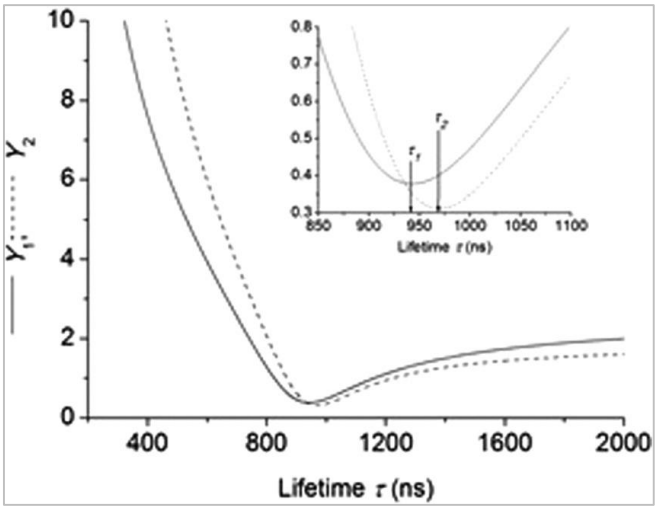

Fig. 64 Representation of the quantities Y_1 and Y_2 as a function of τ showing that these possess two minima that are very close to each other, that represent the real value of the lifetime of the material.

As expected, the two quantities possess two minima that are remarkably close to each other. The average of these two is the best value for the lifetime of the material τ_R that can be deduced from the current transients: τ_R= 956 ±18 s. Consequently, the electron mobility is μ= 1049 ±20 cm^2/Vs. The mobility-lifetime products is therefore (1.00 ±0.04) $\cdot 10^3$ cm^2/V, that in remarkable agreement with values estimated from charge collection efficiency measurements reported in literature [105] [106].

It is important to underline that an accurate determination of the carrier lifetime requires low bias measurements, because at high bias the transit time may be lower than the carrier lifetime, introducing an exponentially large error in the determination of the lifetime itself.

After having obtained the relevant transport parameters, the electric field profile along the sample thickness can be deduced. The results are shown in Fig. 65 for various applied voltages.

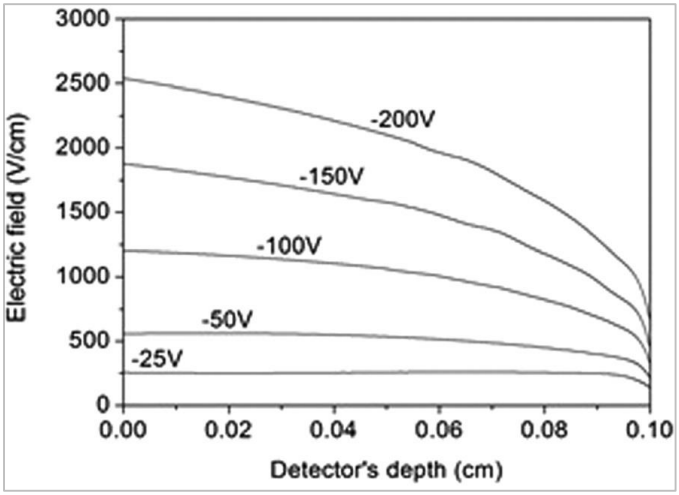

Fig. 65 Electric field profile inside the CdTe detector at different biases, as obtained from the current transients through the minimization procedure described.

As can be readily observed from the data in Fig. 65, the field's strength decrease steadily from cathode to anode: this effect is due the presence of a positive space charge density of 10^{10}-10^{11} cm^{-3} present inside the CdTe sample, and this value is consistent with what was reported in literature for similar samples [107].

The described procedure to reconstruct the electric field is highly sensitive to the time profile of the laser pulses, and this effect is particularly important when deducing the value of the field near the electrodes. This is due to the non-instantaneous generation of the carriers due to the finite time- FWHM of the laser pulse. To overcome this problem, the current transients have been deconvoluted from the laser pulse shape.

4.6 Other examples - CdZnTe

The TCT technique thus validated was used to measure the transport parameter of samples of CdZnTe, and to reconstruct the electric field inside the material.

The current transients of different CZT plane detectors with Au contacts deposited via electro-less technique were measured with a green *Polaris Nd-YAG pulsed laser* at 532 nm, with pulses about 4 ns long. Subsequently, the transport parameters were obtained by the minimization procedure describe earlier, and used in order to reconstruct the profile of the electric field.

4.6.1 Sample 42M

This sample is composed of CdZnTe with 10% Zn concentration grown by boron-encapsulated vertical Bridgman technique. Sample thickness is 2.5 mm.

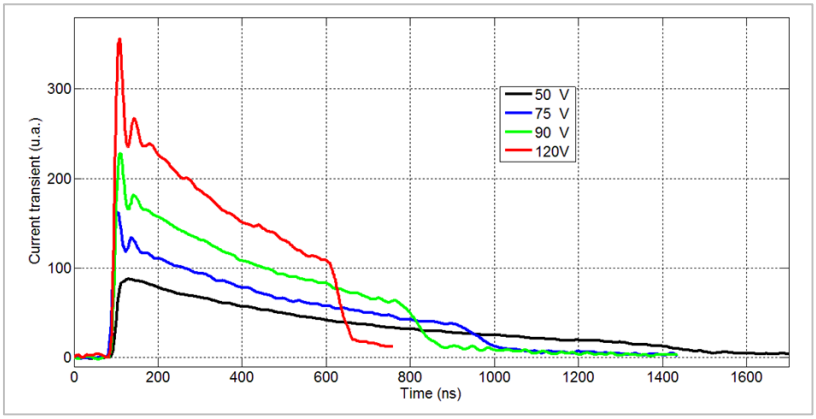

Fig. 66 Current transients obtained with green pulsed laser for CZT sample 42M of 2.5 mm thickness.

The values for the electron lifetime and mobility obtained from the current transient in Fig. 66 are:

$$\tau = 980 \pm 30\ ns$$

$$\mu = 1020 \pm 40\ \frac{cm^2}{V \cdot s}$$

The reconstructed field at different applied voltages is reported in Fig. 67. It is important to observe how the initial oscillation of the current, that is probably due to electromagnetic noise caused by high voltage switching in the pulsed laser electronics components, is reported as a disturbance in the reconstructed field near the cathode. The region near the electrodes is the most affected by unwanted interference effects and to broadening due to non-instantaneous carrier generation (the laser pulse duration is ≈4 ns, so that the charge cloud is not exactly a δ function, but instead has a Gaussian

profile with a FWHM depending on pulse duration and value of the field at the generation point).

For these reasons is important to thoroughly shield the detector from electromagnetic radiation and use lasers with pulse width $\Delta t << T_r$, T_r being the transit time of the carriers.

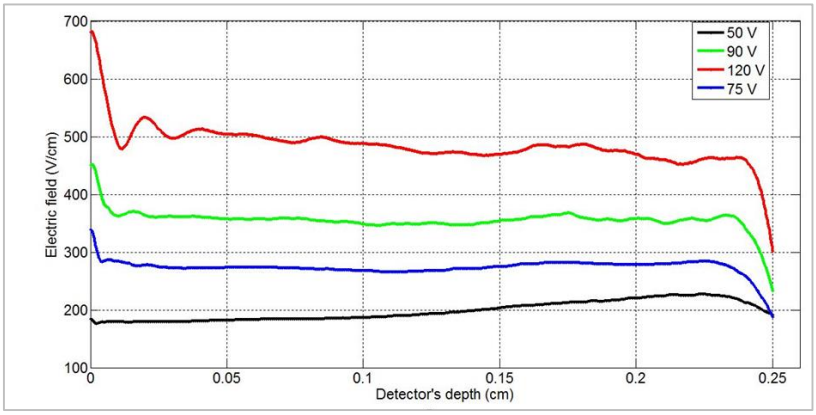

Fig. 67 Reconstructed field for CZT sample 42M at different voltage. The cathode is at z=0 cm (z=detector depth).

This thick sample shows remarkably uniform electric field at every value of the applied potential: this is an optimal characteristic for x- and γ-ray detector applications as it allows the maximum possible charge to be collected.

4.6.2 Sample 26

This CZT plane detector is relatively thin, being only 0.5 mm thick.

The current transients were measured using a green 532 nm Nd-YAG pulsed laser as before, and the results are reported in Fig. 68. Due to the small thickness, only low bias measurements were done. In fact, for the technique to work properly, the transit time of the carriers t_r (i.e. the time of flight) must be longer than the carrier lifetime τ. If not, the current pulse shape does not depend significantly on carrier trapping, thus introducing large errors in the determination of τ.

The transit time depends on the carriers mobility μ and on the module of electric field E inside the sample; therefore, one can use the simplest possible model (uniform electric field) to estimate the maximum useful bias for a sample of thickness d through the following relation:

$$t_r \approx \frac{d}{v} = \frac{d}{\mu E} \approx \frac{d^2}{\mu \Delta V} > \tau \qquad (29)$$

Where v is the relevant carriers' velocity, and ΔV is the applied bias. From Eq. (29) it follows that:

$$\Delta V < \frac{d^2}{\mu \tau} \qquad (30)$$

In the case of *sample 26*, with d=0.5 mm, and assuming τ≈500 ns and μ≈1000 cm^2/Vs (typical values for CZT), one obtains that the bias has to be less than about 5 V.

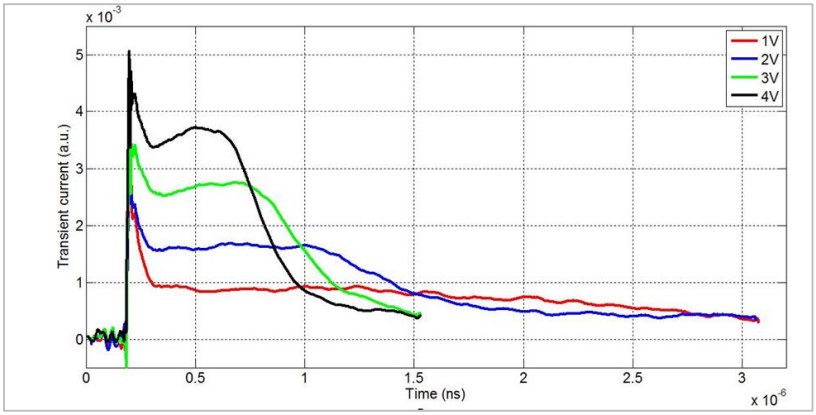

Fig. 68 Current transients at different voltages of CZT sample 26. Low bias values were used due to the low thickness of the sample, according to Eq. (30).

Values of the transport parameters obtained from TCT data reported in Fig. 68 are:

$$\tau = 510 \pm 40\ ns$$

$$\mu = 1170 \pm 60\ \frac{cm^2}{V \cdot s}$$

The electric field reconstructed using the obtained values of μ and τ is reported in Fig. 69 for different values of the applied bias.

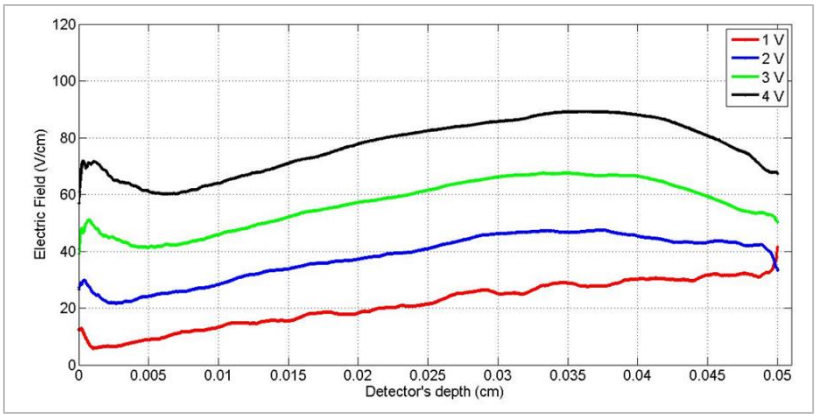

Fig. 69 Reconstructed electric field at various tensions for sample 26. The origin of the z axis represent the position of the cathode (z is the depth in cm).

4.7 Conclusions

The laser-excited transient current technique was used to investigate the material properties of II-VI semiconductors CdTe and CdZnTe that are typically used for x- and gamma-ray detector applications. As the most important transport properties for these applications are the mobility and lifetime of carriers, as well as the profile electric field inside the detector under bias, the problem of obtaining these quantities from TCT measures was investigated. The problem has been solved by an original method that analyse the transient current data obtained using visible or NIR laser pulses to excite the carriers.

The theoretical basis of the method used does not make assumptions on the conduction parameters or the shape of the electric field, so is more general than methods proposed earlier. The procedure is based simply on physical constraints imposed by the detector's thickness, the applied voltages, and the constancy of the amount of photo-generated charge from each laser pulse. Then, by using a minimization procedure, the transport parameters μ and τ of the analysed materials can be extracted. Finally, the electric field profile has been deduced for different samples of CdTe and CZT. The only approximations made were to neglect the effects of diffusion and de-trapping, but improvements of the method that take into account these effects are in progress.

Results obtained on CdTe and CdZnTe planar detectors with this technique are in remarkable agreement with data obtained from literature, thus validating the whole technique.

5 Appendix B – Experimental instruments and techniques

This section provides a more detailed description of the experimental instruments used in this thesis, along with the experimental methods used to make the measurements that appear in Ch. 1 to 4. The theory regarding these techniques is also included.

5.1 Optical transmission and diffuse reflectance spectroscopy

Transmission and reflectance spectroscopy refer to analytical techniques based on measuring the amount of light that interact with a sample at a given wavelength, i.e. by being absorbed or reflected away.

In general, if there is interaction between a photon of energy $h\nu = hc/\lambda$, and the microscopic structure of a material, is because there is a transition between two energy levels E_1 and E_2, so that:

$$h\nu = E_1 - E_2 \tag{31}$$

The nature of the levels E_1 and E_2 involved in the transition depends on the characteristic energy of the photons: for photon wavelength is between about 200 to 1000 nm (UV-VIS-NIR range), these are electronic transitions.

For isolated atoms or molecules, such as in a gas, electronic levels E_n are discrete, and every level can at most contain two electrons.

For a solid material such as a semiconductor, quasi-continuous energy bands $E_n(\mathbf{k})$ take the place of discrete levels: for every band, there is a large number of levels, each defined by a different state of motion of the electron, which is represented by the wave vector **k**.

5.1.1 Theory of transmission spectroscopy

Transmission spectroscopy for a crystalline sample like a thin film of a semiconductor material, consists in the measurement of the ratio between the intensity I of light transmitted through a sample and the intensity of the incident light I_0, as a function of the wavelength λ. This ratio is called the *transmittance* of the sample T:

$$T = \frac{I(\lambda)}{I_0} \tag{32}$$

The value of T as a function of the wavelength (or photon energy) is the *transmittance spectrum T(λ)*. A common way of representing this is by using the *absorbance A*, that is measured in *optical densities* (OD):

$$A = -log_{10}(T) = -log_{10}\left(\frac{I}{I_0}\right) \tag{33}$$

For a solid material, the transmitted intensity I depend on the thickness d travelled by light of wavelength λ inside the material by an exponential relation:

$$I = I_0 e^{-\alpha \cdot d} \tag{34}$$

Where α is known as the absorption coefficient of the material (measured in cm^{-1}), that is in general is a function of the wavelength of the incident light.

To determine the dependence of the absorption coefficient from the photon energy in the case of a semiconductor material, we can make the assumption that the electrons in the materials have a behaviour that does not deviate strongly from that of a free electron, at least in the proximity of k=0 (Γ point) [108]:

$$E_{e,h}(\boldsymbol{k}) = E_{e,h}(0) \pm \frac{\hbar^2 k^2}{2m_{e,h}} \tag{35}$$

Where **k** is the wave vector of the carriers, while m_e and m_h are the effective masses of electrons and holes respectively, which depend on the curvature of the corresponding energy bands.

When a photon of light with energy $h\nu \geq E_g$ is absorbed in a direct semiconductor, there is a direct transition of an electron between the top of the valence band and the bottom of the conduction band ($\mathbf{k}_1=\mathbf{k}_2=0$), leaving behind a hole in the valence band. That is, there is absorption with formation of an e-h couple only for energies above the gap (see Fig. 70-left).

On the other hand, in an indirect semiconductor the top of the VB happens to be at a different **k** value than the bottom of the CB (see Fig. 70-right): in this case, a transition between the two bands need to include the emission or absorption of a phonon to provide for the Δk between the band extrema, because electron transitions with $\Delta\mathbf{k}\neq 0$ are forbidden [108] [109] [110].

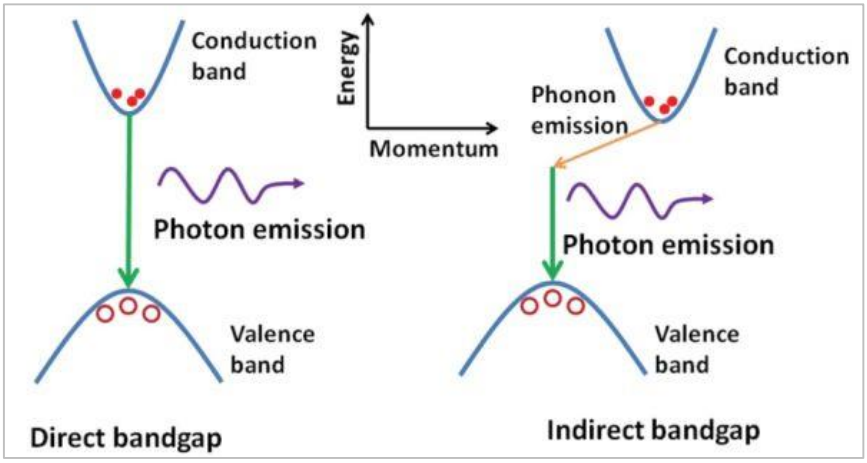

Fig. 70 Direct (left) and indirect (right) transitions in semiconductor materials with direct and indirect band gap respectively.

It can be shown [109] [110] that, under the approximation of *parabolic bands*, the absorption coefficient for *direct band gap semiconductors* depends from the photon energy hν as:

$$\alpha_{dir} = A\frac{(E_g - h\nu)^{\frac{1}{2}}}{h\nu} \tag{36}$$

Where the constant A depends from the characteristics of the material.

In a similar way, for *indirect band gap semiconductors* the absorption coefficient has the form:

$$\alpha_{ind}^{a,e} = C_{a,e}(h\nu - E_g \pm \hbar\omega_{ph})^2 \tag{37}$$

Where *a* and *e* represent respectively the absorption and emission of a phonon of energy $\hbar\omega_{ph}$ (which is normally negligible with respect to hν and E_g), while C_a and C_e are constant that depend on the material and on the temperature. The temperature is important because of the fact that the transition probability for indirect semiconductors depend strongly on the population of phonons inside the crystal.

5.1.2 Determining the energy gap – the Tauc plot

For what was described earlier, is evident that, in a semiconductor, light is transmitted (i.e. the material is transparent) if $h\nu<E_g$, while is absorbed if $h\nu\geq E_g$, so that the absorption spectrum has an edge at photon energies that correspond to the energy gap.

As a consequence, after having measured the *transmission spectrum* $T(\lambda) = I(\lambda)/I_0$ (or $A(\lambda)=-\log_{10}T$, see Eq. (33)) for a new material, it is possible to use the shape of the absorption edge to precisely determine the value of E_g. In fact, knowing the thickness of the sample is possible to determine the absorption coefficient α from Eq. (34), and, if

the material has a direct band gap, Eq. (36) can be used to construct the Tauc plot, that is, a plot of $(\alpha h\nu)^2$ vs. hv. From Eq. (36) one obtains that:

$$(\alpha_{dir} \cdot h\nu)^2 = A(h\nu - E_g) \qquad (38)$$

So that a linear fit of the *absorption edge* will intersect the hv axis at the value of E_g [49] [50]. In the case of an indirect gap semiconductor, a similar approach can be followed by using Eq. (37) instead of Eq. (36). An example of this method is reported in Fig. 71.

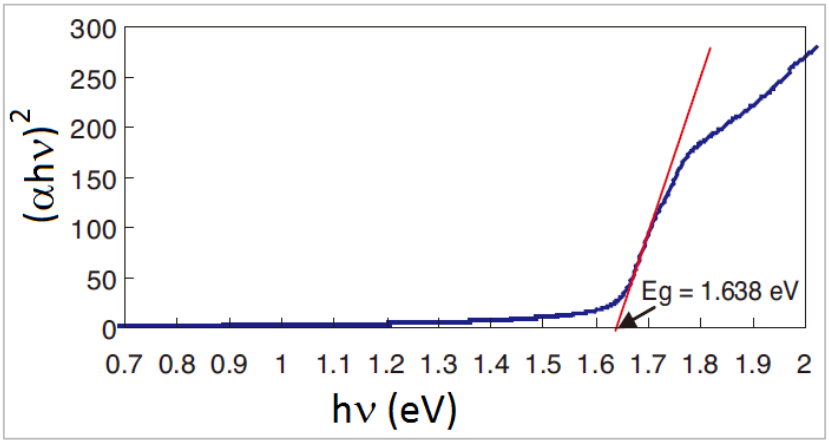

Fig. 71 Example of a Tauc plot for a semiconductor material: $(\alpha h\nu)^2$ is plotted as a function of the photon energy hv (blue line), and the absorption edge is fitted linearly to obtain the value of the optical band gap E_g=1.638 eV.

It is important to note, however, that the Tauc plot method is based upon the parabolic bands approximation of Eq. (35) and on a clear distinction between direct and indirect transitions; due to this fact, the method itself can be unreliable if these conditions are not met exactly. This can happen when one or more bands deviate strongly from the parabolic shape, such as in the case of an extremely flat VB, typical characteristic of metal-oxides, or when there is a mixture between direct and indirect transitions, that can happen if there are more than one CB minima with similar energy.

5.1.3 Diffuse reflectance spectroscopy

When the sample is a solid but not a single crystal nor a uniform single block of material (e.g. the sample is in powder form), diffuse reflectance become the optical technique of choice to analyse the sample.

Diffuse reflectance relies on the focused projection of the spectrometer beam into the sample where it is reflected, scattered and possibly transmitted through the sample material (Fig. 72). The back reflected, diffusely scattered light (some of which is

absorbed by the sample) is then collected by the accessory and directed to the detector optics.

Only the part of the beam that is scattered within a sample and returned to the surface is considered to be diffuse reflection.

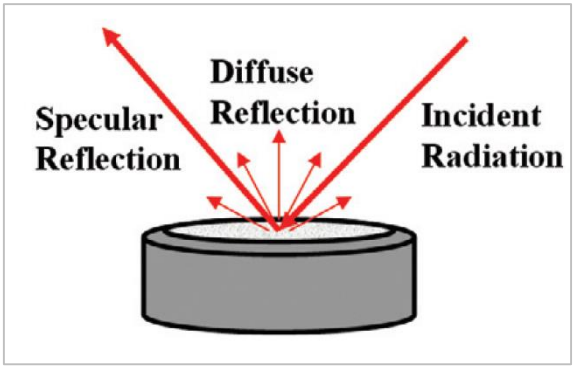

Fig. 72 Diffuse and specular components of the reflection of light out of a scattering sample

As a general rule, samples tend to scatter or reflect light in the region below the gap (i.e. where the sample is transparent), while absorb photons that have $h\nu \geq E_g$. As a consequence, the *diffuse reflectance spectrum* $R(\lambda)=I(\lambda)/I_0$, where I(λ) represent the intensity of scattered light of wavelength λ, is maximum (R≈1) when hν (= hc/λ) is below E_g and falls to nearly zero for $h\nu >> E_g$.

Apart from this general behaviour, however, the diffuse reflectance spectrum is quite different from the transmission one described earlier. To deduce the value of the energy gap from the diffuse reflectance, it is necessary to transform the spectrum R(λ) into a quantity that is proportional to T(λ), from which is then possible to deduce E_g using Eq. (38) or an equivalent one.

The conversion can be done using the *Kubelka-Munk theory* [89], which assumes, among other things, an infinite thickness of material (i.e. negligible transmitted intensity trough the sample) and particles of size comparable to, or smaller than, the wavelength of incident light. Under these conditions, the Kubelka-Munk relationship is:

$$f(R) = \frac{(1-R)^2}{2R} = \frac{K}{S} \qquad (39)$$

Where K is the molar absorption coefficient and S is the scattering coefficient of the sample.

Under the assumption of a perfectly diffuse scattering (or at 60° incidence) the linear absorption coefficient α is related to the molar one simply by K=2α [90], so that, assuming that the scattering coefficient is constant with respect to λ, it is possible to use the quantity f(λ) in place of α(λ) for the Tauc plot (Eq. (38)) to determine the energy gap of the material.

5.1.4 UV-VIS Spectrophotometer

The instrument we used to acquire transmission and diffuse reflectance spectra of metal-oxide samples is a *Varian 2390 UV-VIS-IR double-beam spectrophotometer*, operating in the 200-800 nm wavelength range.

In *transmission mode*, after light coming from the source is monochromatized by a diffraction grating, the light beam is split into two by a semi-transparent beam-splitter: one of the two identical beams passes through the sample, while the other one is brought to a reference (see Fig. 73).

The instrument simply measures the intensity of light I(λ) transmitted through the sample and compares this value to the intensity I0 of the beam transmitted through the reference. The reference is chosen so that, after the comparison of the two beams, only the component of interest of the sample is measured. For example, to measure the transmission spectra of a Ga_2O_3 thin film deposited on an Al_2O_3 substrate, the reference chosen was a blank alumina substrate of the same thickness.

The measured intensity for every wavelength in the 200-800 nm range is the transmittance spectrum, given as $T(\lambda)= I(\lambda)/I_0$ or as $A(\lambda)=-\log_{10}T$ (in OD).

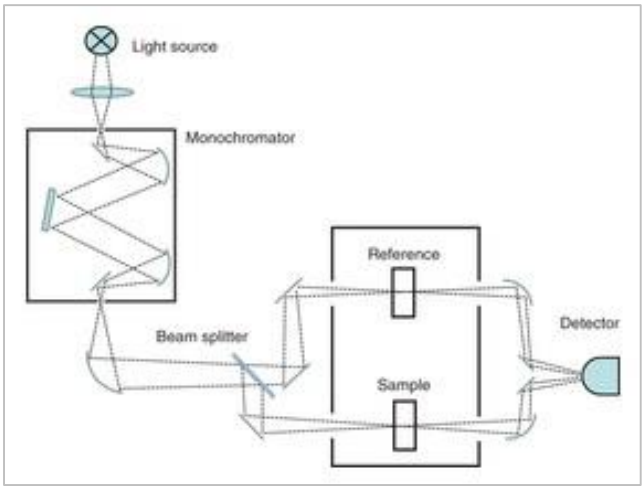

Fig. 73 Outline of the UV-VIS-NIR double beam spectrophotometer when used in transmission mode.

In *diffuse reflectance mode*, the measuring beam enters a BaO (barium oxide) coated *integrating sphere*, in which the sample is placed; in this way, light scattered by the sample in every direction can be collected by the detector, that gives onto in an aperture cut on the surface of the sphere (see Fig. 74). BaO is used due to the optimum reflectance in the UV-VIS-NIR range, which is very close to 100%; in this way there are negligible intensity losses when light is reflected back and forth inside the sphere.

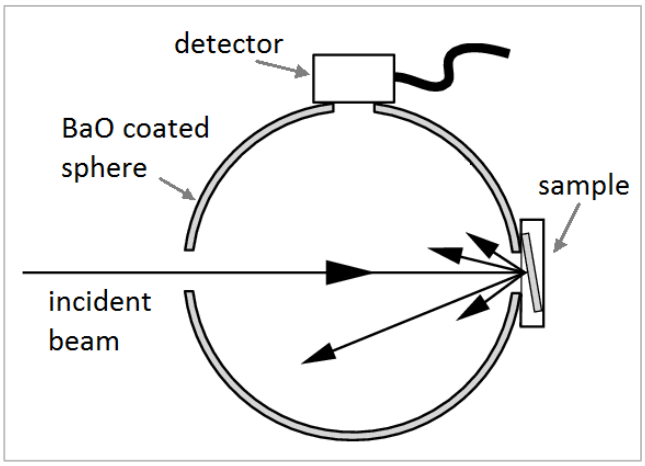

Fig. 74 Integrating sphere for the measurement of the diffuse reflectance spectrum of a sample

5.2 Photoconductivity

Photoconductivity (PC) is the mechanism by which absorption of light of opportune wavelength (i.e. energy) produce an increase in the conductivity of a semiconductor sample (Fig. 75).

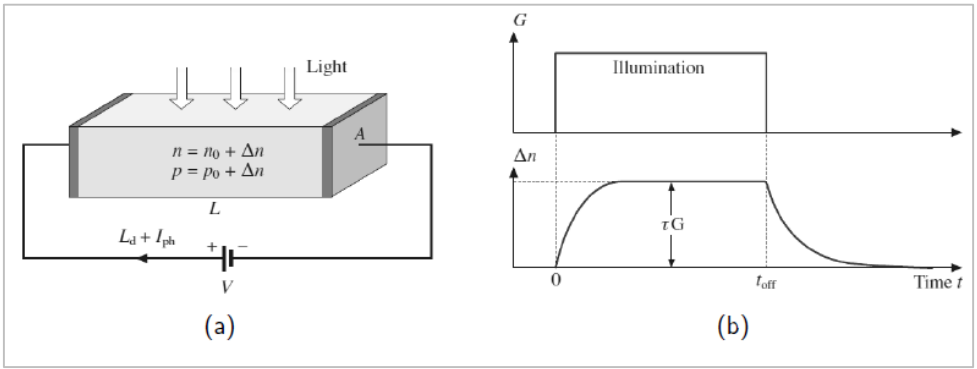

Fig. 75 (a) Basic arrangement for photoconductivity measurements, where V the applied voltage, L the sample length and A the cross-sectional area. I_d, n_0 and p_0 are the current and the carrier densities in the dark, and I_{ph}, Δn, Δp are the incremental values caused by the illumination. (b) Schematic time development of the excess carrier concentration Δn in response to a period of illumination.

5.2.1 General theory

For an *intrinsic* (i.e. undoped) semiconductor, the *intrinsic photoelectric effect* is the dominant mechanism that creates non-equilibrium carriers, i.e light absorption promotes electrons in the conduction band leaving behind holes in the valence band. On the other hand, in an *extrinsic* (i.e. doped) photoconductor, the excitation of shallow impurity levels is involved. The wavelength cut-off (i.e. the *PC edge*) for this simple case is given by:

$$\lambda_{edge} = \frac{hc}{E_g} \tag{40}$$

where E_g is the bandgap energy, h is the Planck constant, and c is the speed of light in a vacuum.

The conductivity σ_0 of non-illuminated intrinsic semiconductor device is given by [111]:

$$\sigma_0 = e(n_0\mu_n + p_0\mu_p) \tag{41}$$

where n_0, p_0, μ_n, and μ_p are respectively the equilibrium concentrations of free electrons and holes and their *mobilities*, while e is the elementary charge of the electron. In

general, when the material is illuminated with light of $\lambda < \lambda_{edge}$ (i.e. $h\nu > E_g$), non-equilibrium carriers are created at a concentration of:

$$\Delta n = \Delta p = \frac{\eta_{ext}\Phi\tau}{Ad} \tag{42}$$

where η_{ext} is the *external quantum efficiency*, defined as the probability that a photoelectron is produced when a photon hit the sample surface, Φ is the photon flux (number of photons per unit time), τ is the carrier lifetime, while A and d are the sample's active area and thickness respectively. The change in the conductivity can be written as:

$$\Delta\sigma = \sigma_{ph} = e(\mu_n\Delta n + \mu_p\Delta p) \tag{43}$$

Using (41) and (42), we can obtain the relative change in conductivity of the illuminated photoconductor:

$$\frac{\Delta\sigma}{\sigma} = \frac{e(\mu_n + \mu_p)\eta_{ext}\Phi\tau}{\sigma Ad} \tag{44}$$

For an extrinsic semiconductor, or when $\mu_n >> \mu_p$ (e.g. for most metal-oxides materials) the sum $\mu_n + \mu_p$ has to be replaced with the mobility of the available carrier (e.g. μ_n). The classic experimental setup is illustrated in Fig. 75-a, where L and A are the length and the cross-sectional area of the sample and the photocurrent is $\Delta I = I_{ph} = \sigma_{ph}AE$, and $E = V/L$ is the applied electrical field. Generally, a fraction of the photo-generated carriers becomes *trapped* at various defects (corresponding to deep energy levels within the band gap), such that not every part of Δn and Δp contributes equally to the photoconductivity in Eq. (43). The trapping effect on the photoconductivity can be accounted for using effective values for the mobilities μ_n and μ_p that are lower than the theoretical free-carrier mobility μ_0.

5.2.2 Photoconductivity in metal-oxides

In metal-oxide semiconductors, the general PC mechanism described in the previous paragraph holds as stated. However, due to the affinity to adsorption of O_2 on the surface in most of these materials, there is another mechanism that can take place, which is related to the trapping of carriers at the surface by the adsorbed molecules.

For some materials, most notably zinc oxide, it is known from a long time [112] that this process is the dominant one in determining the value and the rise/decay time of the photo-conductivity, as well as the value of the dark current of these samples.

The process is described in literature usually in the case of metal-oxide (e.g. ZnO) nano-wires (NW), due to the simple geometry of the nanostructures [113] [114].

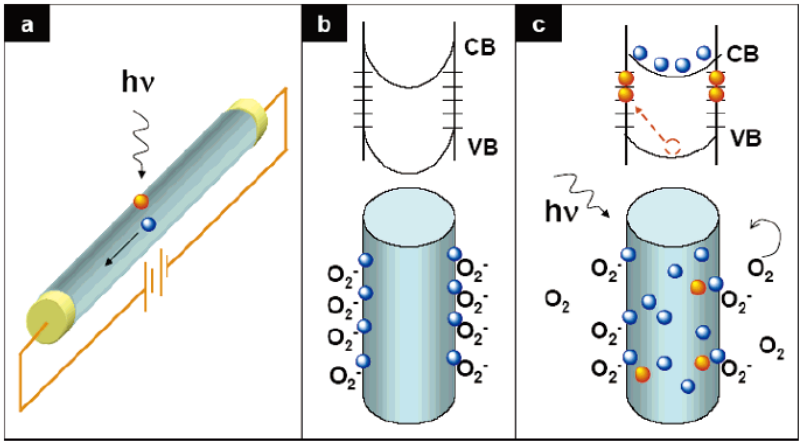

Fig. 76 Photoconduction in metal-oxides nano-wires: (a) Schematic of a NW with applied bias: upon illumination with photons at hν > E_g, electron-hole pairs are generated and holes are readily trapped at the surface. Under the applied electric field, the unpaired electrons are collected at the anode, which leads to the increase in conductivity. (b) Schematic of the energy band diagrams of a ZnO NW in the dark, indicating band-bending and surface trap states due to O_2 adsorption. The bottom drawing shows oxygen molecules absorbed at the NW surface that capture the free electrons present in the n-type semiconductor forming a low conductivity depletion layer near the surface. (c) Under light illumination, photo-generated holes migrate to the surface and become trapped, leaving behind unpaired electrons in the NW that contribute to the photocurrent. In ZnO NWs, the lifetime of the unpaired electrons is further increased by oxygen molecules desorption from the surface when holes neutralize the oxygen ions [71].

In the dark, O_2 molecules adsorb on the ZnO surface and capture the free electrons present in a n-type oxide semiconductor [$O_2(g) + e^- \rightarrow O_2^-(ad)$], and a low-conductivity depletion layer is formed near the surface (Fig. 76-b), that results in the reduction of the conduction channel. When the ZnO NW is illuminated by a UV-light with energy above the energy gap, electron-hole pairs are photo-generated [$h\nu \rightarrow e^- + h^+$], and holes migrate to the surface along the potential slope produced by band bending and discharge the absorbed oxygen ions (O_2^-) through *surface electron-hole recombination* [$h^+ + O_2^-(ad) \rightarrow O_2(g)$] (Fig. 76-c). Consequently, oxygen is *photo-desorbed* from the surface. The unpaired electrons are either collected at the anode or recombine with holes generated when oxygen molecules are reabsorbed and ionized at the surface. Thus, the increase in conductivity due to light absorption has two sources: the *unpaired*

electrons that increase the overall density of carriers, and the geometric effect due to the *widening of the neutral channel* in the core of the NW, itself caused by the reduction of the surface depletion layer thickness.

The hole trapping mechanism through oxygen desorption in ZnO NWs augments the high density of trap states (usually found in NWs) due to the dangling bonds at the surface, and thus greatly increases the NW photoconductivity [71].

This type of conduction mechanism has important consequences:

1. The *dark current* is sensitive to the partial pressure of oxygen, but also to different types of gases (H_2. H_2S, NO_2, CH_3CH_2OH, etc.). This is due to competitive adsorption of these gases with oxygen, that change the conductivity as a consequence.
2. Characteristic rise and decay time constants of the PC are usually much longer than the carrier lifetime τ that appears in Eq. (42). For classic photo-conductors $\tau < 10$ ms, while in metal oxides like ZnO PC rise and decay times can be longer than several hours; this is due to the fact that the mechanism follows the kinetics of adsorption and desorption of species at the surface instead of carrier recombination inside the material.

If the sample is placed in a *vacuum*, the dark current as well as the photo-current should attain a considerably higher value than when the sample is measured in an oxygen-rich atmosphere. This is due to the fact that in a not perfect, but sufficiently good), vacuum, available O_2 molecules are considerably less in number, thus the surface depletion layer is accordingly much thinner, and the conductivity is higher.

5.2.3 Photocurrent measurement

The PC measurement equipment is shown in Fig. 77: the sample is held in an air tight chamber in which a vacuum of about 10^{-5} mbar can be created, using a primary rotary pump and a secondary oil diffusion pump. The light source is a xenon-filled arc lamp with a power output of 300 W, and light can be rendered monochromatic by means of a diffraction grating monochromator, that can operate between 200 and 1300 nm. The voltage is applied to the sample through a *Keitley 2400 source-meter* ($V_{max} = \pm 210$ V); the same instrument can be used to measure the current inside the sample to a sensitivity of 10 pA.

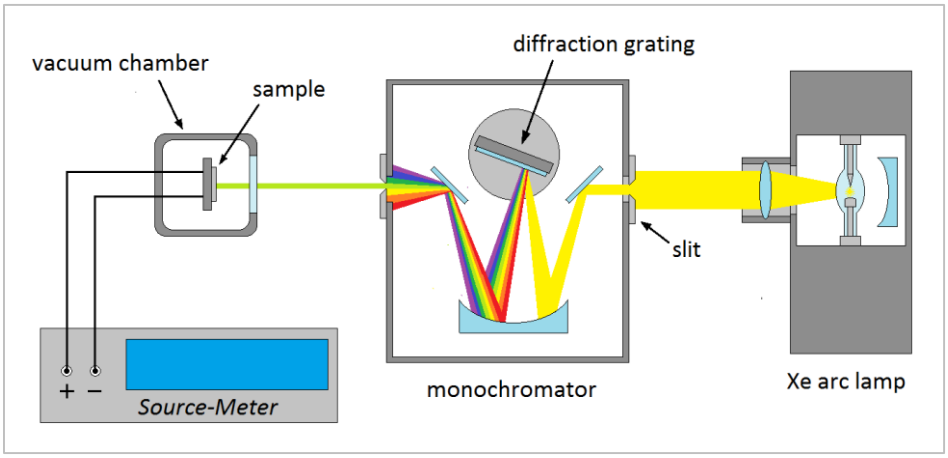

Fig. 77 Diagram of the equipment used to acquire the photocurrent measurements. The light source is a 300 W xenon filled arc lamp, and light is monochromatized using a diffraction grating monochromator. To apply a bias to the sample and at the same time measure the photocurrent, a Keithley 2400 source-meter is used.

For standard semiconductor materials, the usual technique to acquire the photocurrent spectrum of the sample involve the use of a *light chopper*, operating at frequencies between 10 and 10^4 Hz, coupled with a *lock-in amplifier*. With this set-up, the light chopper induce a time-varying photo-current signal in the sample with a pre-determined frequency ω_{ch}; the lock-in amplifier then picks up only signals coming from the sample that are in phase with the chopper frequency, discarding everything else. In this way, there is a dramatic increase in the signal-to-noise ratio and every source of light and/or electric noise that is not in phase with ω_{ch} is cut off.

This method, however, can only be used if the photocurrent rise/decay time is shorter than a fraction of a second, and cannot be used for the materials that are the object of this thesis, due to the fact that the PC is much slower than that, at least at room temperature.

To acquire the PC spectrum for metal-oxides semiconductors, that show a relatively slow PC rise and decay, the method of choice is to illuminate the sample with light of a single wavelength λ, and to measure the photocurrent after a pre-set time interval ($\Delta t \approx 1000$ s) of constant illumination. $I(t_{on}+\Delta t,\lambda)$ represent the value attained by the photo-current after this time: from this is subtracted the value $I(t_{on},\lambda)$ of the current at the time immediately before the illumination, so that $I_{PC}(\lambda) = I(t_{on}+\Delta t,\lambda) - I(t_{on},\lambda)$. This is done to compensate for the *persistent photo-current* (PPC) that is usually left from previous measurements (see Fig. 78). Normally in fact, the PC in the dark before illumination is not the equilibrium value, due to long-term persistent PC effects that are function of the previous history of the sample.

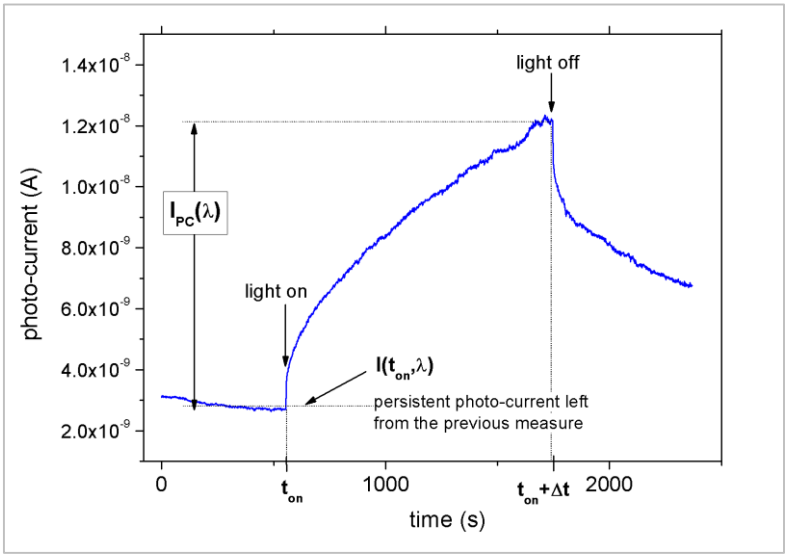

Fig. 78 Typical form of the PC vs. time for a sample of metal-oxide. Monochromatic light of wavelength λ is turned on at the instant t_{on}, and is turned off at $t_{on}+\Delta t$ (Δt=1000 s).

5.3 X-ray diffraction

X-rays are a type of electromagnetic radiation with wavelengths on the order of 1 Å (10^{-10} m), which is comparable with the size of the spacing between atoms in solids. When X-rays interact with a crystalline substance, one gets a diffraction pattern.

In a crystalline solid, the atoms do not distribute randomly but are arranged in space in a regular three-dimensional way, this arrangement being the crystal lattice. These lattices are composed of a series of parallel planes of atoms, with spacing distance *d*.

Usually, the atoms are distributed in a number of directions in a crystal, so that many planes with different orientations exist, each of them having its own specific *d* spacing.

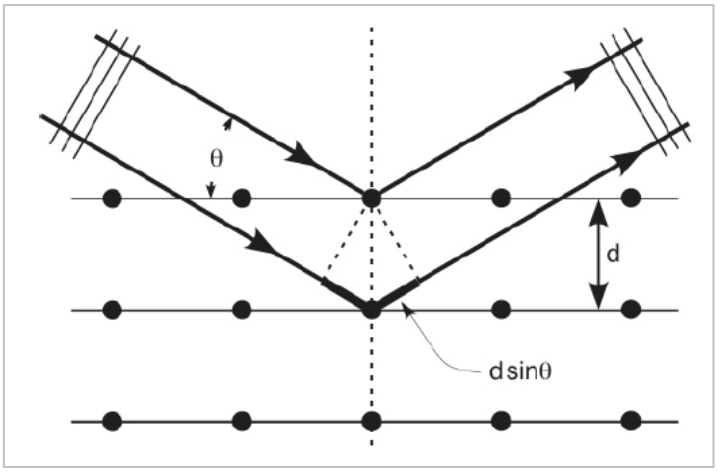

Fig. 79 Bragg diffraction from a crystal lattice of spacing d between planes. The diffracted beam which exit the crystal is due to constructive interference between beams reflected from all the parallel planes of the crystal.

Fig. 79 illustrates the reflection of X-rays from two planes of atoms in a crystalline solid. When a monochromatic X-ray beam with wavelength λ is projected onto a crystal lattice at an angle ϑ, diffraction occurs only when the distance travelled by the rays reflected from successive planes differs by a complete number n of wavelengths, due to interference between the beams reflected from all the parallel planes; this leads to the *Bragg's law of diffraction*:

$$n\lambda = 2dsin\theta \qquad (45)$$

where n is an integer: n = 1,2,3…. (usually is equal to 1, corresponding to the fundamental diffraction), λ is wavelength in angstroms (1.54 Å for the *copper* K_α wavelength, the most used), d is interatomic spacing in angstroms, and ϑ is the diffraction angle in degrees. The set of planes of spacing d is identified by a set of Miller indices, which are the integer coefficients of the reciprocal lattice vector $\boldsymbol{g_{hkl}}$ relative to that plane, so that:

$$d = \frac{2\pi}{|\boldsymbol{g_{hkl}}|} \qquad (46)$$

By varying the angle ϑ, the Bragg's law conditions are satisfied by different d-spacings in polycrystalline materials. Plotting the angular positions and intensities of the resultant diffracted peaks of radiation produces a pattern, which is characteristic of the sample.

Based on the principle of X-ray diffraction, we can obtain a wealth of structural and physical information about the material. XRD can be used for two main applications: the "fingerprint" characterization of crystalline materials and the determination of their structure. Each crystalline solid has its unique characteristic X-ray diffraction pattern which may be used as a fingerprint for its identification, using standards from diffraction

pattern databases. On the other hand, once the material has been identified, XRD may be used to determine its structure, i.e. how the atoms pack together in the crystalline state and what the interatomic distance and angle are etc.

The position of a diffracted peak gives information about the unit cell parameters whereas the intensity of a diffracted peak gives information about the atomic positions. The intensity of a diffracted X-ray beam is given as:

$$I_{hkl} = cjPLAF_{hkl}^2 \quad (47)$$

where *j* is the *multiplicity* (symmetry equivalent reflections), *P* is the *polarisation factor* (polarisation of an X-ray photon can change as a result of scattering/diffraction), *L* is the *Lorentz factor* (geometric correction), *A* is the *X-ray absorption* (X-rays are absorbed as they pass through materials) and *F* is the *structure factor* (mathematical treatment of how atoms scatter light) of the (h,k,l) reflection. If the structure factors F_{hkl} are known for a full set of reflections then the electron density, at any position xyz in the unit cell, can be calculated corresponding to atomic positions. It is possible to measure F_{hkl}^2 and consequently $|F_{hkl}|$, but not its sign. Computer programmes are often required to solve the structure, but more importantly, a combination of X-ray and neutron diffraction is desirable.

As the XRD pattern depend on the arrangement of atoms inside a material, other properties of the sample can be analysed from its study, such as the degree of crystallinity, or the residual strain in an epitaxial film.

5.4 Scanning electron microscopy

The scanning electron microscope (SEM) uses a high energy electron beam focussed on a sample to produce high resolution images of the sample surface (Fig. 80). Bombardment of the sample surface with high energy electrons that are accelerated by a voltage in the kV range, results in the formation of *secondary electrons* and *backscattered electrons*, as well as other emissions, such as characteristic X-rays (used in *X-Ray micro-analysis*) and light (*cathodoluminescence*).

Secondary electrons are ejected from the sample as a result of multiple collisions initiated by the incident high energy electrons bombarding the sample [115]. Backscattered electrons are electrons that have undergone elastic or inelastic scattering with the sample surface. The kinetic energy of backscattered electrons is higher than that of secondary electrons, and the intensity of backscattered electrons depends greatly on the atomic number of the sample's material.

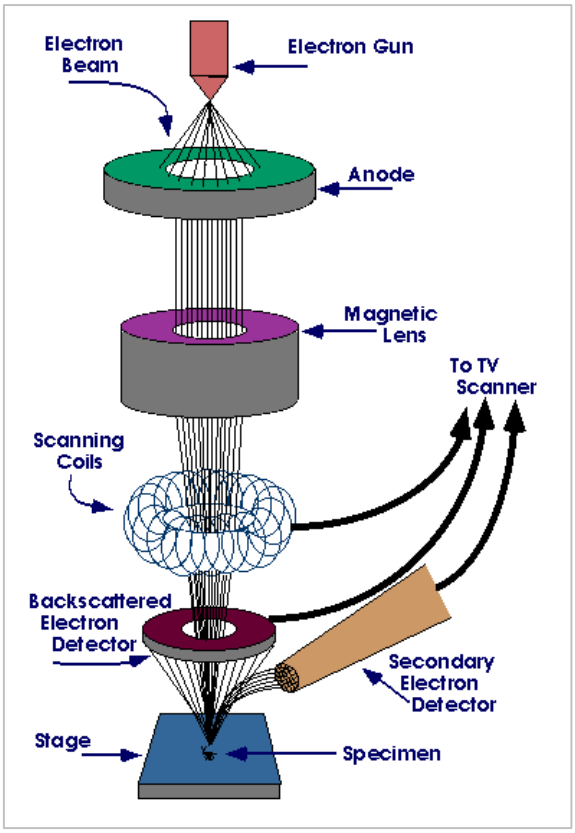

Fig. 80 Simple schematics of a scanning electron microscope. In this particular case, magnetic lenses (electrified coils) are used to control the electron beam; alternatively, electrostatic lenses, or a combination of the two, can be used.

Imaging of the surface of sample can be accomplished using secondary electrons trough *secondary electrons imaging* (SEI). Through the use of electro-magnetic lenses, the electron beam is scanned on the surface of the sample in a rasterized fashion, all the while detecting emitted secondary electrons: in this way the SEM can produce very high-resolution images of the sample surface, revealing details less than 1 nm in size. Due to the very narrow electron beam, SEM micrographs have a large depth of field yielding a characteristic three-dimensional appearance, useful for understanding the surface structure of a sample. A wide range of magnifications is possible, from about 10 times (about equivalent to that of a powerful hand-lens) to more than 500.000 times, about 250 times the magnification limit of the best light microscopes.

Scanning electron microscopy was used to image the surface of vapour-grown Ga_2O_3 thin films, as well as ZnO nanostructures, in order to determine the morphological properties and crystal quality of the samples.

5.5 Cathodoluminescence spectroscopy

Cathodoluminescence (CL) is an optical analysis technique in which high energy electrons (in the keV range) impact on a luminescent material and cause the emission of photons that have much lower energy than the initial electrons (usually in the VIS-UV range). Cathodoluminescence is the inverse of the photoelectric effect, in which electron emission is induced by irradiation with photons.

CL instruments are really electron microscopes (Fig. 80), of the scanning or transmission type, in which a focused beam of electrons impinges on a sample, inducing it to emit light that is collected by an optical system, such as an elliptical mirror. From there, a fibre optic will transfer the light out of the microscope where it is separated into its component wavelengths by a monochromator and is then detected with an appropriate detector. The primary advantage to the electron microscope based technique is the ability to resolve features down to 1 nanometer [116] size and the ability to image the precise region of measurement. Moreover, the optical properties of an object can be correlated to structural properties observed with the electron microscope.

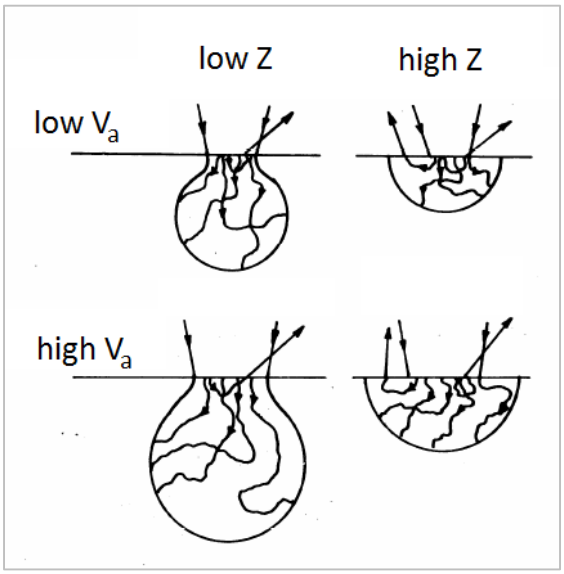

Fig. 81 Interaction volume for different accelerating voltage (V_a) in a low and a high atomic number (Z) materials.

CL emission occurs because the impact of high-energy electrons onto a semiconductor will result in the promotion of electrons from the valence band of the sample material into the conduction band, leaving behind a hole. Recombination of the electron-hole couple may result in the emission of a photon with $hv \approx E_g$. Other than band-to-band

transitions, the electron beam can promote defect transitions, i.e. transitions from states inside the bend gap, such that the energy of the photon, and the probability that a photon and not a phonon will be emitted, depends on the material, its purity, and its defect state.

The CL photons are emitted from a nearly spherical region under the surface of the material known as the interaction volume. The shape and volume of this region depend chiefly on the accelerating voltage of the electron beam as well as the atomic number of the material (see Fig. 81).

Using theoretical calculations or computer (usually Monte Carlo) simulations, it is possible to predict the characteristics of the interaction volume for a specific material and electron energy; in this way, it is possible to deduce the thickness inside the sample from which the signal arise.

The CL technique is based on the observation of photon emission due to radiative recombination of carriers within the sample; as such, the technique is most sensitive in the case of direct band gap semiconductors. However, in some cases, radiative band-to-band recombination can be forbidden, and does not appear as an emission in the CL spectrum. Unfortunately, this is exactly the case for the Ga_2O_3 samples analysed in this thesis; however, defect related emissions appear in the CL spectrum and can be studied as such.

6 Bibliography

[1] T. Yu, Y. Zhu, X. Xiaojing , K. S. Yeong, Z. Shen, P. Chen, C. T. Lim, J. T.-L. Thong and C. H. Sow, «Substrate-Friendly Synthesis of Metal Oxide Nanostructures Using a Hotplate» *small,* vol. 2, n. 1, p. 80 – 84, 2006.

[2] A. B. Djurisic, A. M. C. Ng and X. Y. Chen, «ZnO nanostructures for optoelectronics: Material properties and device applications» *Progress in Quantum Electronics,* vol. 34, pp. 191-259, 2010.

[3] T. Zhai, X. Fang, M. Liao, X. Xu, H. Zeng, B. Yoshio and G. Dmitri, «A Comprehensive Review of One-Dimensional Metal-Oxide Photodetectors» *Sensors,* vol. 9, pp. 6504-6529, 2009.

[4] L. Sang, M. Liao and M. Sumiya, «A Comprehensive Review of Semiconductor Ultraviolet Photodetectors: From Thin Film to One-Dimensional Nanostructures» *Sensors,* vol. 13, pp. 10482-10518, 2013.

[5] U. Ozgur, D. Hofstetter and H. Morkoc, «ZnO Devices and Applications: A Review of Current Status and Future Prospects» *Proceedings of the IEEE,* vol. 98, n. 7, pp. 1255-1268, 2010.

[6] H. Hosono, «Recent progress in transparent oxide semiconductors: Materials and device application» *Thin Solid Films,* vol. 515, p. 6000–6014, 2007.

[7] P. D. C. King and T. D. Veal, «Conductivity in transparent oxide semiconductors» *J. Phys.: Condens. Matter,* vol. 23, pp. 334214-334231, 2011.

[8] M. Higashiwaki, K. Sasaki, A. Kuramata, T. Masui and S. Yamakoshi, «Gallium oxide (Ga2O3) metal-semiconductor field-effect transistors on single-crystal β-Ga2O3 (010) substrates» *APPLIED PHYSICS LETTERS,* vol. 100, p. 013504, 2012.

[9] Y. F. Sun, S. B. Liu, F. L. Meng, J. Y. Liu, Z. Jin, L. T. Kong and J. H. Liu, "Metal Oxide Nanostructures and Their Gas Sensing Properties: A Review" *Sensors,* vol. 12, pp. 2610-2631, 2012.

[10] C. Wang, L. Yin, L. Zhang, D. Xiang and R. Gao, «Metal Oxide Gas Sensors: Sensitivity and Influencing Factors» *Sensors,* vol. 10, pp. 2088-2106, 2010.

[11] K. Nomura, H. Ohta, A. Takagi, T. Kamiya, M. Hirano and H. Hosono, «Room-temperature fabrication of transparent flexible thin-film transistors using amorphous oxide semiconductors» *NATURE,* vol. 432, pp. 488-492, 2004.

[12] S. R. Thomas, P. Pattanasattayavong and T. D. Anthopoulos, «Solution-processable metal oxide semiconductors for thin-film transistor applications» *Chem. Soc. Rev.,* vol. 42, pp. 6910-6923, 2013.

[13] J. H. W. De Wit, G. Van Unen and M. Lahey, «Electron concentration and mobility in In2O3» *J. Phys. Chem. Solids,* vol. 38, p. 819–824, 1977.

[14] A. Togo, F. Oba, I. Tanaka and K. Tatsumi, «First-principles calculations of native defects in tin monoxide» *Phys. Rev. B,* vol. 74, p. 195128, 2006.

[15] S. J. Jokela and M. D. McCluskey, «Structure and stability of O−H donors in ZnO from high-pressure and infrared spectroscopy» *Phys. Rev. B,* vol. 72, p. 113201, 2005.

[16] A. Janotti and C. G. Van de Walle, «Fundamentals of zinc oxide as a semiconductor,» *Rep. Prog. Phys. ,* vol. 72, p. 126501, 2009.

[17] Y. J. Li, T. C. Kaspar, T. C. Droubay, A. G. Joly, P. Nachimuthu, Z. Zhu, V. Shutthanandan and S. A. Chambers, «A study of H and D doped ZnO epitaxial films grown by pulsed laser deposition» *J. Appl. Phys.,* vol. 104, p. 053711, 2008.

[18] A. Janotti and C. G. Van de Walle, «Hydrogen multicentre bonds» *Nature Materials,* vol. 6, pp. 44 - 47, 2007.

[19] S. Lany and A. Zunger, «Dopability, Intrinsic Conductivity, and Nonstoichiometry of Transparent Conducting Oxides» *Phys. Rev. Lett.,* vol. 98, p. 045501, 2007.

[20] M. D. McCluskey and S. J. Jokela, «Defects in ZnO» *J. Appl. Phys.,* vol. 106, p. 071101, 2009.

[21] Y. Natsume, H. Sakata, T. Hirayama and H. Yanagida, «Low-temperature conductivity of ZnO films prepared by chemical vapor deposition» *J. Appl. Phys.,* vol. 72, p. 4203, 1992.

[22] R. Kumara and N. Khareb, «Temperature dependence of conduction mechanism of ZnO and Co-doped ZnO thin films» *Thin Solid Films,* vol. 516, n. 6, p. 1302–1307, 2008.

[23] D. Y. Guo, Z. P. Wu, Y. H. An, X. C. Guo, X. L. Chu, C. L. Sun, L. H. Li, P. G. Li and W. H. Tang, «Oxygen vacancy tuned Ohmic-Schottky conversion for enhanced performance in β-Ga2O3 solar-blind ultraviolet photodetectors» *APPLIED PHYSICS LETTERS,* vol. 105, p. 023507, 2014.

[24] W. Y. Weng, T. J. Hsueh, S. J. Chang, G. J. Huang and S. C. Hung, «Growth of Ga2O3 nanowires and the fabrication of solar-blind photodetector» *IEEE Trans. Nanotechnol.,* vol. 10, p. 1047–1052, 2011.

[25] L. Li, E. Auer, M. Liao, X. Fang, T. Zhai, U. Gautam, A. Lugstein, Y. Koide, Y. Bando and D. Golberg, «Deep-ultraviolet solar-blind photoconductivity of individual gallium oxide nanobelts» *Nanoscale,* vol. 3, p. 1120–1126, 2011.

[26] H. Kind, H. Q. Yan, B. Messer and P. D. Yang, «Nanowire ultraviolet photodetectors and optical switches» *Adv. Mater.,* vol. 14, p. 158–160, 2002.

[27] A. J. Gimenez, J. M. Yanez-Limon and J. M. Seminario, «ZnO-Paper Based Photoconductive UV Sensor» *Journal of Physical Chemistry C,* vol. 115, pp. 282-287, 2011.

[28] S. Rackauskas, K. Mustonen, T. Jarvinen, M. Mattila, O. Klimova, H. Jiang, O. Tolochko, H. Lipsanen, E. I. Kauppinen and A. G. Nasibulin, «Synthesis of ZnO tetrapods for flexible and transparent UV sensors» *Nanotechnology,* vol. 23, p. 095502 (7pp), 2012.

[29] J. A. Anta, «Electron transport in nanostructured metaloxide semiconductors» *Current Opinion in Colloid & Interface Science,* vol. 17, p. 124–131, 2012.

[30] E. Comini, G. Faglia and G. Sberveglieri, «Stable and highly sensitive gas sensors based on semiconducting oxide nanobelts» *APPLIED PHYSICS LETTERS,* vol. 81, n. 10, pp. 1869-1871, 2002 .

[31] D. Calestani, M. Zha, R. Mosca, A. Zappettini, M. C. Carotta, V. Di Natale and L. Zanotti, «Growth of ZnO tetrapods for nanostructure-based gas sensors» *Sensors and Actuators B: Chemical,* vol. 144, p. 472–478, 2010.

[32] M. Higashiwaki and S. Hirota, «First Demonstration of Gallium Oxide (Ga2O3) Metal-Oxide-Semiconductor Field-Effect Transistors (MOSFETs)» *NICT press release,* 2013.

[33] J. B. Varley, J. R. Weber, A. Janotti and C. G. Van de Walle, «Oxygen vacancies and donor impurities in β-Ga2O3» *Applied Physics Letters,* vol. 97, p. 142106, 2010.

[34] M. Orita, H. Ohta, M. Hirano and H. Hosono, «Deep-ultraviolet transparent conductive β-Ga2O3 thin films» *Applied Physics Letters,* vol. 77, n. 25, 2000.

[35] A. A. Balandin, Noise and Fluctuations Control in Electronic Devices, American Scientific Publishers, 2002.

[36] M. Bartic, C. I. Baban, H. Suzuki, M. Ogita and M. Isai, «Beta-Gallium Oxide as Oxygen Gas Sensors at a High Temperature» *J. Am. Ceram. Soc.,* vol. 90, n. 9, p. 2879–2884, 2007.

[37] K. Shimamura, E. G. Villora, K. Domen, K. Yui, K. Aoki and N. Ichinose, «Epitaxial Growth of GaN on (1 0 0) β-Ga2O3 Substrates by Metalorganic Vapor Phase Epitaxy» *Japanese Journal of Applied Physics,* vol. 44, n. 1, p. L 7–L 8, 2005.

[38] H. Y. Playford, A. C. Hannon, E. R. Barney and R. I. Walton, «Structures of Uncharacterised Polymorphs of Gallium Oxide from Total Neutron Diffraction» *Chem. Eur. J.,* n. 19, p. 2803 – 2813, 2013.

[39] R. Roy, V. G. Hill and E. F. Osborn, «Polymorphism of Ga2O3 and the System Ga2O3-H2O» *J. Am. Chem. Soc.,* vol. 74, n. 3, p. 719–722, 1952.

[40] Y. Oshima, E. G. Víllora, Y. Matsushita, S. Yamamoto and K. Shimamura, «Epitaxial growth of phase-pure ε-Ga2O3 by halide vapor phase epitaxy» *Journal of Applied Physics,* vol. 118, p. 085301, 2015.

[41] K. L. Choy, «Chemical vapour deposition of coatings» *Progress in Materials Science,* vol. 48, n. 2, p. 57–170, 2003.

[42] T. T. Kodas and M. J. Hampden-Smith, The Chemistry of Metal CVD, VCH, 2008.

[43] M. Ohring, The Materials Science of Thin Films, Academic Press, 1992.

[44] J. E. Ayers, Heteroepitaxy of Semiconductors, CRC Press , 2007.

[45] R. L. Puurunen, «Surface chemistry of atomic layer deposition: A case study for the trimethylaluminum/water process» *J. Appl. Phys.,* vol. 97, p. 121301, 2005.

[46] S. Geller, «Crystal Structure of β-Ga2O3» *The Journal of Chemical Physics,* vol. 33, p. 676, 1960.

[47] T. Oshima, T. Okuno and S. Fujita, «Ga2O3 Thin Film Growth on c-Plane Sapphire Substrates by Molecular Beam Epitaxy for Deep-Ultraviolet Photodetectors» *Japanese Journal of Applied Physics,* vol. 46, n. 11, p. 7217–7220, 2007.

[48] S. Nakagomi and Y. Kokubun, «Crystal orientation of b-Ga2O3 thin films formed on c-plane and a-plane sapphire substrate» *Journal of Crystal Growth,* vol. 349, p. 12–18, 2012.

[49] J. Tauc, R. Grigorovici and A. Vancu, «Optical Properties and Electronic Structure of Amorphous Germanium» *physica status solidi (b),* vol. 15, n. 2, p. 627–637, 1966.

[50] E. A. Davis and N. F. Mott, «Conduction in non-crystalline systems V. Conductivity, optical absorption and photoconductivity in amorphous semiconductors» *Philosophical Magazine,* vol. 22, n. 179, 1970.

[51] H. He, R. Orlando, M. A. Blanco and R. Pandey, «First-principles study of the structural, electronic, and optical properties of Ga2O3 in its monoclinic and hexagonal phases» *PHYSICAL REVIEW B,* vol. 74, p. 195123, 2006.

[52] M. Beaudoin, M. Meunier e C. J. Arsenault, «Blueshift of the optical band gap: Implications for the quantum confinement effect in a-Si:H/a-SiNx:H multilayers,» *Phys. Rev. B , ,* vol. 47, p. 2197, 1993.

[53] E. G. Villora, M. Yamaga, T. Inoue, S. Yabasi, Y. Masui, T. Sugawara and T. Fukuda, «Optical Spectroscopy Study on β-Ga2O3» *Jpn. J. Appl. Phys.,* vol. 41, p. L 622–L 625, 2002.

[54] N. Ueda, H. Hosono, R. Waseda and H. Kawazoe, «Anisotropy of electrical and optical properties in β-Ga2O3 single crystals» *Applied Physics Letters,* vol. 71, n. 7, pp. 933-935, 1997.

[55] F. Fabbri, M. J. Smith, D. Recht, M. J. Aziz, S. Gradecak and G. Salviati, «Depth-resolved cathodoluminescence spectroscopy of silicon supersaturated with sulfur» *APPLIED PHYSICS LETTERS,* vol. 102, p. 031909, 2013.

[56] G. Bellocchi, F. Fabbri, M. Miritello, F. Iacona e G. Franzò, «Multicolor Depth-Resolved Cathodoluminescence from Eu-Doped SiOC Thin Films,» *ACS Appl. Mater. Interfaces,* vol. 7, n. 33, p. 18201–18205, 2015.

[57] L. Binet and D. Gourier, «Optical evidence of intrinsic quantum wells in the transparent conducting oxide β-Ga2O3» *APPLIED PHYSICS LETTERS ,* vol. 77, n. 8, pp. 1138-1140, 2000.

[58] V. N. Sigaev, N. V. Golubev, E. S. Ignateva, A. Paleari and R. Lorenzi, «Light-emitting Ga-oxide nanocrystals in glass: a new paradigm for low-cost and robust UV-tovisible solar-blind converters and UV emitters» *Nanoscale,* vol. 6, p. 1763–1774, 2014.

[59] D. C. Look, «Recent advances in ZnO materials and devices» *Materials Science and Engineering B,* vol. 80, p. 383, 2001.

[60] U. Ozgur, Y. I. Alivov, C. Liu, A. Teke, M. A. Reshchikov, S. Dogan, V. Avrutin, S. J. Cho and H. Morkoc, «A comprehensive review of ZnO materials and devices» *J. Appl. Phys.,* vol. 98, p. 041301, 2005.

[61] N. H. Nickel and E. Terukov, Zinc Oxide—A Material for Micro- and Optoelectronic Applications, Springer, 2005.

[62] M. C. Newton and P. A. Warburton, «ZnO tetrapod nanocrystals» *Materials Today,* vol. 10, n. 5, pp. 50-54, 2007.

[63] D. J. Milliron, S. M. Hughes, Y. Cui, L. Manna, J. Li, L. W. Wang and P. A. Alivisatos, «Colloidal nanocrystal heterostructures with linear and branched topology» *Nature,* vol. 430, pp. 190-195, 2004.

[64] M. C. Newton, S. Firth, T. Matsuura and P. A. Warburton, «Synthesis and characterisation of zinc oxide tetrapod nanocrystals» *Journal of Physics: Conference Series,* vol. 26, p. 251–255, 2006.

[65] Y. Dai, Y. Zhang and Z. L. Wang, «The octa-twin tetraleg ZnO nanostructures» *Solid State Communications,* vol. 126, p. 629–633, 2003.

[66] Z. Chen, Z. Shan, M. S. Cao, L. Lu e S. X. Mao, «Zinc oxide nanotetrapods,» *Nanotechnology,* vol. 15, n. 3, 2004 .

[67] A. Janotti and C. G. Van de Walle, «Oxygen vacancies in ZnO» *Appl. Phys. Lett.,* vol. 87, p. 122102, 2005.

[68] M. E. Franke, T. J. Koplin and U. Simon, «Metal and Metal Oxide Nanoparticles in Chemiresistors: Does the Nanoscale Matter?» *Small,* vol. 2, pp. 36-50, 2006.

[69] M. Kaur, S. K. Gupta, C. A. Betty, V. Saxena, V. R. Katti, S. C. Gadkari and J. V. Yakhmi, «Detection of reducing gases by SnO2 thin films: An impedance spectroscopy study» *Sens. Actuat. B,* vol. 107, pp. 360-365, 2005.

[70] C. N. Xu, J. Tamaki, N. Miura and N. Yamazoe, «Grain-size effects on gas sensitivity of porous SnO2-based elements» *Sens. Actuat. B,* vol. 3, pp. 147-155, 1991.

[71] C. Soci, A. Zhang, B. Xiang, S. A. Dayeh, D. P. R. Aplin, J. Park and X. Y. Bao, «ZnO Nanowire UV Photodetectors with High Internal Gain» *NANO LETTERS,* vol. 7, n. 4, pp. 1003-1009, 2007.

[72] J. C. Moore and C. V. Thompson, «A Phenomenological Model for the Photocurrent Transient Relaxation Observed in ZnO-Based Photodetector Devices» *Sensors,* vol. 13, pp. 9921-9940, 2013.

[73] J. Bao, I. Shalish, Z. Su, R. Gurwitz, F. Capasso, X. Wang and Z. Ren, «Photoinduced oxygen release and persistent photoconductivity in ZnO nanowires» *Nanoscale Research Letters,* vol. 6, p. 404, 2011.

[74] A. Bera and D. Basak, «Role of defects in the anomalous photoconductivity in ZnO nanowires» *Applied Physics Letters,* vol. 94, p. 163119, 2009.

[75] Y. Li, F. Della Valle, M. Simonnet, I. Yamada and J. J. Delaunay, «High-performance UV detector made of ultra-long ZnO bridging nanowires» *Nanotechnology,* vol. 20, p. 045501 , 2009.

[76] J. Reemts and A. Kittel, «Persistent photoconductivity in highly porous ZnO films» *Journal of Applied Physics,* vol. 101, p. 013709, 2007.

[77] J. J. Wu and S. C. Liu, «Low-Temperature Growth of Well-Aligned ZnO Nanorods by Chemical Vapor Deposition» *Adv. Mater.,* vol. 14, pp. 215-218, 2002.

[78] B. P. Zhang, K. Wakatsuki, N. T. Binh, Y. Segawa and N. Usami, «Low-temperature growth of ZnO nanostructure networks» *J. Appl. Phys.,* vol. 96, p. 340, 2004.

[79] M. Zha, D. Calestani, A. Zappettini, R. Mosca, M. Mazzera, L. Lazzarini and L. Zanotti, «Large-area self-catalysed and selective growth of ZnO nanowires,» *Nanotechnology,* vol. 19, p. 325603, 2008.

[80] L. Zanotti, D. Calestani, M. Villani, M. Zha, A. Zappettini and C. Paorici, «Vapour-phase growth, purification and large-area deposition of ZnO tetrapod nanostructures» *Crystal Research and Technology,* vol. 45, n. 6, p. 667 – 671, 2010.

[81] A. B. Djurisic and Y. H. Leung, «Optical Properties of ZnO Nanostructures» *Small,* vol. 2, n. 8-9, p. 944 – 961, 2006.

[82] A. B. Djurisic, W. C. H. Choy, V. A. L. Roy, Y. H. Leung, C. Y. Kwong, K. W. Cheah, T. K. G. Rao, W. K. Chan, H. F. Lui and C. Surya, «Photoluminescence and electron paramagnetic resonance of ZnO tetrapod structures» *Advanced Functional Materials,* vol. 14, n. 9, pp. 856-864, 2004.

[83] H. T. Ng, B. Chen, J. Li, J. Han, M. Meyyappan, J. Wu, X. Li and E. E. Haller, «Optical properties of single-crystalline ZnO nanowires on m-sapphire» *Appl. Phys. Lett.,* vol. 82, p. 2023, 2003.

[84] Z. Chen, N. Wu, Z. Shan, M. Zhao, S. Li, C. B. Jiang, M. K. Chyua and S. X. Mao, «Effect of N2 flow rate on morphology and structure of ZnO nanocrystals synthesized via vapor deposition» *Scripta Materialia,* vol. 52, n. 1, p. 63–67, 2005.

[85] Q. Yang, K. Tang, J. Zuo and Y. Qian, «Synthesis and luminescent property of single-crystal ZnO nanobelts by a simple low temperature evaporation route» *Applied Physics A,* vol. 79, n. 8, pp. 1847-1851, 2004.

[86] B. Lin, Z. Fu and Y. Jia, «Green luminescent center in undoped zinc oxide films deposited on silicon substrates» *Appl. Phys. Lett.,* vol. 79, p. 943, 2001.

[87] X. Liu, X. Wu, H. Cao and R. P. H. Chang, «Growth mechanism and properties of ZnO nanorods synthesized by plasma-enhanced chemical vapor deposition» *J. Appl. Phys.,* vol. 95, p. 3141, 2004.

[88] N. Y. Garces, L. Wang, L. Bai, N. C. Giles, L. E. Halliburton and G. Cantwell, «Role of copper in the green luminescence from ZnO crystals» *Appl. Phys. Lett.,* vol. 81, p. 622, 2002.

[89] P. Kubelka and F. Munk, «An Article on Optics of Paint Layers» *Z. Tech. Phys.,* vol. 12, p. 593, 1931.

[90] A. Escobedo Morales, E. Sanchez Mora and U. Pal, «Use of diffuse reflectance spectroscopy for optical characterization of un-supported nanostructures» *REVISTA MEXICANA DE FISICA S,* vol. 53, n. 5, p. 18–22, 2006.

[91] J. Tauc, Optical Properties of Solids, North-Holland, 1972.

[92] J. Wang, Z. Wang, B. Huang, Y. Ma, Y. Liu, X. Qin, X. Zhang and Y. Dai, «Oxygen Vacancy Induced Band-Gap Narrowing and Enhanced Visible Light Photocatalytic Activity of ZnO» *ACS Appl. Mater. Interfaces,* vol. 4, p. 4024−4030, 2012.

[93] Y. Hu, J. Zhou, P. H. Yeh, Z. Li, T. Y. Wei and Z. L. Wang, «Supersensitive, Fast-Response Nanowire Sensors by Using Schottky Contacts» *Adv. Mater.,* vol. 22, p. 3327–3332, 2010.

[94] Y. Takahashi, M. Kanamori, A. Kondoh, H. Minoura and Y. Ohya, «Photoconductivity of Ultrathin Zinc Oxide Films» *Jpn. J. Appl. Phys.,* vol. 33, pp. 6611-6615, 1994.

[95] O. Lupan, L. Chow and G. Chai, «A single ZnO tetrapod-based sensor» *Sensors and Actuators B,* vol. 141, p. 511–517, 2009.

[96] M. C. Carotta, A. Cervia, V. di Natale, S. Gherardi, A. Giberti, V. Guidi, D. Puzzovio, B. Vendemiati, G. Martinelli, M. Sacerdoti, D. Calestani, A. Zappettini, M. Zha and L. Zanotti, «ZnO gas sensors: A comparison between nanoparticles and nanotetrapods-based thick films» *Sensors and Actuators B: Chemical,* vol. 137, p. 164–169, 2009.

[97] G. Lutz, Semiconductor Radiation Detectors, Springer, 2007.

[98] J. Isberg, M. Gabrysch, A. Tajani and D. J. Twitchen, «Transient current electric field profiling of single crystal CVD diamond» *Semicond. Sci. Technol.,* vol. 21, p. 1193–1195, 2006.

[99] J. Fink, P. Lodomez, H. Kruger, H. Pernegger, P. Weilhammer and N. Wermes, «TCT characterization of different semiconductor materials for particle detection» *Nuclear Instruments and Methods in Physics Research Section A,* vol. 565, n. 1, p. 227–233, 2006.

[100] S. Uxa, E. Belas, R. Grill, P. Praus and R. B. James, «Determination of Electric-Field Profile in CdTe and CdZnTe Detectors Using Transient-Current Technique» *IEEE Transactions on Nuclear Science,* vol. 59, n. 5, pp. 2402 - 2408, 2012 .

[101] M. Zanichelli, A. Santi, M. Pavesi and A. Zappettini, «Charge collection in semi-insulator radiation detectors in the presence of a linear decreasing electric field» *J. Phys. D: Appl. Phys.,* vol. 46 , p. 365103, 2013.

[102] A. Cola, I. Farella, A. M. Mancini and A. Donati, «Electric Field Properties of CdTe Nuclear Detectors» *IEEE Transactions on Nuclear Science,* vol. 54, n. 4, pp. 868-872, 2007.

[103] P. J. Sellin, G. Prekas, J. Franc and R. Grill, «Electric field distributions in CdZnTe due to reduced temperature and x ray irradiation» *Appl. Phys. Lett.,* vol. 96, p. 133509, 2010.

[104] A. Santi, M. Zanichelli, G. Piacentini, M. Pavesi, A. Cola and I. Farella, «An original method to evaluate the transport parameters and reconstruct the electric field in solid-state photodetectors» *Applied Physics Letters,* vol. 104, p. 193503, 2014.

[105] K. Suzuki, S. Seto , T. Sawada and K. Imai, «Carrier transport properties of HPB CdZnTe and THM CdTe:Cl» *2001 IEEE Nuclear Science Symposium Conference Record,* vol. 4, pp. 2391 - 2395, 2001.

[106] P. J. Sellin, A. W. Davies, A. Lohstroh, M. E. Ozsan and J. Parkin, «Drift Mobility and Mobility-Lifetime Products in CdTe:Cl Grown by the Travelling Heater Method» *IEEE Transactions on Nuclear Science,* vol. 52, n. 6, pp. 3074-3078, 2005.

[107] A. Cola, I. Farella, M. Anni and M. C. Martucci, «Charge Transients by Variable Wavelength Optical Pulses in CdTe Nuclear Detectors» *IEEE Transactions on Nuclear Science,* vol. 59, n. 4, pp. 1569-1574, 2012.

[108] C. Ghezzi, Fisica dei Semiconduttori, Monte Università di Parma, 2013.

[109] P. Y. Yu and M. Cardona, Fundamentals of Semiconductors, Springer, 2005.

[110] M. S. Dresselhaus, SOLID STATE PHYSICS PART II - Optical Properties of Solids, 2001.

[111] R. H. Bube, Photoconductivity of Solids, John Wiley & sons, 1960.

[112] D. A. Melnick, «Zinc Oxide Photoconduction, an Oxygen Adsorption Process» *The Journal of Chemical Physics,* vol. 26, p. 1136, 1957.

[113] Q. H. Li, T. Gao, Y. G. Wang and T. H. Wang, «Adsorption and desorption of oxygen probed from ZnO nanowire films by photocurrent measurements» *Applied Physics Letters,* vol. 86, p. 123117, 2005.

[114] J. D. Prades, F. Hernandez-Ramirez, R. Jimenez-Diaz, M. Manzanares, T. Andreu, A. Cirera, A. Romano-Rodriguez and J. R. Morante, «Effects of electron-hole separation on the photoconductivity of individual metal oxide nanowires» *Nanotechnology,* vol. 19, p. 465501:1–465501:7, 2008.

[115] J. Goldstein, D. E. Newbury, D. C. Joy, C. E. Lyman, P. Echlin and E. Llfshin, Scanning Electron Microscopy and X-ray Microanalysis, 3rd Ed., Springer, 2003.

[116] F. J. García de Abajo, «Optical excitations in electron microscopy» *REVIEWS OF MODERN PHYSICS,* vol. 82, n. 1, pp. 209-275, 2010.

Acknowledgements

Special Thanks to my tutor Maura Pavesi for all the support that she gave me in these three years, and to all members of our opto-electronics group at the University of Parma: Andrea Santi and Massimiliano Zanichelli.

Thanks to Andrea Zappettini, Marco Villani and Davide Calestani and the entire Signal group at IMEM-CNR for the ZnO nano-tetrapod samples.

To Roberto Fornari and Francesco Boschi for providing the Ga_2O_3 samples and relative informations, and thaks to all the people in their their research group at IMEM-CNR and at the Physics department at the university of Parma.

Thanks to Antonella Parisini, Andrea Baraldi, and Marco Gorni for help and support for the completion of this work.

Finally, thanks to all the researchers that contributed to the measurements that are presented in this PhD thesis: F. Fabbri, G. Salviati, E. Gombia, E. Buffagni, C. Ferrari.